Technical Physics Letters, Vol. 26, No. 1, 2000, pp. 1–3. Translated from Pis'ma v Zhurnal Tekhnicheskoĭ Fiziki, Vol. 26, No. 1, 2000, pp. 3–8.

The Use of a Scanning Tunneling Microscope (STM) for Investigation of Local Photoconductivity of Quantum-Dimensional Semiconductor Structures

V. Ya. Aleshkin, A. V. Biryukov, S. V. Gaponov, Z. F. Krasil'nik, and V. L. Mironov

Institute of Physics of Microstructures, Russian Academy of Sciences, Nizhni Novgorod, Russia

Received January 27, 1999

Abstract—The possibility is demonstrated of using the STM for recording spectra of photoconductivity of quantum-dimensional semiconductor structures with a high spatial resolution. Studies are made into the local photoconductivity of GaAs/$In_xGa_{1-x}As$ based quantum wells and quantum points as a function of the depth of location of the quantum-dimensional structure relative to the surface space charge region. For quantum points in the vicinity of the sample surface, spectra are obtained which are characterized by features associated with the individual energy spectrum of those points. *© 2000 MAIK "Nauka/Interperiodica".*

The standard methods of investigation of the photoconductivity and photoluminescence of semiconductor structures with quantum wells and quantum points enable one to derive information averaged over the observation region which exceeds considerably the characteristic lateral scale in the structure such as the size of quantum points, the scale of irregularities of alloying of quantum wells, etc. [1–3]. The use of probing microscopy makes for considerably higher spatial resolution owing to a reduction of the beam aperture of exciting or received radiation. The main progress made in this field is associated with the use of a near-field optical microscope to investigate the photoconductivity [4, 5] and photoluminescence [6–8] of quantum-dimensional structures. In our opinion, however, it appears especially promising to study the local photoconductivity of such structures by photoresponse in the tunneling current of a scanning tunneling microscope, because the use of a tunneling contact as photocurrent sensor enables one to localize the probing region within a single quantum point.

This paper deals with the results of investigations of the local photoconductivity of GaAs/$In_xGa_{1-x}As$ quantum wells and quantum points using an STM in combination with an optical system [9]. The experiment was staged for the purpose of observing the dependence of the current of tunneling contact between the STM probe and a semiconductor structure on the exciting radiation wavelength. Optical pumping was provided by the radiation of a halogen lamp passed through an MDR-23 monochromator and a KS-19 passive filter serving to cut off the visible spectral region. A multifiber light guide was used to deliver the monochromatic radiation to the semiconductor structure on the side of the substrate that served as a filter to cut off light quanta with an energy greater than the width of the forbidden band of GaAs. Owing to this, the photocarriers were generated only in $In_xGa_{1-x}As$. Epitaxial GaAs/$In_xGa_{1-x}As$ structures characterized by the *n*-type conductivity and having a current-voltage characteristic of tunneling contact typical of the Schottky barrier were investigated [3]. The probe was held above the surface with the aid of the STM feedback system in the j_t = const mode at a voltage corresponding to the forward branch of the current-voltage characteristic. The photocurrent was measured as a difference between the current in the reverse branch of the current-voltage characteristic upon illumination of contact and the dark current.

The spatial resolution of the suggested procedure depends substantially on the depth of location of the quantum-dimensional structure relative to the surface space charge region (SCR). If a quantum well or a layer of quantum points are outside of the SCR, the lateral size of the region from which the photocarriers are collected to the STM probe is of the order of the diffusion length of carriers in GaAs (~1 μm). If a quantum well is in the SCR, the spatial resolution is subjected to a determining effect of the factors such as diffusion of carriers along the well until the moment of departure due to thermal activation or tunneling, the transit of photocarriers in a strong surface field (it amounts to approximately 10^5 V/cm), and the process of their capture on deep-lying surface states. For quantum points in the vicinity of the surface, the role of diffusion processes becomes unimportant, and the spatial resolution may, in principle, be brought up to the size of the wave function of minority carriers on a single quantum point.

Experiments revealed a fairly strong dependence of the value of photocurrent of STM on the intensity and wavelength of exciting light. Figure 1 gives the spectra of photoexcitation of an $In_xGa_{1-x}As$/GaAs heterostructure with a quantum well located at a depth of ~250 nm and of a heterostructure containing a layer of quantum

1063-7850/00/2601-0001$20.00

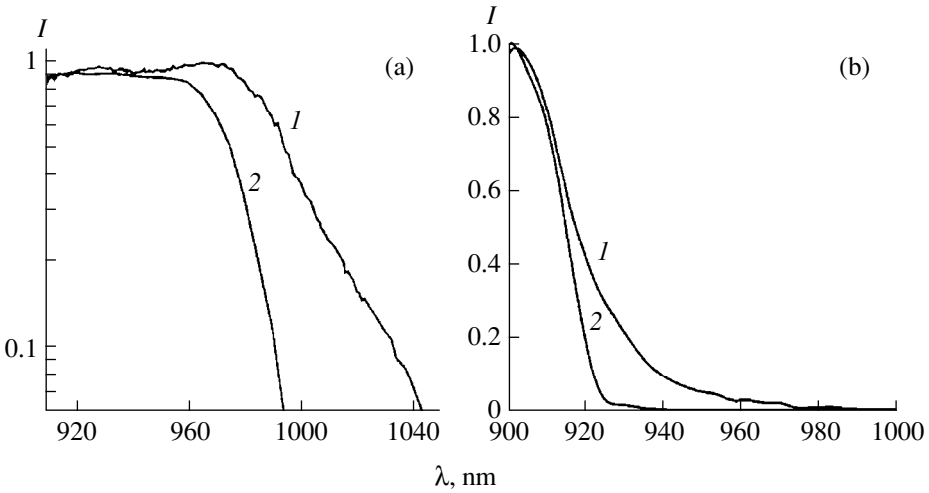

Fig. 1. The spectra of photoconductivity of structures containing (a) GaAs/$In_xGa_{1-x}As$ quantum well and (b) a layer of GaAs/InAs quantum points. The thickness of the coating layer of GaAs is 250 and 320 nm, respectively. Curves *1* were obtained using the standard procedure of measuring the photocurrent on macrocontacts. Curves *2* were obtained by registering local photoresponse in the STM.

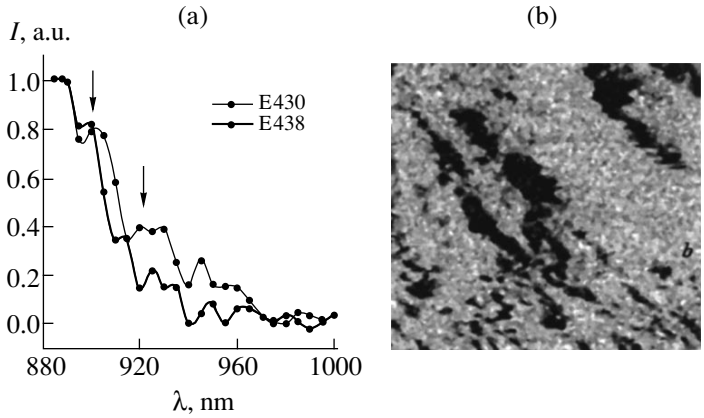

Fig. 2. (a) STM spectra of the photoconductivity of structures with InAs/GaAs quantum points in the surface region. The coating layer thickness for E438 sample is 2 nm, and that for E430 sample is 1.5 nm. (b) The distribution of photoresponse over the surface of a sample containing a quantum well at a depth of 250 nm. The frame size, 1×1 μm.

points of InAs in GaAs at a depth of ~320 nm. The STM spectra were compared with the spectra obtained using the standard procedure of measuring the photocurrent on macrocontacts ~500 μm in diameter deposited onto the sample [3]. As demonstrated by the experimental results, the photoconductivity spectra obtained in STM have a sharper long-wave edge responsible for absorption on dimensional quantization levels. This may be attributed to the fact that the region from which the photocarriers are collected on the STM probe is much less than the size of macrocontacts and, therefore, the degree of smearing of spectrum due to fluctuations in the thickness and composition of the $In_xGa_{1-x}As$ level is lower.

Figure 2a gives the photoconductivity spectra of layers of quantum points grown in the vicinity of the sample surface. In order to preclude oxidation, such structures were immersed in vacuum oil immediately after growth, so that the spectra were taken from the tunneling contact realized via an oil interlayer. In this case, the diffusion processes were unimportant, and a thin structure of the long-wave edge of photoexcitation was observed (shown by arrows in the figure), which is associated with the dimensional quantization levels at quantum points and in the thin wetting layer of InAs.

Along with the spectral measurements, investigations were performed on the nonuniformity of distribution of photoresponse over the sample surface. For this purpose, the feedback loop was broken when scanning a sample at every point of the frame, and the value of current in the reverse branch of semiconductor characteristic was recorded. Figure 2b shows a typical distribution of photoresponse over the surface of a structure with a quantum well located at a depth of 250 nm. The

dark regions in the figure correspond to the regions of the structure where no photoresponse is observed. The image contrast may be determined both by the nonuniformity of the quantum well and by the local electrical properties of the coating layer; therefore, additional investigations of the morphology and properties of the coating layers are required.

We have demonstrated the possibility of using STM for registering the local photoconductivity of quantum-dimensional structures with a high spatial resolution. For structures with quantum points on the sample surface, the probing region may be localized within a single quantum point, which enables one to study its individual energy spectrum.

ACKNOWLEDGMENTS

We are grateful to D.G. Revin for assistance in our work, to A.V. Murel' for the data on measurements of photoconductivity on macrocontacts he placed at our disposal, and to O.I. Khrykin and V.M. Danil'tsev for their samples.

This study received support from the Fundamental Metrology Program of the State Committee for Science and Technology (project 3.45) and from the Russian Foundation for Basic Research (project nos. 96-02-16990a and 98-02-16625).

REFERENCES

1. A. W. Leitch and H. L. Ehlers, Infrared Phys. **28** (6), 433 (1988).
2. J.-Y. Marzin, J.-M. Gerard, A. Izraël, *et al.*, Phys. Rev. Lett. **73** (5), 716 (1994).
3. V. Ya. Aleshkin, D. M. Gaponova, S. A. Gusev, *et al.*, Fiz. Tekh. Poluprovodn. **32** (1), 111 (1998) [Semicond. **32** (1), 99 (1998)].
4. S. K. Buratto, J. W. P. Hsu, E. Betzig, *et al.*, Appl. Phys. Lett. **65** (21), 2654 (1994).
5. M. S. Ünlü, B. B. Goldberg, and W. D. Herzog, Appl. Phys. Lett. **67** (13), 1862 (1995).
6. R. D. Grober, T. D. Harris, J. K. Trautman, *et al.*, Appl. Phys. Lett. **64** (11), 1421 (1994).
7. T. D. Harris, D. Gershoni, L. Pfeiffer, *et al.*, Semicond. Sci. Technol. **11**, 1569 (1996).
8. A. Chavez-Pirson, J. Temmyo, H. Kamada, *et al.*, Appl. Phys. Lett. **72** (26), 3494 (1998).
9. D. G. Volgunov, S. V. Gaponov, V. F. Dryakhlushin, *et al.*, Prib. Tekh. Éksp., No. 2, 132 (1998).

Translated by H. Bronsteĭn

Technical Physics Letters, Vol. 26, No. 1, 2000, pp. 10–11. Translated from Pis'ma v Zhurnal Tekhnicheskoĭ Fiziki, Vol. 26, No. 1, 2000, pp. 21–23.

The Resonance and Nonresonance Coefficients of Stimulated Transitions for a System with Relaxation

M. G. Noppe

Novosibirsk State Technical University, Novosibirsk, Russia

Received May 17, 1999

Abstract—Temperature-dependent resonance and nonresonance stimulated transition coefficients are determined for a system with relaxation. The resonance coefficient was used for simulation of the output parameters of lasers. The nonresonance coefficients were used for interpretation of the observed multimode emission spectrum of long lasers. © *2000 MAIK "Nauka/Interperiodica".*

1. INTRODUCTION

The coefficients of stimulated transitions are necessary for calculation of the amplification and the output radiation intensity of semiconductor injection lasers. Casey and Panish [1] calculated these quantities using a golden rule introduced for the idealized model of a system without relaxation. An expression for the stimulated transition coefficient derived in [1] had some limitations with respect to time (see formula (3.5.18) in [2]). In this paper, we will determine the resonance (used for simulation of the output laser parameters [3, 4]) and nonresonance temperature-dependent constant coefficients of stimulated transitions for a system with relaxation. The constant nonresonance coefficients of stimulated transitions are used for interpretation of the multimode emission spectra of long lasers.

2. THEORY

Consider a system in a multifrequency field, for which the Hamiltonian of interaction with the field has the following form:

$$H(t) = \sum_m H^{(m)} \cos(\omega_m t + \varphi_m).$$

In this work, we consider a semiconductor laser as a multilevel system in a multifrequency field. An equation for the density matrix of a certain pair of levels 2 and 1 in the multilevel system with vertical transitions can be presented in the following way [2, 6]:

$$d\rho_{21}/dt + (i\omega_0 + \Gamma)\rho_{21} = (1/i\hbar)H_{21}(\rho_{11} - \rho_{22}), \quad (1)$$

where $\hbar\omega_0 = E_2 - E_1$, H_{21} is a matrix element of the Hamiltonian of interaction with the field; $\Gamma = 1/T_2$; and T_2 is the electron scattering time. The latter quantity is estimated according to the formula $T_2 = 1.27 \times 10^{-11}/T$ (sK) (where T is the temperature), obtained in [7] on the basis of experimental data. Assuming that $(\rho_{22} - \rho_{11})$ = const and using the rotating wave approximation, we find a solution of equation (2) for the stationary regime. The rate of the overall stimulated transition $2 \longrightarrow 1$ is given by the formula:

$$r_{21}^s = (i/\hbar)(H(t)_{21}\rho(t)_{12} - \rho(t)_{21}H(t)_{12}). \quad (2)$$

Using formula (2), we may write the time-independent component of the overall stimulated transition rate $r_{21}^{s,0}$ as follows:

$$r_{21}^{s,0} = \left(B_{21}P_0 + \sum_{m\neq 0} C_{21}^{(m)}P_m\right)(\rho_{22} - \rho_{11}), \quad (3)$$

where P_m is the energy density at the frequency ω_m, and

$$B_{21} = (\bar{H}_{21}/\hbar)^2(1/2\Gamma), \quad (4)$$

$$C_{21}^{(m)} = (\bar{H}_{21}/\hbar)^2[\Gamma/((\omega_0 - \omega_m)^2 + \Gamma^2)]/2, \quad m \neq 0, \quad (5)$$

$$\bar{H}_{21} = H_{21}^{(0)}/\sqrt{P_0}. \quad (6)$$

3. CALCULATION

The overall stimulated transition rate is proportional to the sum of the resonance term $B_{21}P_0$ and the nonresonance terms $C_{21}^{(m)}P_m$ (see equation (3)). The coefficient at P_0 is denoted as B_{21} because this value virtually coincides with the Einstein coefficient for a stimulated transition [8]. The terms $C_{21}^{(m)}P_m$ determine the interaction of laser modes related to a nonresonance mechanism of stimulated transitions: a mode with the frequency ω_m leads to stimulated transitions at the frequency ω_0. This nonresonance mechanism of stimulated transitions generalizes the concept of the stimulated transition. In particular, the Einstein relationship for the stimulated transition coefficients B_{21} and B_{12} follows from formula (4): $B_{21} = B_{12}$. In the same

way, it follows from formula (5) that $C_{21}^{(m)} = C_{12}^{(m)}$. Let us estimate the parameters of a laser for which a nonresonance mechanism of stimulated transitions would appear to be significant. Assuming that $C_{21}^{(l)}/B_{21} > \varepsilon$, where ε is the criterion of an essentially nonresonance mechanism and ω_1 is the frequency of the mode that is most close to the mode with the frequency ω_0, we obtain the following inequality: $L > \pi c T_2^p \overline{\varepsilon/(1-\varepsilon)}/n$, where n is the index of refraction, L is the length of the laser, and T_2 is the time construct estimated according to the formula $T_2 = 1.27 \times 10^{-11}/T$ (sK) [7]. For $T = 300$ K, $\varepsilon = 0.25$, and $n = 3.4$, this yields $L > 68$ μm. It follows from this estimate that the nonresonance mechanism of stimulated transitions is quite important for maintaining a multimode spectrum of radiation in sufficiently long lasers. Eliseev and Sverdlov [5, pp. 88–90] analyzed experimental works and concluded that "lasers with short cavities are preferable for obtaining a single-mode regime." Therefore, the nonresonance mechanism of stimulated transitions helps to account for the observed multimode spectrum of radiation of rather long lasers.

ACKNOWLEDGMENTS

The author is grateful to Ya. S. Grinberg for fruitful discussion.

REFERENCES

1. H. Casey and M. Panish, *Heterostructure Lasers* (Academic Press, New York, 1978; Mir, Moscow, 1981), Part A.
2. A. Yariv, *Quantum Electronics* (Wiley, New York, 1989; Sov. Radio, Moscow, 1980).
3. M. G. Noppe, Pis'ma Zh. Tekh. Fiz. **25** (3), 33 (1999) [Tech. Phys. Lett. **25** (2), 97 (1999)].
4. M. G. Noppe, *Proceedings of the IV International Scientific–Technical Conference APIE-98, Novosibirsk, Russia* (1998), Vol. 1, p. 93.
5. P. G. Eliseev and B. N. Sverdlov, *Achievements in Science and Technology, Ser. Electronics* (VINITI, Moscow, 1988), Vol. 21.
6. M. G. Noppe, *Physical Principles of Nonlinear Theory of Injection Semiconductor Lasers* [in Russian] (Novosibirsk, 1995).
7. Zh. I. Alferov, A. T. Gorelenok, V. V. Mamutin, *et al.*, Fiz. Tekh. Poluprovodn., No. 11, 1999 (1984) [Sov. Phys. Semicond. **18** (11), 1247 (1984)].
8. A. Eĭnsteĭn, Zur Quanten Theorie der Strahlung, Mitt. Phyz. Ges. (Zurich), No. 18, 47 (1916); *A Collection of Scientific Works* (Nauka, Moscow, 1966), Vol. 3, pp. 386–392.

Translated by A. Chikishev

Technical Physics Letters, Vol. 26, No. 1, 2000, pp. 12–14. Translated from Pis'ma v Zhurnal Tekhnicheskoĭ Fiziki, Vol. 26, No. 1, 2000, pp. 24–29.

Formation of a Two-Sided Porous Structure during Electrochemical Silicon Etching by the Unno–Imai Method

S. P. Zimin, M. N. Preobrazhenskiĭ, and D. S. Zimin

Demidov Yaroslavl' State University, Yaroslavl, Russia

Institute of Microelectronics, Russian Academy of Sciences, Yaroslavl, Russia

Received July 14, 1999

Abstract—It is shown that the formation of porous silicon on the anode side of a silicon wafer by the liquid-contact method is accompanied by the appearance of a modified layer on the cathode side of the wafer. The thin modified layer has a porous structure and can attain the thickness of up to several microns. Unlike the main porous silicon layer, the modified porous layer on the cathode side is characterized by high electric conductivity. It is established that this layer also contains platinum and rhodium distributed over the whole layer thickness. Possible practical applications of the modified layer are considered. *© 2000 MAIK "Nauka/Interperiodica".*

Porous silicon is a promising material for opto-, micro-, and nanoelectronics. The unique properties of porous layers allow one to use them in the design of various devices such as emitters, photodetectors, membranes, chemical and biological sensors, photon crystals, etc. [1]. Each of such devices has a porous layer with certain structural parameters. Therefore, the development of technological processes for obtaining porous silicon layers with the necessary properties is a rather important problem. Usually, porous silicon layers are obtained upon the anode electrochemical treatment of silicon in various hydrofluoric acid-based electrolytes, in particular, by using the Unno–Imai liquid-contact method [2] in which a silicon wafer is placed between two platinum electrodes. The schematic of the method is shown in Fig. 1. A twin fluoroplastic cell with two platinum electrodes is used. The voltage supplied to the electrodes gives rise to the formation of a porous layer on the anode side of the wafer, whose properties depend on the electrolyte composition, anodization mode, the dopant type, etc. However, the processes occurring on the back side of the wafer are almost unstudied. Foll [3] described the anode and the cathode sides of the wafer and found that silicon on the cathode side is inert and, therefore, shows no interesting phenomena. However, our experiments showed that this statement is not always correct and that, under certain conditions, the cathode mode results in essential changes in the subsurface silicon layer.

In our experiments, the initial substrates were (111)-oriented silicon wafers heavily doped with boron or antimony (0.03 and 0.01 Ω cm, respectively). The electrodes were made of the Pt–Rh alloy, the anodizing-current density (j) in the HF-based electrolytes varied within 5–50 mA/cm^2, the time t of the specimen treatment varied within 5–60 min. During the experiment, a conventional 10–150 μm-thick porous silicon layer was formed on the working (anode) side of the wafer; whereas, on the cathode side, only a thin modified silicon layer was formed. At high current densities and large times of the specimen treatment, this modified layer attained the thickness ranging from 1 to 7 μm and was well observed on the wafer cleavage in an optical microscope (Fig. 2).

The crystal structure of the modified layer was studied on a DRON-2 X-ray diffractometer (Co-radiation). The X-ray diffractograms had only silicon reflections corresponding to the (111)-orientation and showed no reflections of any other phases. This indicates that the modified layer preserves the single-crystal silicon matrix. The chemical composition of the modified layer on the cathode side of the wafer was studied on a PHI-660 Auger spectrometer and a CAMECA IMS4F mass-spectrometer. The measured profiles showed that

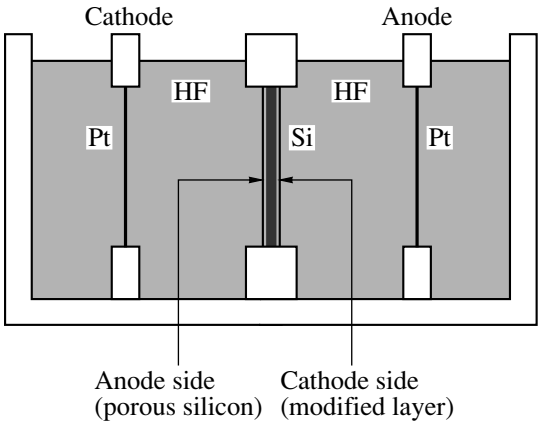

Fig. 1. Electrolytic cell used in the Unno–Imai method.

the silicon distribution is uniform over the whole thickness of the modified layer and undergoes no changes in the wafer bulk. The modified layer is enriched with oxygen and carbon, which are also uniformly distributed over the whole layer thickness. The characteristic feature of the modified layer is the presence of considerable amounts of platinum and rhodium, attaining on the surface the total amount of 3 at. %. This value slightly decreases along the direction toward the substrate. It should be emphasized that the porous silicon layer formed on the anode side of the wafer contained no noble metals in its bulk, but showed negligible amounts of noble metals on the surface. Our experiments led to the assumption that the modified layer had a porous structure as well. This assumption is favored by the following facts: first, the layer preserves the single-crystal structure typical of low-density porous silicon. Second, the amounts of oxygen and carbon in the modified layer and the profiles of their distributions were almost the same as in the porous silicon layer formed on the anode side of the wafer. Third, the penetration of Pt and Rh ions into a depth of several microns into silicon during its electrochemical treatment can be explained only by the presence of a well-developed system of micropores.

To confirm our hypothesis on the porous structure of the modified layer, we measured the $V(z)$ curves on an ELSAM acoustic microscope. It is well known that the velocity of the Rayleigh surface wave determined from the $V(z)$ curves is strongly dependent on the material porosity [4]. Figure 3 shows the $V(z)$ curves obtained for the initial silicon wafer, porous silicon layer on the anode side, and the modified layer measured on the same structure at a radiation frequency of 1 GHz. The coordinate z was measured from the surface and corresponded to the displacement of the acoustic lens along the direction toward the specimen. The velocity of a surface wave in silicon calculated from these curves by formula from [5] equals 4750 m/s and is in good accord with the known data. The velocity of a surface wave in the porous layer on the anode side of the wafer equals 3180 m/s, which, in accordance with [4], corresponds to the silicon porosity equal to 35% and is consistent with the results of the independent determination of porosity by the gravimetric method. The velocity of a surface wave in the modified layer equals 3880 m/s, which indicates that this layer has a porous structure with the porosity equal to 20%. Thus, the modified layer formed on the cathode side of the silicon wafer can be nothing else but a thin layer of porous silicon with new structural characteristics.

The formation of a modified porous layer on the cathode side of the silicon wafer can be interpreted in the following way. Using electrolytic cells for silicon wafers with aluminum contacts on the nonworking sides, Lehmann showed [6] that pores can be formed not only in the anode mode, but also in the case of small bias voltages in the cathode mode. The voltage supplied to the electrodes in the Unno–Imai liquid-contact

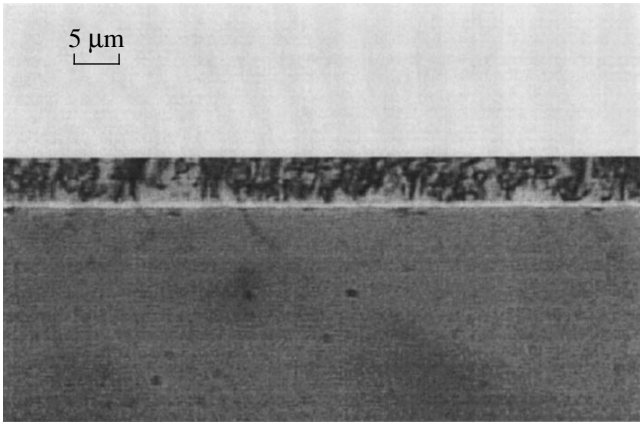

Fig. 2. Typical micrograph of the modified layer formed on the cathode side of the silicon wafer.

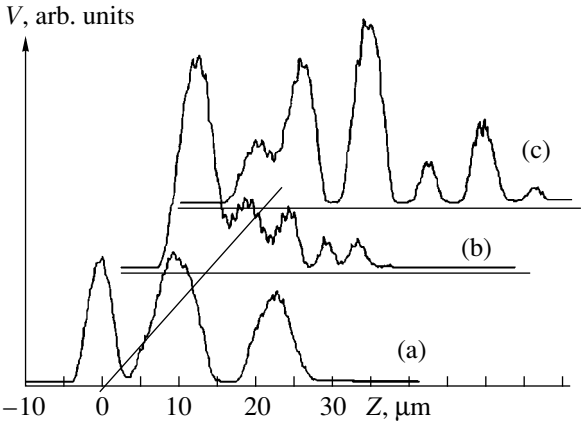

Fig. 3. $V(z)$ curves for (a) the initial silicon, (b) the porous silicon layer on the anode side of the wafer, and (c) the modified layer formed on its cathode side. Antimony-doped silicon, $j = 50$ mA/cm^2, $t = 60$ min.

method is redistributed among all the elements of the electrolytic cell. The attainment of the modes, such as were described in [6], on the cathode side of the wafer can provide the conditions favoring pore formation. It should be remembered that formation of a porous layer on the cathode side of the wafer is rather intense only for heavily-doped wafers and is almost absent for high-resistance silicon.

Thus, the results obtained in this study prove that the Unno–Imai method can be used for obtaining a two-sided porous structure using heavily-doped silicon wafers. Along with the formation of porous silicon on the anode side of the wafer, a thin porous layer is also formed on its cathode side. The main feature of the porous layer on the cathode side is the presence of noble metal in the layer bulk. As a result, if the resistivity of the main porous silicon layer is high enough, the resistivity of the modified layer on the cathode side is almost equal to the resistivity of the initial silicon

wafers. This fact allows one to fabricate ohmic contacts with low transient resistivities for both porous layers and the structure as a whole. The transient resistivities of aluminum contacts for the modified layer were lower, by almost an order of magnitude, than the resistivity of the aluminum–silicon contact. Moreover, the study of aluminum metallization [7] also showed that the conditions for growth of metal films on the surface of the modified layer are essentially different from the conventional conditions.

ACKNOWLEDGMENTS

This study was supported by the Ministry of Education of the Russian Federation, project no. 98-8-4.3-231, and the International Science Organization, projects d99-633 and s99-496.

We are grateful to E.Yu. Buchin for useful discussions and also to V.K. Smirnov and V.V. Naumov, who performed the elemental analysis and the diffractometric measurements, respectively.

REFERENCES

1. *Materials of the International Conference "Porous Semiconductors—Science and Technology"* (Mallorca, Spain, 1998).
2. K. Imai and H. Unno, IEEE Trans. Electron. Dev. **ED-31**, 297 (1984).
3. H. Foll, Appl. Phys. A **53**, 8 (1991).
4. R. J. M. Da Fonseca, J. M. Saurel, A. Foucaran, *et al.*, Thin Solid Films **225**, 155 (1995).
5. R. D. Weiglein, IEEE Trans. **SU-32** (2), 225 (1985).
6. V. Lehmann, J. Electrochem. Soc. **140**, 2836 (1993).
7. S. P. Zimin, M. N. Preobrazhenskiĭ, and D. S. Zimin, in *Proceedings of V International Conference on High Technologies in Russian Industry* (Moscow, Russia, 1999), p. 225.

Translated by L. Man

Technical Physics Letters, Vol. 26, No. 1, 2000, pp. 15–18. Translated from Pis'ma v Zhurnal Tekhnicheskoĭ Fiziki, Vol. 26, No. 1, 2000, pp. 30–37.

Identification of Self-Organized Vortexlike Structures in Numerically Simulated Turbulent Flow of a Viscous Incompressible Liquid Streaming around a Well on a Plane

S. A. Isaev, A. I. Leont'ev, and P. A. Baranov

Academy of Civil Aviation, St. Petersburg, Russia

Received September 3, 1999

Abstract—A system of Reynolds equations closed by adding a low-Reynolds-number Menter's dissipative model of turbulence are solved with the use of a factorized finite-volume method. The generation of vortexlike structures in the case of stalled turbulent flow streaming around a deep well on a plane is analyzed. The effect of vortex intensification due to asymmetry of the well is discussed. © *2000 MAIK "Nauka/Interperiodica".*

In recent years, the phenomenon of vortex intensification of heat and mass exchange processes, determined by the generation of self-organized vortex structures in a low-velocity flow streaming around curvilinear reliefs, in particular, spherical wells, has been extensively studied. There is certain progress in these studies, which is related to the development and application of the numerical simulation methods. Recently, we have [1] proposed a simplified approach to the numerical simulation of the stationary spatial vortex structures formed within a spherical well streamlined by a laminar flow of viscous incompressible liquid. This approach is characterized by the use of cylindrical grids with high mesh density inside the well and by analytical representation of the metric coefficients, which allows one to avoid their interpolation and increase the accuracy of the solution. Within the framework of this approach, developed in [1–5], flow–vortex structures responsible for the mass transfer in a stalled flow were identified including the closed vortex rings. Lin *et al.* [6] made an attempt at calculating the turbulent flow in a channel with rows of spherical wells on one of the walls with the use of the CFL3D computer codes.

In this numerical study, we have concentrated on a detailed analysis of the mechanism of controlled vortex generation in a turbulent boundary flow of an incompressible viscous liquid in the vicinity of an isolated concave well on a smooth wall with an allowance of the well shape asymmetry. Like in [1], we have used computer visualization of the flow by monitoring the tracks of labeled liquid particles for identification of the spatial flow–vortex structures. We consider a spherical well with a rounded edge (the well depth is 0.22 and the edge radius is 0.1) for which the regime of steady turbulent streamlining with the formation of a developed zone of stalled flow is realized.

For numerical simulation of the turbulent flow in the vicinity of the curvilinear relief, we have used an approach different from that employed in [1–5]. This method, previously used for the solution of 2D problems involving flows streamlining the bodies with vortex cells (see, e.g., [7]), is based on the application of multiblock grids. The constructed factorized algorithm is based on an implicit finite-volume method of solution of the Navier–Stokes equations averaged according to Reynolds. The set of equations is closed by adding a two-parameter low-Reynolds-number Menter's dissipative model of turbulence [8] within the framework of the concept of decomposition of the calculation area and the generation of oblique grids of the H and O types with overlap in the selected subareas of substantially different scales. The system of initial equations is presented in the divergence form for increments of the dependent variables, in particular, the Cartesian velocity components. For approximation of the source terms, the convection flows are calculated with the aid of a 1D counterflow UMIST scheme that is a variant of the TVD scheme [9]. In general, the methodology of this study is the same as that described in [10].

In order to solve the problem of turbulent flow streaming around a deep well and to provide for a better resolution of different-scaled structural elements of the flow, such as the shear layer and the reverse flow zone, it is expedient to consider separately a boundary area of a cylindrical ring shape circumscribed around the well. The external radius of the cylinder is 1 (all linear dimensions are related to the diameter of the well), the inner radius is 0.1, and the height is 0.175. An oblique curvilinear grid matched to the streamlined surface is imposed on the area considered (Fig. 1). Sixty cells are uniformly distributed over the circumference, from 30 to 45 cells are selected in the vertical direction in such

1063-7850/00/2601-0015$20.00

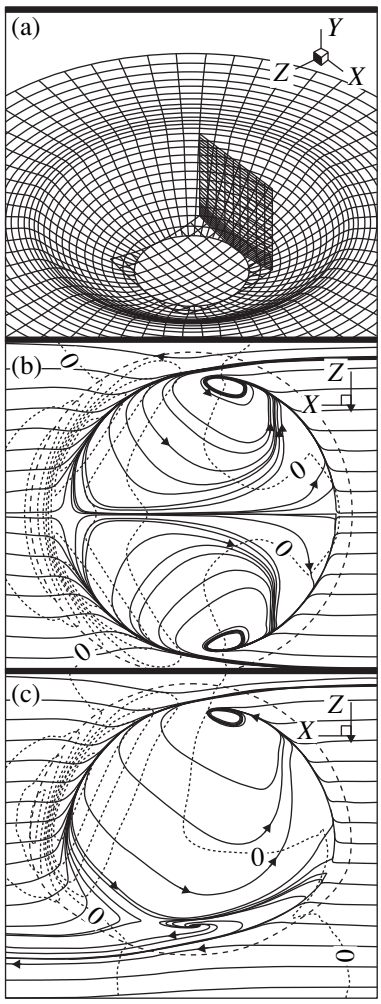

Fig. 1. Schematic diagrams showing (a) a fragment of the multiblock spatial grid in the vicinity of a spherical well with the depth 0.22, and the streamline patterns of liquid flowing over the surface of (b) spherical and (c) asymmetric wells. Dashed lines correspond to isobars plotted with a step of 0.02. Zero level of the excessive pressure is marked with the symbol 0.

a way that the grid nodes concentrate near the wall (a minimum step near the wall was varied from 0.0008 to 0.005). In the radial direction, the cells (from 30 to 45) concentrate near the boundary of the well (the minimum step is 0.015).

A large-scale rectangular area, with the base partly coinciding with the streamlined flat wall covers the area of the well under consideration. The origin of the Cartesian coordinates coincides with the projection of the center of the well onto the plane. The length of the area is 17, its height is 5, and the width is 10. The area is divided by a Cartesian grid ($55 \times 35 \times 40$ cells). The nodes of the grid concentrate in the vicinity of the well (the minimum step in the longitudinal and transverse directions is 0.15) and near the wall (the step near the boundary varies from 0.001 to 0.005).

For better resolution of the boundary flow in the vicinity of the axis of the cylindrical subarea, we introduce a patch that intersects this area (Fig. 1a) and has a shape of the curvilinear parallelepiped. Within the boundaries of this patch, we construct a grid with uniform distribution of the nodes in the longitudinal and transverse directions. The steps of this grid are matched to the boundary step of the grid in the neighboring cylindrical area. Also matched are the positions of the grid nodes in the vertical direction.

We have analyzed the streamline patterns around the wells of two types—of the spherical shape and of an asymmetric geometry comprising a combination of the spherical and elliptical (with the semiaxes ratio 0.3 to 0.5) shapes (Figs. 1b, 1c).

A profile of the flow velocity set at the input boundary corresponds to the 1/7 profile for a turbulent boundary layer with the thickness close to the depth of the well (0.175). Soft boundary conditions are set at the output boundaries (the conditions of continuability of the solution). At the wall, the condition of sticking is assumed to be valid. To introduce dimensionless quantities, we use the normalizing parameters representing the velocity of the oncoming flow outside the boundary layer and the diameter of the well. The Reynolds number is taken equal to 2.35×10^4.

Figures 1 and 2 we present some of the numerical results obtained using the TECPLOT system of computer visualization of the spatial fields.

Figure 1b shows a pattern of the boundary turbulent flow spreading on the surface of a deep symmetrical well. Here, as well as in the case of a laminar flow [1], we observe singularities of the focus type in the peripheral parts of the well. However, in contrast to the laminar flow, case, a zone of the stalled flow formed in the turbulent regime appears to be open. The oncoming flow gets inside the well through these open side windows, which results in substantial intensification of the vortex motion in the liquid. Note that the maximum velocity of the reverse flow inside the well, equal to 0.24 for the adopted value of $\mathrm{Re} = 2.35 \times 10^4$, appears to be four times as large as that for $\mathrm{Re} = 2500$.

For the asymmetric well (Fig. 1c), the pattern of streamlining becomes substantially asymmetric with the flow bending toward the deformed part and the pressure maximum shifting in the opposite direction. The pattern of the flow in the spherical part of this well is nearly the same as that for the symmetric case. However, the flow structure in the elliptical part is absolutely different. A singularity on this slope of the well is a sink, rather than a source (as in the case of the symmetric flow). On the whole, the structure of the large-scale vortex flow inside the asymmetric well has a spiral shape. This pattern is clearly revealed by analysis of the trajectories of labeled particles introduced at different points of the flow.

A symmetric vortexlike structure formed in the spherical well possesses a high ejection ability and has

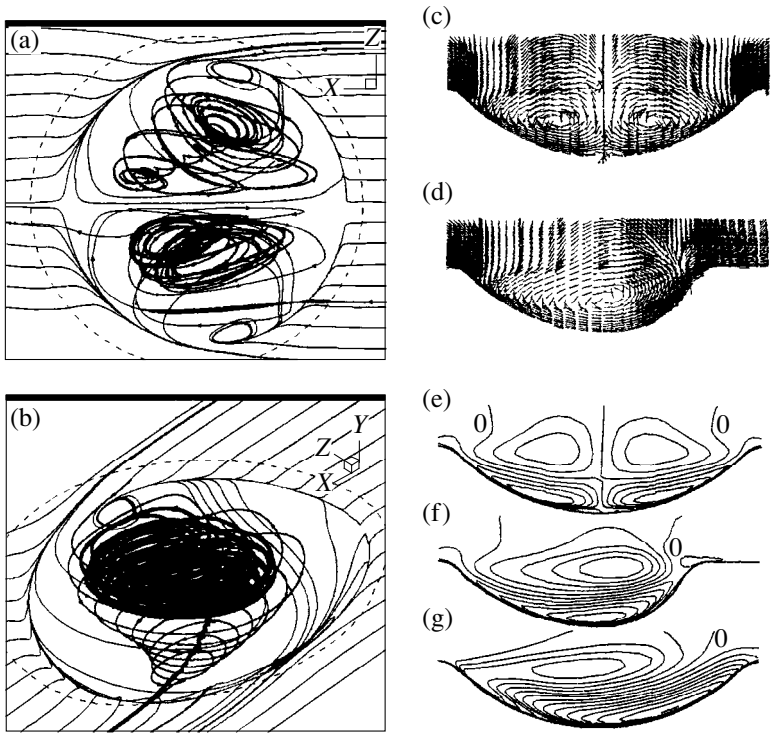

Fig. 2. Computer visualization of the flow–vortex structures realized in (a) spherical and (b) asymmetric wells. Patterns of the flow velocity vectors and isolines of the transverse flow velocity component in the median cross section ($x = 0$) of (c, e) spherical and (d, f) asymmetrical wells. Isolines of the transverse component of the velocity (g) in the longitudinal ($z = 0$) plane for asymmetrical well. Isolines are plotted with a step of 0.02 starting from zero level.

a lamellar structure. The vortex attracts particles from the oncoming flow, as depicted in Fig. 2a for a trajectory passing through a point with the coordinates $x = –0.1$, $y = –0.1$, $z = 0.2$. In particular, large-scale vortex rings, inside which the particles perform reciprocating motions (see the trajectory of a liquid particle coming through a point with the coordinates $x = –0.1$, $y = –0.1$, $z = –0.1$), are incorporated into the spiral flows outgoing from singularities at the surface of the well.

Only one flow–vortex structure is realized in the asymmetric well (Fig. 2b). A vortex ring formed by the trajectory of a labeled particle passing through the point ($x = –0.1$, $y = –0.1$, $z = 0.1$) is streamlined by a streamed flow consisting, in particular, of liquid particles of the oncoming flow (see, e.g., the trajectory of a particle passing through a point with the coordinates $x = –0.25$, $y = –0.1$, $z = 0.25$).

Integral characteristics of forces acting upon a circular element of the wall (of a unity radius) with a well

Well shape	C_x	C_y	C_z
Spherical	0.2012	–0.007475	0.00013
Asymmetric	0.1575	–0.001167	0.00091

Note: C_x, C_y, and C_z are the head, vertical, and transverse forces acting upon a circular element with a well.

A change of the secondary flow from the structure with two large scale vortex cells (realized in the spherical well) to a one-vortex structure (in the asymmetrical well) is most clearly a comparison between the velocity vector patterns in the transverse median cross section of the well (Figs. 2c, 2d). This change is quantitatively manifested by intensification of the secondary flow, that is, by a substantial increase (more than twofold) of the transverse flow velocity (Figs. 2e, 2f, and 2g) in the asymmetric vortex structure. This fact is in agreement with the phenomenon of vortex amplification upon the asymmetric flow injection into a turbulent boundary layer [11]. Note also (see table) a decrease of the head resistance of the circular part of the wall with a well and the appearance of a transverse force for the well of asymmetric geometry.

ACKNOWLEDGMENTS

This work was supported by the Russian Foundation for Basic Research, project nos. 99-01-00722 and 99-02-16745.

REFERENCES

1. S. A. Isaev, A. I. Leont'ev, D. P. Frolov, *et al.*, Pis'ma Zh. Tekh. Fiz. **24** (6), 6 (1998) [Tech. Phys. Lett. **24** (3), 209 (1998)].

2. S. A. Isaev, P. A. Baranov, A. E. Usachev, *et al.*, in *Proceedings of the 8th International Symposium on Flow Visualization, Sorrento, Italy* (1998), p. 217.1.
3. S. A. Isaev, P. A. Baranov, A. E. Usachev, *et al.*, in *Proceedings of the 4th ECCOMAS CFD Conference, Athens, Greece* (1998), Vol. 1, p. 768.
4. S. A. Isaev, A. I. Leont'ev, A. E. Usachev, *et al.*, *Proceedings of the 2nd All-Russia National Conference on Heat Exchange, Moscow, Russia* (1998), Vol. 6, p. 121.
5. S. A. Isaev, A. I. Leont'ev, A. E. Usachev, *et al.*, Izv. Ross. Akad. Nauk, Énergetika, No. 2, 126 (1999).
6. Y.-L. Lin, T. I.-P. Shih, and M. K. Chyu, ASME Paper, No. 99-GT-263 (1999).
7. P. A. Baranov, S. A. Isaev, Yu. S. Prigorodov, *et al.*, Pis'ma Zh. Tekh. Fiz. **24** (8), 33 (1998) [Tech. Phys. Lett. **24** (4), 301 (1998)].
8. F. R. Menter, AIAA J. **32** (8), 1598 (1994).
9. F. S. Lien, W. L. Chen, and M. A. Leschziner, Int. J. Numer. Meth. Fluids **23**, 567 (1996).
10. P. A. Baranov, S. A. Isaev, Yu. S. Prigorodov, *et al.*, Pis'ma Zh. Tekh. Fiz. **24** (17), 16 (1998) [Tech. Phys. Lett. **24** (9), 671 (1998)].
11. F. S. Henry and H. H. Pearcey, AIAA J. **32** (12), 2415 (1994).

Translated by A. Chikishev

Technical Physics Letters, Vol. 26, No. 1, 2000, pp. 19–20. Translated from Pis'ma v Zhurnal Tekhnicheskoĭ Fiziki, Vol. 26, No. 1, 2000, pp. 38–41.

A New Approach to the Creation of Nanoelectronic Systems Using a Dimensionally-Quantized Potential Relief of Charges Built into Insulating Layers on a Semiconductor Surface

E. I. Gol'dman and A. G. Zhdan

Fryazino Department, Institute of Radio Engineering and Electronics, Russian Academy of Sciences, Fryazino, Moscow oblast, Russia

Received August 27, 1998

Abstract—A new approach to obtaining rearrangeable nanoscale low-dimensional electronic systems is analyzed. The method consists in creating a regular local charge density distribution in an insulator layer contacting with a semiconductor so as to induce a two-dimensional potential relief in the near-surface region of the semiconductor. A desired built-in charge density distribution profile can be created, for example, by scanning over the insulator surface with a probing point of a tunneling microscope. This profiling allows, in principle, various dimensionally-quantized structures to be obtained including quantum wells, dots, wires, superlattices, etc. The prospects for realization of the proposed approach are considered in application to the silicon–silicon oxide system. © *2000 MAIK "Nauka/Interperiodica".*

Modern approaches to the organization of nanoelectronic systems are based on the conventional methods of epitaxial growth, local doping, lithography, etc. [1] and on some new methods of surface modification, such as the electric force action of the probing point of a scanning tunneling microscope [2]. Below we will consider a principally new approach to creating surface elements and structures on a nanometer scale, based on a regular variation of the charged state in a layer of insulator contacting with a semiconductor. The formation of certain local charge density distribution in the insulator, inducing the corresponding two- dimensional potential relief in a near-surface layer of the semiconductor, would allow us to obtain various low-dimensional structures in the system, including quantum wells, dots, wires, superlattices, etc.

We will analyze the prospects for realization of the proposed principle in application to the silicon–silicon oxide system, which allows us to combine the unique physicochemical properties with highly developed technologies available. There is a number of methods providing for the creation of built-in charges in the oxide layer, of which we will consider two techniques: (1) the injection and trapping of electrons (holes) in the SiO_2 bulk or at a SiO_2–Si_3N_4 interface and (2) the migration of ions over the oxide and their interaction with electrons in the near-surface layer of silicon. On the dimensional quantization scale ($\delta \cong 100$ Å), a potential relief amplitude of the order of $\Delta U \cong 1$ eV is provided by the amplitude of modulation of the built-in charge density $\Delta N_s = 5 \times 10^{13}$ cm^{-2} ($\Delta U \sim q^2 \Delta N_s \delta/\xi$, where q is the elementary charge and ξ is the average dielectric permittivity at the interface). The built-in electron (or hole) densities on this level are quite readily obtained by the tunneling or avalanche carrier injection into the oxide during exposure to non-damaging electric fields ($\leq 5 \times 10^6$ V/cm) [3, 4]. The injected charge is characterized by a prolonged (up to 10^8 s) lifetime, for example, in the storage devices based on the electron states localized at the tunneling oxide–silicon nitride contact [5]. Sufficiently high surface charge densities $N_s \approx 3 \times 10^{13}$ cm^{-2} are also created by alkali metal ions migrating in the oxide at elevated temperatures (≥100°C) in polarizing electric fields of the order of $\approx 1 \times 10^5$ V/cm [7].[1] The duration of storage of the charge created by these methods in the oxide layer contacting with the silicon surface exceeds 10^8 s at room temperature (and is even longer at lower temperatures, where the quantum effects are most clearly pronounced) and the migration activation energies typically reach 0.8–1.5 eV [8, 9].

Thus, the task of creating nanoelectronic systems reduces to a variation of the built-in charge density over the insulator–semiconductor interface.

A well-known property of the electron and ion charges built into an insulator is the ability of inducing the formation of spontaneous submicron structures affecting the electron characteristics of silicon at the silicon–oxide interface [10, 11]. For example, the drift of mobile positive ions in SiO_2 toward the interface is accompanied by the formation of stable built-in charge

[1] According to some data [6], the migration of ions in silicon oxide is observed at or even below room temperature.

1063-7850/00/2601-0019$20.00 © 2000 MAIK "Nauka/Interperiodica"

spots with a number density of $\geq 10^{13}$ cm^{-2} and a size of the order of ~100 Å. The edge fields of these spots were reported to generate minor charge carriers due to the Franz–Keldysh effect [11]. Although the charge spots seem to be randomly distributed over the surface, electrons in the potential wells created by these spots must possess properties typical of the zero-dimensional systems.[2]

Creation of a regular built-in charge distribution with a certain scale at the insulator–semiconductor interface is possible, for example, with the aid of a modern scanning tunneling microscopy technique. The local density of the built-in charge is determined by the point–semiconductor potential difference and the duration of exposure in a given site, while the size of the charged region depends on the gap between the point and the semiconductor surface (i.e., by the insulating layer thickness). The last circumstance does not restrict the possibility of creating the dimensionally-quantized structures by this method, since high-quality insulating layers in the Si–SiO_2 system can be obtained beginning with thicknesses of the order of ~10 Å.

Although the proposed approach to creation of the dimensionally-quantized systems is evidently quite realistic, there are virtually no investigations in this direction. A work which is close to our approach in methodological aspect was performed at the Stanford University (USA) [12], where a local recharge of boundary states was studied in a Si_3N_4–SiO_2–Si structure. Experiments performed under non-optimum conditions (using an insulating layer with a total thickness of 500 Å) allowed a spatial resolution of 1500 Å to be obtained at a data storage time (for a 128×128 dot matrix) of about 7 days [12].[3]

In conclusion, we would like to indicate some interesting ways to expand the functional abilities of quantum elements and nanoelectronic systems by using a layer of oxide saturated with ferromagnetic ions. As is known, for example, positive iron ions exhibit mobility in SiO_2. The electron levels related to these ions are localized at the Si/SiO_2 interface and characterized by energies below the conduction band of silicon [14], which allows their charged state to be modified by means of the field effect. A change in the arrangement of these ions would allow us to create, in addition to the potential relief, a magnetic relief that can be controlled by applying a comparatively small external magnetic field and changing the degree of electron enrichment in the surface layer. This provides additional degrees of freedom for controlling the related nanoelectronic systems. Some particular effects of this type observed in systems with homogeneous properties along the interphase boundary were studied in [15]. It should be also noted that the proposed approach is also characterized by inherent possibility of producing rearrangements (erasing, rewriting) in the low-dimensional systems under consideration.

[2] Mechanisms involved in the formation of these charged spots admit, in principle, the appearance of self-organized ordered low-dimensional structures.

[3] It is a remarkable fact that a physically analogous search for nontraditional technologies is conducted in the field of macroelectronics. By freezing an ion relief created using a thermal–field treatment of a system possessing a mixed ion–electron conductivity, it is possible to obtain effective rectifying and light-emitting elements based on the *p–i–n* transitions induced by a localized space charge of ions [13].

REFERENCES

1. Abstracts of Papers of the *3rd All-Russia Conference on the Physics of Semiconductors "Semiconductors-97"* [in Russian] (FIAN, Moscow, 1997).
2. P. N. Luskinovich and V. I. Nikitin, Élektron. Tekh., Ser. 3, Mikroélektron., No. 3, 27 (1991).
3. S. T. Sah, Solid-State Electron. **33** (2), 147 (1990).
4. D. J. Di Maria and J. W. Stasiak, J. Appl. Phys. **65** (6), 2342 (1989).
5. V. I. Belyĭ, L. L. Vasil'eva, V. A. Gritsenko, *et al.*, in *Silicon Nitride in Electronics* [in Russian], Ed. by A. V. Rzhanov (Nauka, Novosibirsk, 1982).
6. M. W. Hillen and D. G. Hemmes, Solid-State Electron. **24** (8), 773 (1981).
7. T. W. Hicmott, J. Appl. Phys. **46** (6), 2583 (1975).
8. M. R. Boudry and J. P. Stagg, J. Appl. Phys. **50** (2), 942 (1979).
9. J. P. Stagg and M. R. Boudry, J. Appl. Phys. **52** (2), 885 (1981).
10. E. I. Gol'dman, A. G. Zhdan, and A. M. Sumaroka, Pis'ma Zh. Éksp. Teor. Fiz. **57** (12), 783 (1993).
11. E. I. Gol'dman, A. G. Zhdan, and A. N. Ponomarev, Fiz. Tekh. Poluphovod. **28** (11), 1947 (1994).
12. R. C. Barrel and C. F. Quate, J. Appl. Phys. **70** (5), 2725 (1991).
13. J. Gao, G. Yu, and A. J. Heeger, Appl. Phys. Lett. **71** (10), 1293 (1997).
14. V. N. Vertoprakhov, B. M. Kuchumov, and E. G. Sal'man, in *The Structure and Properties of Si–SiO_2–M Structures* [in Russian] (Nauka, Novosibirsk, 1981).
15. Yu. I. Balkareĭ, V. N. Lutskiĭ, and V. A. Petrov, Pis'ma Zh. Éksp. Teor. Fiz. **54** (8), 449 (1991).

Translated by P.P. Pozdeev

Technical Physics Letters, Vol. 26, No. 1, 2000, pp. 21–22. Translated from Pis'ma v Zhurnal Tekhnicheskoĭ Fiziki, Vol. 26, No. 1, 2000, pp. 42–44.

A New Monopole Mass-Analyzer Based on a Hyperboloid Electrode System

É. P. Sheretov, V. S. Gurov, M. V. Dubkov, and O. V. Korneeva

Ryazan State Radio Engineering Academy, Ryazan, Russia

Received July 14, 1999

Abstract—A new version of the monopole mass spectrometer with improved characteristics, which advances the idea of the quadrupole analyzer, is described. © *2000 MAIK "Nauka/Interperiodica".*

The monopole mass analyzer proposed by Ulf von Zahn [1] comprises a rodlike electrode of a circular (*1*) or a hyperbolic (*2*) section and an angle electrode (*3*) formed by two perpendicular planes (Fig. 1). A serious drawback of such a monopole is the insufficience of a good shape of the mass peak due to the presence of tails on the heavy-mass side of the peak, which restricts resolution, relative sensitivity, and the possibility of analyzing small components.

Theoretical calculations, which we carried out earlier [2], showed that replacing an angle electrode *3* by a hyperbolic one *4* (Fig. 1) substantially improves the shape of the mass peak and the resolution of the monopole, but does not affect the analyzer sensitivity. The geometry of the rodlike electrode and the radius R_0 of the electrode system remain unchanged, as well as the quadratic distribution of the potential in this system. The improvement in parameters is achieved due to the absence in the new monopole of the near-axial region with an electric field of zero strength, and to the fact that ions are injected into the analyzer with the initial coordinates $y_0 \geq r_0$, where r_0 is the geometric parameter of the hyperbolic angle electrode, whose shape is described by the equation $y^2 - x^2 = r_0^2$ (the case $r_0 = 0$ corresponds to the angle electrode of the known Zahn monopole). For example, an increase in the geometric parameter r_0 of the angle electrode from 0 to $0.05R_0$ allows the relative sensitivity to be increased by at least a factor of 10^2–10^3. The resolution at a level of 0.01 then increases by about 2.5–3 times.

The new geometry of the monopole is implemented in practice only with the use of the unique technology of producing electrode systems of a complex shape, which has been developed by us within the International Space Project Venus–Comet Halley [3].

The monopole with the new geometry of electrodes has an electrode system 200 mm long, a field radius $R_0 = 6$ mm, and a geometric parameter of the angle electrode $r_0 = 0.1R_0$. Thin-walled electrodes are made of 1-mm-thick copper and are covered by a protective gold layer. The mass of the assembled analyzer is 180 g.

Ions with an energy of 2 eV or higher are injected from the ion source into the mass analyzer parallel to the rodlike electrode near the axis through a 1-mm circular opening in the 6-mm-thick diaphragm. The exit diaphragm has a triangular opening with an area of 36 mm^2. The electrode system is fed from a specially designed HF oscillator with a harmonic signal, variable amplitude (up to 450 V), and frequency scanning of the mass spectrum. The scanning is accomplished by varying the radio frequency in the range from 900 to 4500 kHz.

Figure 2a shows a typical fragment of the mass spectrum of a residual gas in the metallic sputter-ion pumped-out vacuum system. The mass spectrum is obtained with the new monopole for the ion input energy of 8 eV with the slope of the operating curve $\lambda = a/q = 0.144$ (Fig. 2a). Experimental resolution for the mass peak 28 amu and $\lambda = 0.173$ (Fig. 2b) is 825 at a level of 0.5; 410 at a level of 0.1; and 200 at a level of 0.01, which is much better than the values known from literature [1, 4].

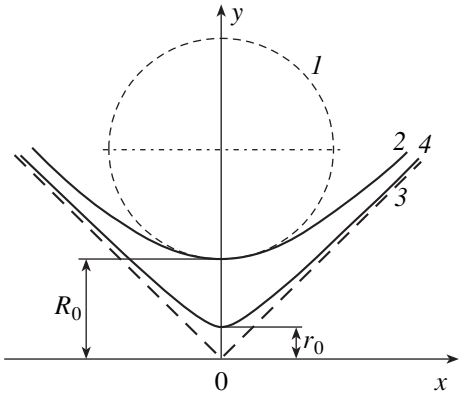

Fig. 1. Geometry of monopole mass analyzers: (*1*, *3* or *2*, *3*) Zahn's monopole; (*2*, *4*) new monopole based on the hyperboloid electrode system.

1063-7850/00/2601-0021$20.00 © 2000 MAIK "Nauka/Interperiodica"

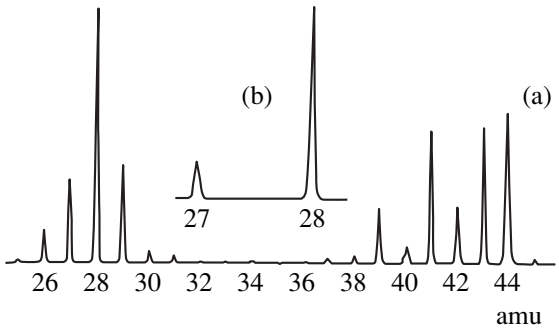

Fig. 2. Fragments of mass spectra obtained with the new monopole for the input ion energy 8 eV, and a/q = (a) 0.144 and (b) 0.173.

We compared the shape of the experimental mass peak obtained with the new monopole with the peak recorded in the analyzer fitted with the monopole of traditional geometry, produced in our laboratory by the same technology. The latter has a length of 200 mm and a field radius of 6 mm. The results of comparison are as follows. For the same operating modes and input ion energies, the resolution achieved with the new monopole at different levels of determination (0.5, 0.1, 0.01, and 0.001) is higher by a factor of 3–4 than the resolution of the conventional monopole, while the relative sensitivity obtained is higher by a factor of 10^2, attaining 10^{-5}.

This opens up wide opportunities for using such instruments for microanalysis, while the combination of high analytical characteristics with a small size and mass, provided by the new technology for their fabrication, makes them especially attractive for use in conditions of mobile laboratories.

REFERENCES

1. Ulf von Zahn, Rev. Sci. Instrum. **34**, 1 (1963).
2. É. P. Sheretov, V. S. Gurov, and M. V. Dubkov, in *Proceedings of International Conference "Scientific Foundations of High Technologies," Novosibirsk* (1997), Vol. 1, pp. 63–66.
3. É. P. Sheretov, V. S. Gurov, and M. V. Dubkov, in *Proceedings of 14th International Mass Spectrometry Conference, Helsinki, 25–29 August 1997*, p. 229.
4. P. H. Dawson and N. R. Whetten, in *Dynamic Mass Spectrometry*, Ed. by D. Price and J. E. Williams (Heyden, London, 1970), Vol. 1, pp. 1–60.

Translated by A. Kozlenkov

Technical Physics Letters, Vol. 26, No. 1, 2000, pp. 23–25. Translated from Pis'ma v Zhurnal Tekhnicheskoĭ Fiziki, Vol. 26, No. 1, 2000, pp. 45–49.

Raman Lidar for Remote Sensing of Sulfur-Containing Hydrocarbons in the Atmosphere

S. V. Merkur'ev, V. E. Privalov, and V. G. Shemanin

Baltic State Technical University, St. Petersburg, Russia

Received June 25, 1999

Abstract—It is demonstrated that remote detection of the maximum permissible concentrations of dangerous substances (hydrogen sulfide, mercaptan, ethylmercaptan) is possible only at inadmissibly short distances. *© 2000 MAIK "Nauka/Interperiodica".*

The monitoring of sulfur-containing hydrocarbons in the atmosphere is an important problem because of their very low maximum permissible concentration (MPC) (up to 10^{-5} mg/m^3 [1]) and high toxicity. This work aimed at obtaining a numerical solution of the lidar equation for a 180° vibrational Raman scattering from hydrogen sulfide, mercaptan, and ethylmercaptan molecules under the conditions of daytime probing, which is necessary for selecting the laser wavelength and obtaining a maximum power of the Raman scattering signal at the lidar photodetector.

Similarly to the previous works [2–5], we consider the following possible variants: copper vapor laser (578.2, 510.6, 289.1, 255.3 nm and a sum frequency corresponding to 271.2 nm) with peak powers up to 100 kW [6], $XeCl_2$ excimer laser (308 nm) [7], and Nd-YAG laser (532, 355, 266 nm harmonics) with the same peak powers [7].

The frequencies of the SH stretching vibrations ν of the molecules under study were taken from [7, 8] for H_2S and from [9] for CH_3SH and C_2H_5SH. The CH stretching frequencies of the latter two molecules were taken from [9]. All these frequencies are listed in the table. Using these values, we calculated the wavelengths of the Raman bands λ for the selected laser wavelengths λ_0 [3]. These results are also presented in the table.

The differential cross sections ($d\sigma/d\Omega$) of Raman scattering of the molecules under study for the selected laser wavelengths were determined, as in [3], on the basis of cross sections experimentally measured for the excitation wavelength λ_0 = 337.1 nm (nitrogen laser) [7] (see table). The cross sections for ethylmercaptan were

Frequencies of SH and CH stretching vibrations, wavelengths of Raman bands, and differential Raman cross sections of the hydrocarbon molecules under study for various laser wavelengths

Molecule		H_2S		CH_3SH				C_2H_5SH		
$\tilde{\nu}$, –"$^{-1}$	2611		2572		2931		2570		2930	
λ_0, nm	λ, nm	$\left(\frac{d\sigma}{d\Omega}\right)\times 10^{30}$	λ, nm	$\left(\frac{d\sigma}{d\Omega}\right)\times 10^{30}$	λ, nm	$\left(\frac{d\sigma}{d\Omega}\right)\times 10^{30}$	λ, nm	$\left(\frac{d\sigma}{d\Omega}\right)\times 10^{30}$	λ, nm	$\left(\frac{d\sigma}{d\Omega}\right)\times 10^{30}$
266	285.9	49.0	285.5	49.0	288.5	19.3	285.5	49.0	288.5	177.0
355	391.3	15.4	390.7	15.4	396.2	6.1	390.6	15.4	396.2	55.8
532	617.8	3.1	616.3	3.1	630.3	1.2	616.3	3.1	630.2	11.1
308	334.9	27.2	334.5	27.3	338.6	10.8	334.5	27.2	338.6	98.5
578	680.7	2.2	678.9	2.2	695.9	0.9	678.8	2.2	695.8	7.9
510	588.3	3.6	587.0	3.6	599.6	1.4	586.9	3.6	599.6	13.1
289	312.6	35.1	312.2	35.2	315.7	13.9	312.2	35.1	315.7	127.0
271	291.6	45.4	291.3	45.5	294.4	18.0	291.3	45.4	294.4	164.3
255	273.2	58.0	272.9	58.0	275.6	22.9	272.9	58.0	275.6	209.6
	337.1	19.0								

1063-7850/00/2601-0023$20.00 © 2000 MAIK "Nauka/Interperiodica"

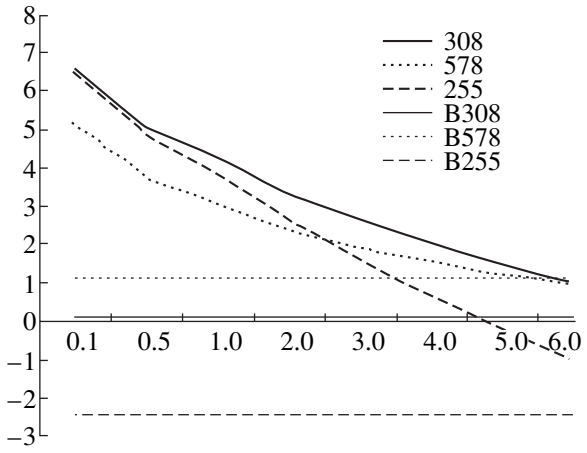

Fig. 1. Logarithmic plots of the power of Raman signal for ethylmercaptan at a concentration of 10^{19} cm^{-3} vs. probing distance for several selected wavelengths. For comparison, horizontal lines show the levels of minimum power detected by the lidar P_b calculated for the given experimental conditions.

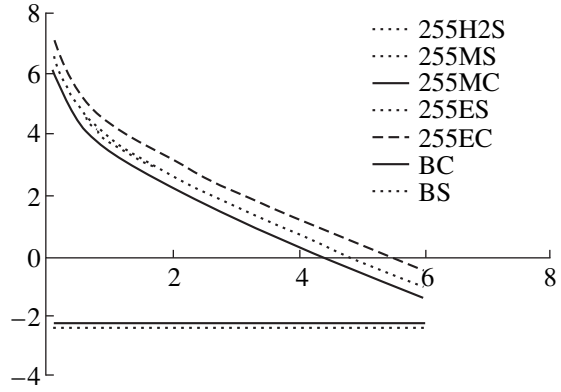

Fig. 2. Logarithmic plots of the power of Raman signal for hydrogen sulfide, mercaptan, and ethylmercaptan molecules at a concentration of 10^{19} cm^{-3} for the laser wavelength 255 nm vs. the probing distance. For comparison, horizontal lines show the levels of minimum power detected by the lidar P_b at the same wavelength under the given experimental conditions.

estimated using the known values for methane and butane [7].

The lidar equation for Raman scattering can be considered in the same form as in [2] with the values of parameters from [4, 5]. Numerical calculations of the Raman signal power were performed for a molecule concentration of 10^{19} cm^{-3} and the probing distances R = 0.1, 0.5, 1.0, 2.0, 3.0, 4.0, 5.0, and 6.0 km.

As in [4, 5], we determined the values of the background power at the detector $P_b(\lambda, R)$ and minimum detectable power P_m under the conditions of daytime probing using the values of the spectral brightness of sunlight for the Raman scattering wavelengths of the molecules under study $S_b(\lambda)$ summarized in the table.

The results of calculations for ethylmercaptan molecules (SH bands, laser wavelengths 255, 308, and 578 nm) are presented in Fig. 1. The same figure shows the levels of the minimum power P_b detect by lidar calculated for our experimental conditions at each of the wavelengths employed [4, 5]. For the laser wavelengths 255 and 578 nm, the calculated power is higher than the background level for all the probing distances and the substance concentration of 10^{19} cm^{-3}. For the wavelength 308 nm, the minimum detected power is above the background level only for the distances not exceeding 5 km.

Figure 2 shows the results of calculations for both bands of the molecules under study with a concentration of 10^{19} cm^{-3} for the laser wavelength 255 nm and a probing distance of 6 km. For comparison, we also present the background levels for both Raman bands at this wavelength. The calculated values of detected power for ethylmercaptan are greater than those for the SH band of hydrogen sulfide, mercaptan, and ethylmercaptan, which were virtually identical and higher than the powers calculated for the CH band of mercaptan. This distribution reflects a relationship between the differential cross sections of the molecules studied. No one of the curves crosses the background level within the entire range of the probing distances.

Using the data from [1], according to which the MPC values are 0.008 mg/m^3 (1.42×10^{11} cm^{-3}) for hydrogen sulfide, 9×10^{-6} mg/m^3 (1.13×10^8 cm^{-3}) for mercaptan, and 3.0×10^{-5} mg/m^3 (2.9×10^8 cm^{-3}) for ethylmercaptan, we estimated the maximum probing distances at which the detection of these molecules is possible at the MPC levels. An analysis of these data shows that detection of the MPC of hydrogen sulfide is possible at a distance of up to 200 m for the laser wavelengths 266 and 271 nm, 150 m for the wavelength 289 nm, 100 m for the wavelength 255 nm, and 50 m for the wavelength 308 nm. Detection of the MPC of mercaptan is possible only using the SH band at a distance of up to 10 m for the laser wavelengths 266 and 271 nm, and up to 5 m for the wavelength 255 nm. The maximum distances for ethylmercaptan probed at the same wavelengths are 30 and 10 m, respectively. The maximum probing distances for the CH band are 40 m (271 nm), 20 m (266 nm), and 10 m (255 nm).

Therefore, optimum results in the given lidar system are obtained using the radiation of a copper vapor laser (271.2 nm) and the fourth harmonic of an Nd-YAG laser (266 nm), which allow one to reach the maximum distances of probing for concentrations of the molecules studied at the MPC level in atmosphere under the daytime conditions.

REFERENCES

1. *The List and Codes of Atmospheric Pollutants* [in Russian] (Research Institute of Atmospheric Air Protection, St. Petersburg, 1992).
2. V. E. Privalov and V. G. Shemanin, Opt. Spektrosk. **82** (4), 700 (1997) [Opt. Spectrosc. **82** (4), 650 (1997)].
3. V. E. Privalov and V. G. Shemanin, Proc. SPIE **3345**, 6 (1998).
4. G. V. Laktyushkin, V. E. Privalov, and V. G. Shemanin, Pis'ma Zh. Tekh. Fiz. **24** (4), 32 (1998) [Tech. Phys. Lett. **24** (2), 138 (1998)].
5. V. E. Privalov and V. G. Shemanin, Opt. Spektrosk. **85** (1), 161 (1998) [Opt. Spectrosc. **85** (1), 147 (1998)].
6. S. A. Vitsinskiĭ, V. D. Divin, A. V. Keller, I. L. Lovchiĭ, and A. A. Svetlykh, Opt. Zh., No. 5, 83 (1996).
7. R. M. Measures, *Laser Remote Sensing: Fundamentals and Applications* (Wiley, New York, 1984; Mir, Moscow, 1987).
8. W. F. Murphy, W. Holzer, and H. J. Bernsteĭn, Appl. Spectrosc. **23** (3), 211 (1969).
9. L. M. Sverdlov, M. A. Kovner, and E. P. Kraĭnov, *Vibrational Spectra of Polyatomic Molecules* [in Russian] (Nauka, Moscow, 1970).

Translated by A. Chikishev

Technical Physics Letters, Vol. 26, No. 1, 2000, pp. 26–28. Translated from Pis'ma v Zhurnal Tekhnicheskoĭ Fiziki, Vol. 26, No. 1, 2000, pp. 50–55.

Stabilization of Luminous Properties of Porous Silicon by Vacuum Annealing at High Temperatures

B. M. Kostishko, I. P. Puzov, and Yu. S. Nagornov

Ul'yanovsk State University, Ul'yanovsk, Russia

Received February 5, 1999

Abstract—The degradation properties of porous silicon caused by vacuum annealing at high-temperatures have been measured. Vacuum annealing within the temperature range of 150–300°C provided the complete removal of water molecules from the pore surface and partial destruction of hydrogen complexes. Our studies showed that vacuum annealing at 150°C considerably stabilizes the luminous properties of porous silicon: the subsequent UV-irradiation of silicon specimens changed the photoluminescence intensity only by 8–10% of its initial value. *© 2000 MAIK "Nauka/Interperiodica".*

Despite a large number of research groups studying porous silicon, all the attempts to create reliable and stable light-emitting devices on its basis have failed. Therefore, interest in various applications of porous silicon has been considerably reduced. However, the fundamental studies of this unique material have not ceased. Moreover, the number of related studies steadily increases. This is associated with the fact that porous silicon, which can be obtained by extremely simple technology, possesses the properties that can be interpreted within different models and approaches. It should be mentioned that there exists more than five mechanisms of visible photoluminescence [1]. Each of the corresponding five models has its ardent supporters and is confirmed by numerous experimental data.

To all appearances, the studies of porous silicon become ever more concentrated on the search for ways and technologies stabilizing its luminous properties. The most promising results in this field were obtained using fast high-temperature oxidation [2, 3], laser modification of the initial substrates [4], and carbonization [5]. Moreover, some studies make use of vacuum annealing of porous silicon at high temperatures [6, 7]. However, all these studies take into account surface stabilization caused by the removal of water molecules, but ignore the changes in the luminous properties of porous silicon caused by such a treatment. In this connection, we present here the results of our studies of changes in the photostimulated evolution of photoluminescence of porous silicon upon vacuum annealing in the temperature range of 150–300°C.

Porous silicon was obtained using the standard technology of electrochemical etching in the HF/C_2H_5OH (1 : 1) solution. The starting material was a (100)-oriented phosphorus-doped single crystal silicon wafer with the resistivity $\rho = 32\ \Omega$ cm. The as-prepared porous silicon specimens were placed into a vacuum chamber of an 09IOS-10-005 Auger spectrometer and were heated there by a wide electron beam directed toward the back side of the holder. A 2-h annealing was performed at various temperatures in the range of 150–300°C. The residual pressure in the chamber did not exceed 10^{-5} Pa. The fluorescence spectra were obtained on a DFS-52 spectrometer at room temperature. Excitation was attained with the aid of the DKsSh-150 lamp at the wavelength of 360 nm. In order to avoid possible thermal effects at the specimen surface, the specimens were irradiated with an intensity not exceeding $P = 50$ mW/cm^2.

Figure 1 shows the experimental data on the variations of the intensity and the position of the spectral maximum for specimens annealed in vacuum at 150 and 300°C (series *A* and *B*, respectively). The fluorescence spectra were recorded in air immediately upon

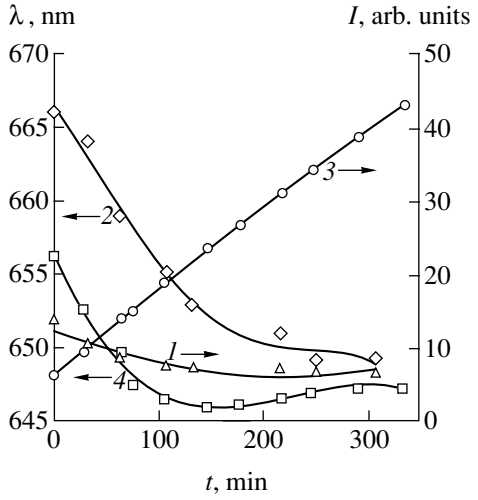

Fig. 1. (*1* and *3*) Intensity and (*2* and *4*) wavelength of the spectral maximum of photoluminescence as functions of the exposure to UV radiation. Annealing temperature: (*1* and *2*) 150°C, (*3* and *4*) 300°C.

1063-7850/00/2601-0026$20.00 © 2000 MAIK "Nauka/Interperiodica"

the specimen removal from the vacuum chamber. As is seen, the spectra and the kinetics of their variation under the UV-irradiation are essentially dependent on the annealing temperature used. An increase in the temperature from 150 to 300°C resulted in luminescence quenching by more than twice. The subsequent 5.5-h illumination with the UV-light of the specimens of series *A* led to slight fluorescence quenching and the shift of the spectral maximum to the short-wave range by 8 nm. The specimens of series *B* showed similar changes in the position of the intensity maximum, but, instead of fluorescence quenching, they showed a sevenfold rise of the photoluminescence emission.

The difference in the degradation characteristics is attributed to the fact that at the temperatures used, different components are desorbed from the surface. Annealing at 150°C results in the maximum possible rate of water-molecules desorption [8]. An increase of the annealing temperature up to 250°C gives rise to a drastic increase in the desorption rate of hydrogen molecules H_2 [8], although the efficient destruction of SiH_2-groups on the surface of quantum wires and the subsequent desorption of molecular hydrogen can occur only at temperatures higher than 300°C (the IR-data [9]).

The UV-irradiation of the specimens provides the occurrence of several photo-stimulated reactions on the pore surfaces [10, 11]. Two of these reactions reduce to the reversible destruction of the hydrogen- and carbon-containing groups remaining on the surface. Both reactions are associated with the formation of dangling bonds, and centers of radiationless recombination, and, as a consequence, with fluorescence quenching. Along with these reactions, one also observes healing of the centers of radiationless recombination during surface oxidation.

The above experimental data lead to a conclusion that vacuum annealing at temperatures lower than the critical one (300°C) is accompanied by partial destruction of hydrogen groups. Exposure of such specimens to light results in an accelerated formation of SiO_x groups and the rise of the photoluminescence emission. The shift of the spectral maximum to the short-wavelength range is also associated with surface oxidation [2, 3]. The fact that for specimens of series *B*, this shift is observed at 17 nm and not at 8 nm (as for specimens of series *A*) also confirms the oxidation hypothesis. The rise of photoluminescence emission up to values exceeding those observed for as-prepared specimens and specimens of the series *A* is explained by the fact that the complete substitution of hydrogen groups by oxygen ones increases the luminescence by almost five times [12].

In most of the studies, the use is made not of the as-prepared specimens but of the specimens stored for weeks and even months in air. During such storage, the composition of the specimens surface is stabilized, thus preventing the effect of aging. Therefore, of special

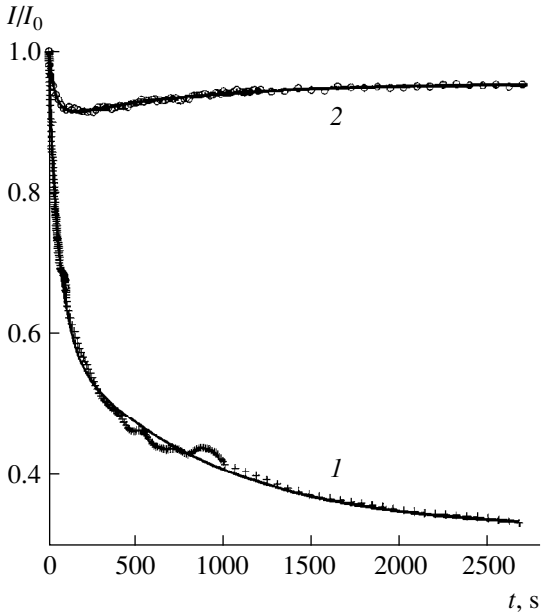

Fig. 2. Integrated photoluminescence intensity of porous silicon specimens stored for two weeks in air as a function of exposure to laser radiation. The data are normalized to the initial intensity I_0; (*1*) as-prepared specimen, (*2*) specimen upon annealing in vacuum at 150°C.

interest is the stability of luminous characteristics of porous silicon, which upon its vacuum annealing at high temperatures, was stored in an oxygen-containing atmosphere. Figure 2 shows the curves of the integrated intensity of photoluminescence for an as-prepared specimen and a specimen of the *A* series as functions of the time of irradiation with the light from an LGN-409 He–Cd laser (λ = 325 nm, P = 40 mW/cm^2). Prior to irradiation, the specimens were stored for two weeks in darkness in the air atmosphere. The continuous lines were calculated according to the kinetic model of photostimulated evolution of photoluminescence from porous silicon [10, 11]. The analysis of these lines leads to the following conclusions. On the decreasing segment of photoluminescence, the specimens of the series *A* almost do not have the component caused by photostimulated cleaning of the pore surface from carbon-containing molecules. The fluorescence intensity decreases only by 8.5%; whereas, in the control specimen, it attains the value of 75%. The rate of photoluminescence quenching upon annealing increases by almost a factor of two, and the intensity starts increasing already upon four minutes of specimen irradiation. The rise in the fluorescence emission for the initial specimens of porous silicon at the laser power indicated above was observed only upon one hour specimen irradiation.

Thus, annealing in vacuum at the temperature corresponding to the maximum rate of H_2O thermodesorption (150°C) results in the removal of volatile carbon-containing molecules from the surface of porous silicon

and an essential stabilization of its photoluminescence. An increase of the annealing temperature up to 300°C gives rise to partial destruction of hydrogen groups and formation of the centers of radiationless recombination. A further UV-irradiation of the specimen results in intense additional oxidation of the surfaces of quantum wires, healing of the quenching centers, and an increase of the photoluminescence intensity.

ACKNOWLEDGMENTS

The study was supported by the programs *Russian Universities: Fundamental Studies* and *Materials, Structures, and Devices for Semiconductor Optoelectronics.*

REFERENCES

1. A. G. Cullis, L. T. Canham, and P. D. J. Calcott, J. Appl. Phys. **82** (3), 909 (1997).
2. G. G. Qin, H. Z. Song, B. R. Zhang, *et al.*, Phys. Rev. B: Condens. Matter **54** (4), 2548 (1996).
3. J. Lin, L. Z. Zhang, B. R. Zhang, *et al.*, J. Phys.: Condens. Matter **6**, 565 (1994).
4. L. L. Fedorenko, A. D. Sardarly, É. B. Kaganovich, *et al.*, Fiz. Tekh. Poluprovodn. (St. Petersburg) **31** (10), 6 (1997).
5. B. M. Kostishko, Sh. R. Atazhanov, and S. N. Mikov, Pis'ma Zh. Tekh. Fiz. **24** (16), 24 (1998) [Tech. Phys. Lett. **24** (8), 633 (1998)].
6. P. K. Kashkarov, E. A. Konstantinova, S. A. Petrov, *et al.*, Fiz. Tekh. Poluprovodn. (St. Petersburg) **31** (6), 745 (1997).
7. K. N. El'tsov, V. A. Karavanskiĭ, and V. V. Martynov, Pis'ma Zh. Éksp. Teor. Fiz. **63** (2), 106 (1996) [JETP Lett. **63** (2), 119 (1996)].
8. V. A. Kiselev, S. V. Polisadin, and A. V. Postnikov, Fiz. Tekh. Poluprovodn. (St. Petersburg) **31** (7), 830 (1997) [Semicond. **31** (7), 704 (1997)].
9. C. Tsai, K.-H. Li, J. Sarathy, *et al.*, Appl. Phys. Lett. **59** (22), 2814 (1991).
10. B. M. Kostishko, A. M. Orlov, and T. G. Emel'yanov, Pis'ma Zh. Tekh. Fiz. **22** (10), 68 (1996) [Tech. Phys. Lett. **22** (5), 417 (1996)].
11. B. M. Kostishko and L. I. Gonchar, Pis'ma Zh. Éksp. Teor. Fiz. **66** (5), 357 (1997) [JETP Lett. **66** (5), 382 (1997)].
12. A. Nakajima, T. Itakura, S. Watanabe, *et al.*, Appl. Phys. Lett. **61**, 46 (1992).

Translated by L. Man

Technical Physics Letters, Vol. 26, No. 1, 2000, pp. 29–30. Translated from Pis'ma v Zhurnal Tekhnicheskoĭ Fiziki, Vol. 26, No. 1, 2000, pp. 56–60.

Modeling of the Time Characteristics of Luminance in Thin-Film Electroluminescent Structures

E. E. Zabudskiĭ and M. K. Samokhvalov

Ul'yanovsk State Technical University, Ul'yanovsk, Russia

Received June 4, 1999

Abstract—The pattern of luminance waves in thin-film electroluminescent structures was modeled and the duration of transient lighting processes in these systems was determined. A principle of the indicator display control is formulated which provides for a maximum luminance of the light-emitting devices. © *2000 MAIK "Nauka/Interperiodica".*

At present, thin-film electroluminescent (TFEL) structures of the metal–insulator–luminophor–insulator–transparent electrode type controlled by ac voltages offer the most promising flat light-emitting devices. Mathematical modeling of the TFEL structures helps to elucidate the laws of electron processes occurring in these systems, establish optimum regimes of luminescence excitation, and develop TFEL based devices capable of displaying images (including matrix systems). The approach to modeling the parameters of TFEL devices can be divided into two stages: (1) determination of the electric characteristics of thin-film light-emitting elements [1] and (2) calculation of the lighting parameters of display devices based on the results of the first stage.

A special feature of analysis of the optical and electric properties of the electroluminescent devices in which the emission is excited by ac voltages is the periodic character of variation of the main characteristics. In the steady-state excitation regime, the charge, current, dissipated power, and emission luminance (photometric brightness) of an electroluminescent device vary in a consistent manner within every period of operation, so that the characteristics can be considered as interrelated and expressed by values averaged over the period [2]. At the same time, study of the transient processes in TFEL structures, which is of primary importance for development of the optimum regimes and schemes of excitation of the display devices, allows us to determine the time characteristics of luminance of these light-emitting systems.

Dependence of the electroluminescence parameters on the applied voltage is determined by the field-induced process of electron tunneling, that is, by the rate of carrier production, rather than by the electron acceleration in the luminophor film. The impact excitation kinetics is determined by the rate of variation of the density of excited emission centers in the luminophor [3, 4]:

$$\frac{dN^*(t)}{dt} = \frac{\sigma}{e} j(t)[N - N^*(t)] - \frac{N^*(t)}{\tau}, \qquad (1)$$

where N^* is the concentration of excited centers; N is the concentration of emitting centers, σ is the impact ionization cross-section; e is the electron charge; τ is the time constant of relaxation related to radiative transitions to the ground state; and $j(t)$ is the active current density in the active layer.

The instantaneous luminance of emission from an electroluminescent structure depends on the rate of transition of the emitting centers from excited to ground state:

$$B(t) = \eta_c d_{ph} \frac{N^*(t)}{\tau}, \qquad (2)$$

where d_{ph} is the luminophore thickness and η_c is the efficiency of the light yield. The latter quantity is determined by optical constants of the materials used:

$$\eta_c = \frac{K_\lambda}{\pi} h\nu \eta_s, \qquad (3)$$

where K_λ is the visibility factor determining conversion of the energy characteristics of emission into the values characterizing the light perception properties of the human eye; $h\nu$ is the emitted photon energy; η_s is a coefficient determined as the ratio of the number of photons emitted from the surface of the electroluminescent capacitor to the total number of photons generated within the luminescent layer volume.

Substituting formula (2) into equation (1), we obtain an ordinary differential equation of the first order:

$$\frac{dB(t)}{dt} = \frac{\sigma}{e} j(t)\left[\frac{N\eta_c d}{\tau} - B(t)\right] - \frac{B(t)}{\tau}. \qquad (4)$$

A solution to this equation determined a time variation of the instantaneous emission luminance of the

1063-7850/00/2601-0029$20.00 © 2000 MAIK "Nauka/Interperiodica"

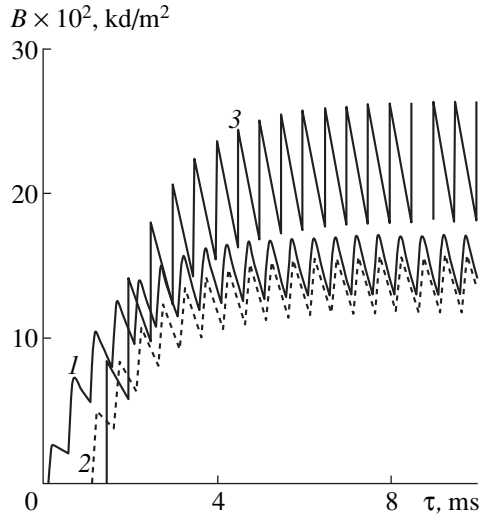

Luminance waves in a TFEL structure excited by alternating-sign voltage pulses of various shapes: (*1*) sinusoidal; (*2*) triangular; (*3*) rectangular.

TFEL structure studied (i.e., the luminance wave). Equation (4) is nonlinear and can be solved by numerical techniques. The character of the luminance waves $B(t)$ is related to the time variation of the active current density $j(t)$ in the luminophor layer. The function $j(t)$ was determined by mathematical modeling of electric characteristics of the electroluminescent devices studied. The modeling was based on a system of equations describing an equivalent nonlinear scheme of a TFEL device in terms of the main laws of the electric circuit theory [1]. In order to check for the adequacy of the model, the function $j(t)$ was also determined experimentally as a time derivative of the charge accumulated at the luminophor–insulator interface of a thin-film structure.

The solution to equation (4) was obtained by the fourth-order Runge–Kutta method. The initial conditions were taken in the form $t_0 = 0$ s, $B_0 = B(t_0) = 0$ kd/m^2. The calculation was performed for the following values of parameters [2]: $N = (1–2) \times 10^{18}$ cm^{-3}; $\sigma = 2 \times 10^{-16}$ cm^2; $\tau = 1.3$ ms; $K_\lambda = 520$ lm/W; $h\nu = 2.1$ eV; $\eta_s = 0.09$; $d_{ph} = 0.5–2$ μm. The time variation of luminance for the TFEL structures excited by ac voltages of various shapes at a frequency of 1 kHz and an amplitude of 200 V is presented in the figure.

The experimental investigations were performed using structures based on the ZnS:Mn films with ZrO_2–Y_2O_3 insulating layers. The structures were obtained by electron-beam deposition onto glass substrates with transparent electrode (ITO). The experimental and calculated voltage–luminance characteristics showed good coincidence and agreed with the published data [5].

The results allowed us to make the following conclusion of considerable practical importance for the creation of TFEL based display devices. An analysis of our previous results obtained by mathematical modeling and experimental measurements, as well as the published data of other researchers, suggested that the duration of transient electric processes occurring in thin-film structures amounts to 1–3 periods of the applied ac voltage. At the same time, study of the lighting characteristics (luminance waves) in this work showed that the duration of transient processes determined from the time variation of luminance of thin-film electroluminescent devices may reach up to ten periods of the ac voltage. Thus, for the average (effective) luminance of emission from a TFEL element excited by a periodic alternating-sign voltage, the value determined by the Talbot law for one or even a few periods is markedly lower than the level of luminance obtained from this element with the same voltage applied for a time corresponding to a greater number of periods.

From the standpoint of development of the schemes controlling the operation of TFEL systems involving large numbers of elements, the above results imply that high luminance levels can be reached only by applying the trains of ac pulses sufficiently long to ensure attaining of the regime of steady-state operation of the emitting elements. This principle was realized in an original device controlling the formation of images on a luminescent matrix display composed of two-directional semiconductor elements with negative differential resistance.

ACKNOWLEDGMENTS

The work was performed within the framework of the “Integration” Federal Research Program, project A0065.

REFERENCES

1. E. E. Zabudskiĭ and M. K. Samokhvalov, Mikroélektronika **28** (2), 117 (1999).
2. M. K. Samokhvalov, Zh. Tekh. Fiz. **66** (10), 139 (1996).
3. J. W. Allen, J. Lumin. **23** (1–2), 127 (1981).
4. M. K. Samokhvalov, Zh. Prikl. Spektrosk. **62** (3), 182 (1995).
5. G. O. Muller and R. Mach, J. Lumin. **40–41**, 92 (1988).

Translated by P.P. Pozdeev

Technical Physics Letters, Vol. 26, No. 1, 2000, pp. 31–32. Translated from Pis'ma v Zhurnal Tekhnicheskoĭ Fiziki, Vol. 26, No. 1, 2000, pp. 61–65.

Formation of Charged Particle Tracks in Glass-Fiber Microstructures

V. V. Ammosov[1)], E. M. Gushchin[2)], P. Ioannu[3)], S. V. Somov[1)], and A. A. Semak[2)]

[1)]*Institute of High Energy Physics, Protvino, Moscow oblast, Russia*

[2)]*Moscow Institute of Engineering Physics (Technical University), Moscow, Russia*

[3)]*Institute of Athens, Athens, Greece*

Received September 13, 1999

Abstract—Glass-fiber disks intended for the image transfer in electrooptical transducers can be used as targets in microchannel Cerenkov track detectors. Calculated values of the coefficient of Cerenkov radiation trapping in the glass-fiber discs well agree with experiment, which confirms the hypothesis concerning a Cerenkov-type mechanism of the charged particle track formation in non-scintillating microfiber structures. © *2000 MAIK "Nauka/Interperiodica".*

Glass-fiber disks are used in electrooptical transducers (EOTs)—the main elements of microchannel track detectors (MCDs). An MCD structure typically comprises a three-stage EOT array operated in the regime of single photoelectron detection. A target mounted at the entrance of the first EOT stage represents either a microcapillary unit filled with a liquid scintillator or a an assembly of thin scintillating plastic or glass fibers (see, e.g., [1]). A part of the generated light flux (typically 4–6%) is trapped by the capillary (or fiber), transported by means of the total internal reflectance effect toward a photocathode, amplified, and detected by a TV camera (vidicon). Then the image is converted into a digital form and recorded into computer memory for processing and storage. The main disadvantage of the scintillating MCDs is a poor optical insulation of the capillaries (fibers), which leads to spreading of the light pulse and decrease in the spatial resolution of the detector. This effect is especially manifested in the study of interactions accompanied by the ejection of particles with a high ionization density. High energy deposition in the vicinity of the interaction peak results in flaring of this region, which hinders analysis of the signal.

Recently we have studied scintillating MCDs and noted that tracks of rapid charged particles were observed even in the absence of a scintillating target, when the particles passed via the entrance disk at the first EOT stage [2, 3]. Moreover, the density of dots on the particle tracks $n = 2$–3 mm^{-1} registered in this mode has unexpectedly proved to be comparable with the level obtained with a scintillating target. A similar effect was observed when a scintillating target was replaced by non-scintillating glass-fiber disks intended for the image transfer. The results of our measurements showed that the light yield coefficient of the glass employed in the core of the latter glass-fiber disks does not exceed 0.01% of the analogous value for a plastic scintillator, and it was suggested that the tracks registered in this mode are formed by the Cerenkov radiation. Indeed, despite the Cerenkov radiation intensity being low compared to that of the scintillations, the directed character of the former radiation results in that the coefficient of its trapping in the glass-fiber disk may reach up to about unity which markedly exceeds the coefficient of trapping of the isotropic radiation.

Since the radiation trapping coefficient and, hence, the track density for the Cerenkov radiation must depend on the angle θ between the fiber axis and a particle trajectory, we have performed preliminary calculation of this dependence for the following values of a real glass-fiber disks: the fiber core diameter $d = 5$ μm; the fiber core index of refraction $n_1 = 1.812$; the fiber shell index of refraction $n_2 = 1.49$. The radiation trapping coefficient k for each fixed value of θ was calculated by averaging over all possible distances R between the fiber axis and the particle trajectory ($0 \le R \le d/2$). It was assumed that particles move toward the cathode for $0° \le \theta < 90°$ and away from the cathode for $90° < \theta < 180°$. As seen from Fig. 1, the k versus θ plot exhibits a maximum at $\theta = 30°$–$50°$ and lies above the abscissa axis ($k > 0$) at all angles up to $\theta = 147°$.

In practice, a value of importance is the dot number density n on the particle track rather than the radiation trapping coefficient proper. Since a detector registers the projection of a particle track onto the photocathode plane, rather than the real track, we obtain $n \sim k/\sin\theta$. This implies that the dot number density as a function of the angle θ (see Fig. 2) would have a character somewhat different from that of the $k(\theta)$ function. In calculating the dot number density on the track projection, we took into account the spectral composition of the Cerenkov radiation and a spectral characteristic of the quantum yield of a bialkali-metal-oxide photocathode used in the first EOT stage. Then, we studied an MCD

1063-7850/00/2601-0031$20.00 © 2000 MAIK "Nauka/Interperiodica"

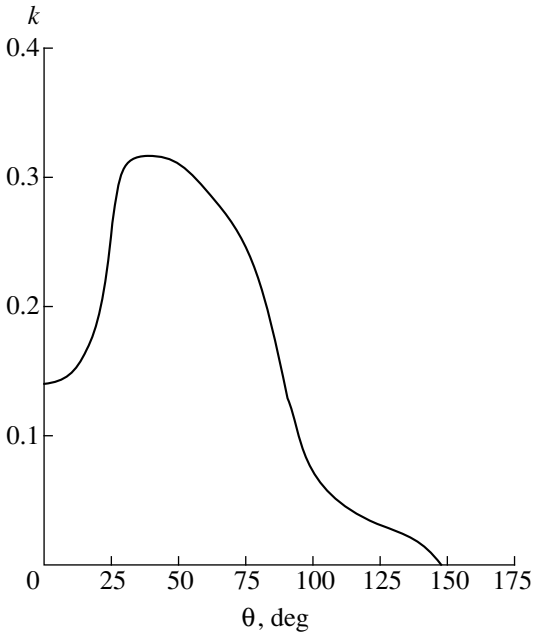

Fig. 1. Plot of the Cerenkov radiation trapping coefficient of a glass microfiber versus the angle between the fiber axis and a charged particle trajectory.

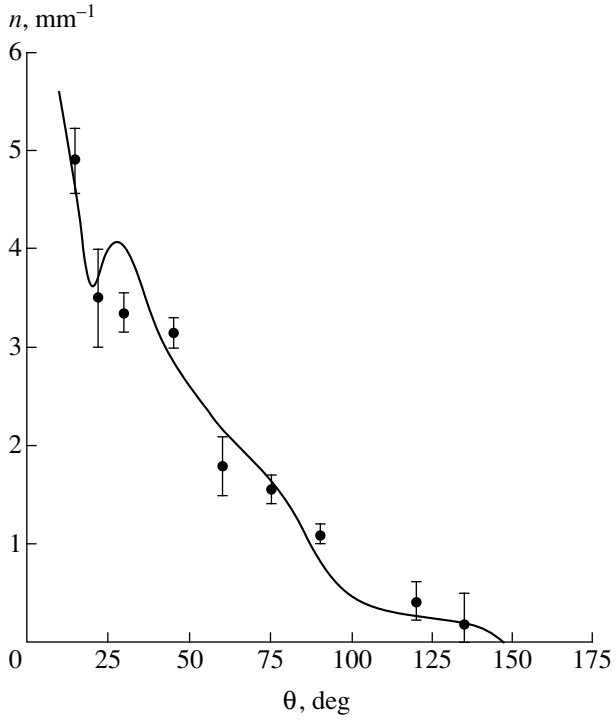

Fig. 2. Plot of the dot number density on a charged particle trajectory registered in the entrance glass-fiber disk of MCD versus the angle between the fiber axis and a charged particle trajectory. Solid curve shows the results of calculation based on the data presented in Fig. 1; black symbols with error bars present the experimental data obtained in a proton beam.

during operation in a 70-GeV proton beam at various angles relative to the beam axis. It was established that the measured dot number density on the proton tracks registered on the entrance disk of the first EOT stage agrees well with the results of preliminary calculations (Fig. 2). As seen, the best conditions of exposure of a Cerenkov MCD are provided by orientation at an angle of 25°–45° relative to the particle beam axis. On increasing the angle above this interval, the dot number density on the track exhibits a sharp drop, while the measurements at angles below the interval are difficult because of a short length of the track projection onto the photocathode plane. Further analysis of the interactions registered with this detector showed that the optimum angle is $\theta \approx 40°–45°$.

Thus, the results of our calculations and measurements conformed the assumption that the tracks of charged particles in glass-fiber structures are formed due to the Cerenkov radiation. This fact opens the possibility of creating a track detector of the new type, the Cerenkov MCD, possessing a spatial resolution of 10–100 μm. This device is insensitive to strongly ionizing particles. Other important advantages of the Cerenkov MCD based on the standard glass-fiber disks (of the type intended for the image transfer) is a good optical insulation of the fiber core due to the presence of the third nontransparent shell and the absence of principal restrictions on the detector size. The latter circumstance allows the new detectors to be effectively used in investigations involving the neutrino beams.

ACKNOWLEDGMENTS

This work was supported by the Russian Foundation for Basic Research (project no. 98-02-17139), by the Ministry of Education of the Russian Federation (a grant according to the 1998 Research Program, Section “Nuclear Physics and High-Energy Physics”), and by the “Interphysics” State Research Center.

REFERENCES

1. *Proceedings of the 3rd Conf. on Scintillation Fiber Detectors*, Ed. by A. D. Bross, R. C. Ruchti, and M. R. Wayne (Woodbury, 1998).
2. E. M. Gushchin, S. V. Somov, and V. A. Ryabov, Pis’ma Zh. Tekh. Fiz. **21** (17), 42 (1995).
3. E. M. Gushchin, S. V. Somov, and V. A. Ryabov, Prib. Tekh. Éksp., No. 4, 15 (1996).

Translated by P.P. Pozdeev

Technical Physics Letters, Vol. 26, No. 1, 2000, pp. 33–34. Translated from Pis'ma v Zhurnal Tekhnicheskoĭ Fiziki, Vol. 26, No. 1, 2000, pp. 66–70.

Numerical Simulation of the Dynamics of a Liquid Conducting Surface in a Strong Electric Field

V. G. Suvorov

Institute of Electrophysics, Ural Division, Russian Academy of Sciences, Yekaterinburg, Russia

Received May 12, 1999; in final form, September 13, 1999

Abstract—Two-dimensional numerical simulation is performed on the instability of a liquid conducting surface with axial symmetry in a strong electric field. The method of splitting with respect to physical factors with transformation of the calculation region to the canonical form [1] is used to investigate the flow of liquid with a free surface. This approach enables one to study the time dependence of the basic physical quantities in the nonlinear mode when the emitting point is formed. It is demonstrated that this dependence exhibits a collapse behavior: a critical time t_c exists, in the vicinity of which a physical quantity either diverges or goes to zero as $\sim(t_c - t)^\gamma$. The values of the critical exponent γ are found for the electric field, curvature radius, and the axial velocity at the point tip, and the correlation between them demonstrated. © *2000 MAIK "Nauka/Interperiodica".*

The study of phenomena associated with the motion of conducting liquid in electric field (operation of ion sources, explosive electron emission, functioning of the cathode spot of vacuum arc) requires models describing the regularities of development of the nonlinear stage of the process. Numerical simulation could considerably promote the study of these regularities. A specific feature of this problem is the presence of strong feedback between the surface shape and the electric field on this surface, which calls for a fairly exact definition of the surface, especially, at the moment when the emitting point is formed. The traditional method of markers on the net (MN), employed previously to solve such problems [2], inadequately accurately simulates the flow in the vicinity of free surface, as a result of which the surface shape is not smooth, and its rapid randomization occurs because of the above-mentioned feedback. Zheng and Linsu [2] traced the evolution of surface in electric field; however, no investigation was made of the time dependence of physical quantities; in so doing, the randomization problem was overcome by artificial smoothing out of the surface.

In this paper, I present the results of numerical simulation of a liquid conducting surface in electric field using the method suggested by Belotserkovskiĭ *et al.* [1]; the simulation was performed in axisymmetric geometry. The difference between this method and the MN method lies in the transformation of the calculation region to the canonical form. Using the change of variables

$$r = r, \quad \xi(r, t) = \frac{z + B}{\eta(r, t) + B}$$

the contour bounding the calculation region ($r = 0$, axis of symmetry of the problem; $r = x_r$, right-hand boundary; $z = \eta(r, t)$, free surface; $z = -B$, bottom) is, at every moment of time, mapped onto a rectangle ($r = 0$, $r = x_r$, $\xi = 0$, $\xi = 1$) in the (r, ξ) system. The set of Navier–Stokes equations is written in the (r, ξ) variables and solved by the standard methods on a distributed net [3].

I traced the evolution of small disturbance of the liquid surface of mercury in a uniform electric field with an intensity somewhat exceeding the critical value, in cylindrical coordinates (Fig. 1). In so doing, the right-hand edge and bottom shifted to a fairly long distance and did not affect the calculation results. The electric field on the surface was also determined by the method of [1]; the surface curvature and the pressure of surface tension were determined directly by means of finite-difference approximation, and no artificial smoothing out was introduced. The last surface in Fig. 1 is substantially a typical autoelectronic (or ionic) emitter.

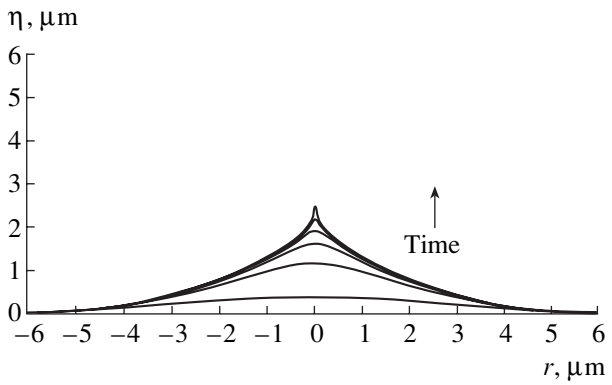

Fig. 1. The evolution of the liquid surface of mercury in a uniform external field, $E_0 = 2.4 \times 10^8$ V/m. The surfaces are given successively at the moments of time (in ns); 0, 695, 783, 810, 822, 826; $t_c = 829$.

1063-7850/00/2601-0033$20.00 © 2000 MAIK "Nauka/Interperiodica"

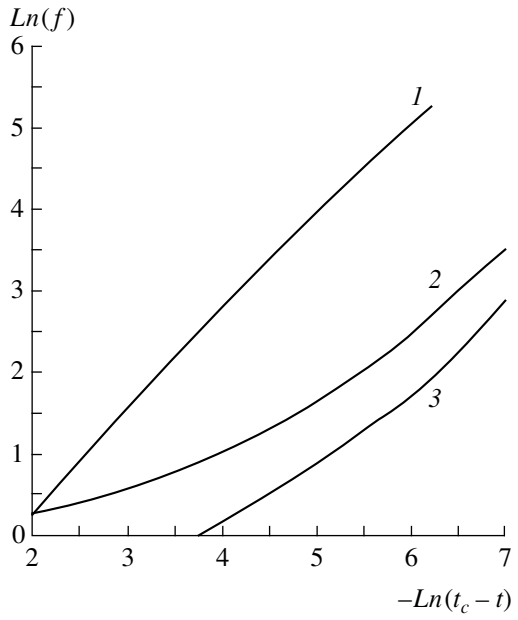

Fig. 2. The time dependence of f: (*1*) $f = R_c^{-1}$, (*2*) $f = E$, (*3*) $f = \nu$, for the surface evolution given in Fig. 1.

The calculation results indicate that one can fairly clearly identify in the liquid surface dynamics the nonlinear phase in which the variation of physical quantities exhibits a collapse behavior, i.e., a development during which the quantities in a finite time (t_c) go either to zero or to infinity. The dependences of $Ln\{R_c^{-1}(t), E(t), \nu(t)\}$ on $-Ln(t_c - t)$ have the form of straight lines at $t \longrightarrow t_c$ (Fig. 2). Here, $R_c^{-1}(t)$, $E(t)$, and $\nu(t)$ respectively denote the dimensionless curvature, electric field, and axial velocity at the point tip. Note that no appreciable indeterminacy exists in the choice of t_c. Therefore, one can write the following relations for dimensional quantities:

$$E(t) = E_0\left(1 - \frac{t - t_0}{t_c - t_0}\right)^{-\gamma_E}, \quad (1)$$

$$R_c(t) = R_0\left(1 - \frac{t - t_0}{t_c - t_0}\right)^{\gamma_R}, \quad (2)$$

$$\nu(t) = \nu_0\left(1 - \frac{t - t_0}{t_c - t_0}\right)^{-\gamma_V}, \quad (3)$$

where t_0 is the time characterizing the beginning of the nonlinear stage; and E_0, R_0, and ν_0 are physical quantities at the moment of time $t = t_0$. The following exponents were derived in (1)–(3): $\gamma_E = 1.01$, $\gamma_R = 1.05$, and $\gamma_V = 1.1$. The close coincidence of the values of γ_E and γ_R is a consequence of the well-known law according to which the electric field on an autoemission cathode is $\sim R_c^{-1}$. The value of γ_V may be explained by simple estimates. Indeed, the momentum transferred by the liquid in the vicinity of the point is $\sim\rho\lambda R_c^2\nu$ (ρ is the liquid density and λ is the scale of disturbance), and the force acting on it is $\sim R_c^2 E^2$; then, Newton's second law yields $\gamma_V + 1 \approx 2\gamma_E$. One can see that the derived exponents satisfy this equality fairly well.

Needless to say that by using the numerical approach, one cannot rigorously prove relations (1)–(3); however, in trying to approximate the time dependences of physical quantities, I have arrived at the conclusion that these relations are the best. In this case, the analytic approach is more rigorous, for example, on the lines of [4]; as to relations (1)–(3), they could serve some reference point for nonlinear analysis.

ACKNOWLEDGMENTS

In conclusion, I would like to thank Prof. Forbes for the possibility of using the results of investigations performed at the University of Surrey, Guildford, UK.

This study received support from the Russian Foundation for Basic Research, project nos. 99-02-16462 and 99-02-18234, as well as from the International Foundation INTAS-RFFI (Russian Foundation for Basic Research), project no. IR-97-663.

REFERENCES

1. O. M. Belotserkovskiĭ, V. A. Gushchin, and V. N. Kon'shchin, Zh. Vychisl. Mat. Mat. Fiz. **27**, 594 (1987).
2. C. Zheng and T. Linsu, J. Vac. Sci. Technol. B **6** (6), 2104 (1988).
3. C. A. J. Fletcher, *Computational Methods in Fluid Dynamics* (Mir, Moscow, 1991).
4. E. A. Kuznetsov, M. D. Spector, and V. E. Zakharov, Phys. Rev. E **49**, 1283 (1994).

Translated by H. Bronsteĭn

Technical Physics Letters, Vol. 26, No. 1, 2000, pp. 35–37. Translated from Pis'ma v Zhurnal Tekhnicheskoĭ Fiziki, Vol. 26, No. 1, 2000, pp. 71–76.

The Physicomechanical Properties and Structure of Superelastic Porous Titanium Nickelide-Based Alloys

V. É. Gyunter, Yu. F. Yasenchuk, A. A. Klopotov, and V. N. Khodorenko

Research Institute of Medical Materials and Implants with Plastic Memory at Kuznetsov Siberian Physicomechanical Institute, Tomsk, Russia

Received July 23, 1999

Abstract—The results are given investigations of the structural and physicomechanical properties in porous titanium nickelide, and these results are compared with analogous properties in cast alloys. © *2000 MAIK "Nauka/Interperiodica".*

In recent years, new materials used as continuously functioning implants in the human organism, such as porous permeable titanium nickelide-based alloys, have found extensive application in medicine [1]. The alloys exhibit high elastic properties, are capable of changing their shape with temperature, and do not deteriorate under conditions of sign-variable load. The complex behavior of martensite phase transformations occurring in titanium nickelide-based alloys shows up clearly in porous structures. Phase transitions in porous titanium nickelide-based alloys are characterized by hysteresis and extended temperature interval in which the material exhibits the effects of plastic memory of shape and superelasticity.

The investigation results given in this paper establish the correlation between the physicomechanical properties and structural transformations in porous alloys and their difference from those in nonporous titanium nickelide-based alloys. The inclusion of the singularities of the behavior of porous titanium nickelide-based alloys makes for their more efficient utilization in practical medicine [1].

X-ray diffraction studies were performed in a DRON-3 diffractometer using low- and high-temperature chambers KRN-190 and GPVT-1500, respectively. Pictures were taken in CuK_α radiation. A Tesla-BS-540 electron microscope was used for electron-microscopic investigations. The curves of the temperature dependence of electrical resistance were determined by the standard four-point potentiometer technique [2]. Plastic deformation was accomplished by tension. The alloys were prepared by the process described in [1]. Charge materials were provided by Grade PNK1 VL7 nickel powder and Grade PTÉM-1 titanium powder. The material under investigation had a porosity of approximately 40–45%.

The X-ray diffraction studies of porous titanium nickelide-based alloys (whose composition was close to stoichiometric), performed at different temperatures, revealed the presence of several phases, namely, *B*2, *B*19, and Ti_2Ni (Fig. 1). The content of the Ti_2Ni phase is approximately 5–8% for all temperatures. The electron microscopy of massive regions of porous alloys reveals numerous large spherical formations of Ti_2Ni with an average size of ~300 nm and finely divided particles (~20 nm). In the bridges dividing the pores, acicular crystals of martensite of phase *B*19' are observed, while almost no particles of the Ti_xNi_y phase are present. Figure 1d gives fragments of X-ray photographs of porous titanium nickelide at different temperatures, which demonstrate clearly the presence of the high-temperature *B*2 phase at low temperatures and a wide temperature range of existence of a two-phase mixture of *B*2 + *B*19'. The presence of a wide temperature range of martensite transformation in porous titanium nickelide compared with cast alloy is reflected in the temperature curves of electrical resistance (Fig. 2a). Based on the data of X-ray analysis, the variation of the phase composition in porous and cast alloys was studied and the variation of the volume fraction of phase *B*19' calculated (Fig. 2b). It is demonstrated that the martensite transition (MT) $B2 \longrightarrow B19'$ is incomplete in porous alloys (only about 60% of the *B*2 phase goes to the martensite phase) and proceeds in a wider temperature interval than in the case of cast alloys.

Therefore, an important singularity of porous titanium nickelide compared to nonporous (cast) alloy of the same composition consists in a wide temperature interval of phase transformations (Fig. 2). It is approximately 250°C, i.e., it exceeds considerably the range (30–40°C) of transformations of cast alloy. The increase of the temperature range of phase transformations is caused by the structure of porous titanium nickelide prepared from powders. The characteristic transformation temperature titanium nickelide is sensitive to the chemical composition. The variation of the content of components in the homogeneity region leads to a shift of the temperature of the beginning of phase transformations by several tens of degrees [1]. The phase formations arising in the alloy (for example, Ti_2Ni,

1063-7850/00/2601-0035$20.00 © 2000 MAIK "Nauka/Interperiodica"

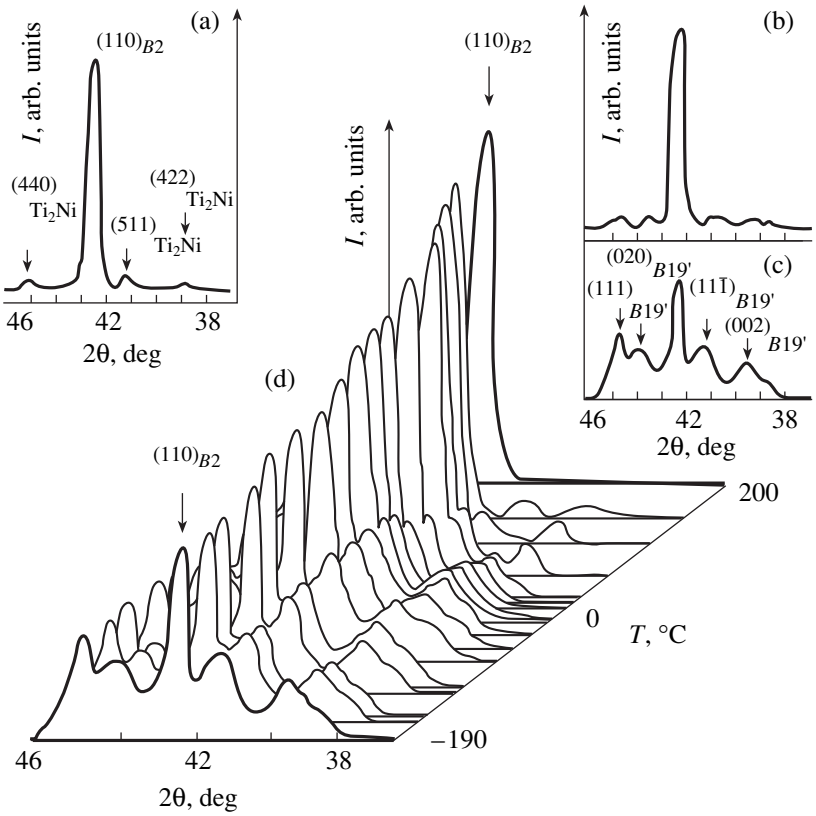

Fig. 1. Fragments of X-ray photographs of porous TiNi at different temperatures: (a) $T = 200°C$, (b) $T = 0°C$, (c) $T = -190°C$.

$TiNi_3$, Ti_4Ni_2O(N, H, C)) develop an elevated level of voltage in martensite crystals and in the matrix phase *B*2, including the bridges dividing the pores, and lead to a shift of the characteristic temperatures of martensite transformations and of the temperatures at which the plastic memory effects show up [1]. The dimensional factor is also of importance, because the manifestation of martensite transformation in thin bridges differs from that in massive regions. The effect of these factors results in that phase transformations in titanium nickelide-based porous materials begin in different regions at different temperatures, with the hysteresis being extended along the temperature axis, while the temperature ranges of transformations and the ranges of manifestations of the effects of plastic memory and superelasticity in porous titanium nickelide-based alloys are extended accordingly.

Figure 2c illustrates the effect of plastic memory in porous and cast alloys. In the porous alloy, the plastic memory effect shows up in a wider temperature range than in the cast one, and the residual plastic deformation in the porous material is much greater in magnitude (ε in Fig. 2c) than in the case of the cast one. An almost complete (up to 100%) recovery of shape is observed in cast titanium nickelide after deformation by 6–8% and subsequent heating above the temperature range of MT (Fig. 2c). When the degree of deformation of cast titanium nickelide increases, dislocation defects are formed which are irreversible as distinct from martensite transformations. The stage of reversible deformation by the martensite mechanism is replaced by that of irreversible plastic deformation. Even at small loads, regions emerge, in which the elastic deformation exceeds the limiting value. On the contrary, in porous alloys, the degree of recovery of shape does not exceed 85% even for minimum deformation. The degree of recovery of shape depends on the porosity, size distribution of pores, and level of stresses of martensite shift, i.e., is associated with the singularities of deformation of porous bodies.

An analysis of the deformation dependences of titanium nickelide of different porosities reveals that the yield point of the alloy decreases as the porosity increases. In the σ–ε diagrams, the curves of loading and subsequent release do not coincide and form a hysteresis loop (Fig. 3) whose width is defined by the magnitude of dissipation of energy. The hysteresis increases with porosity. In so doing, the reversible deformation may amount to over 7%, which exceeds appreciably the elastic Hookean deformation. As compared with cast titanium nickelide, an extension is observed of the temperature range of manifestation of the elastic properties of porous samples (Fig. 3). The process of destruction of pore walls is nonuniform, this leading to an extension of the range of manifestation of the elastic properties of porous materials of titanium nickelide and alloys

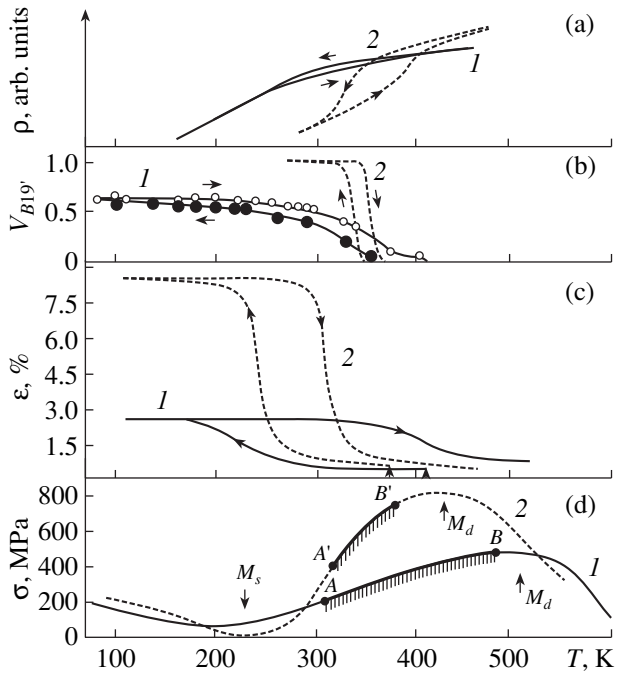

Fig. 2. The temperature dependences of various characteristics in (*1*) porous and (*2*) cast titanium nickelide-based alloys: (a) curves of electrical resistance, (b) curves of the volume fraction of phase *B*19′, (c) curves of reversible memory effect, (d) curve of the dependence of the yield point (segments *AB* indicate the temperature ranges of superelasticity).

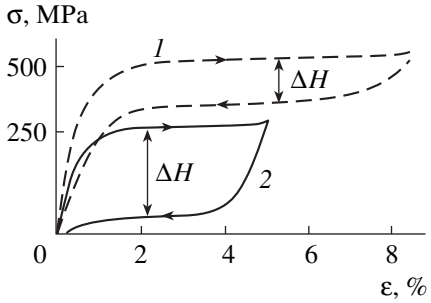

Fig. 3. The deformation dependence of manifestation of superelastic properties in (*1*) cast and (*2*) porous titanium nickelide-based alloys (Δ*H* is the hysteresis width).

on its basis. Note that the complex behavior of the deformation processes in porous titanium nickelide-based alloys and the complex behavior of martensite transformations in those alloys extends both the temperature ranges of superelasticity (Fig. 2) and the ranges of manifestation of plastic memory effects.

More important from the standpoint of practical uses of titanium nickelide-based alloys are both the characteristic temperatures of martensite transformations and the parameters of the effects of plastic memory and superelasticity. Figure 2d gives the temperature dependence of critical stresses of martensite shift and of the yield point of porous and cast alloys. The characteristics such as the minimum stress of martensite shift ($\sigma_{\min}^{M_S}$), maximum stress of martensite shift corresponding to the yield point at the temperature M_d ($\sigma_{\max}^{M_d}$), and the temperature range of manifestation of superelasticity $\Delta T = T_B - T_A$ (the difference between the maximum T_B and minimum T_A temperatures at which the superelastic properties show up) are given in Fig. 2d for porous and cast alloys. The martensite shift in the porous material is much less than in the cast one; however, the temperature range of manifestation of superelasticity in the porous material is much wider than in the cast one.

Under real conditions, the substantial shift of the range of transformations in both cast and porous alloys to the low-temperature region (Fig. 3, curve *1*) is caused by significant plastic deformation.

The experimental results lead one to draw an important conclusion. The superelastic properties, the plastic memory effects, and the thermal-force singularities show up in porous titanium nickelide-based alloys in a wider temperature range than in cast alloys of analogous composition.

REFERENCES

1. V. É. Gyunter, G. Ts. Dombaev, P. G. Sysolyatin, *et al.*, *Medical Materials and Implants with Plastic Memory* (TGU—Tomsk State University, Tomsk, 1998).
2. W. Hume-Rothery, J. W. Christian, and W. B. Pearson, *Equilibrium Diagrams of Metal Systems* (Metallurgizdat, Moscow, 1956).

Translated by H. Bronsteĭn

Technical Physics Letters, Vol. 26, No. 1, 2000, pp. 38–40. Translated from Pis'ma v Zhurnal Tekhnicheskoĭ Fiziki, Vol. 26, No. 1, 2000, pp. 77–83.

Scattering of Plane Electromagnetic Waves by a Chiral–Metal Cylinder

V. A. Neganov and O. V. Osipov

Povolzh'e State Academy of Telecommunications and Information Science, Samara, Russia

Received January 29, 1999

Abstract—The problem of scattering of *E*- and *H*-polarized plane electromagnetic waves by a metal cylinder covered with a chiral layer is solved by the method of partial regions. The scattering field is studied in the near and far zones. The correlation between the type of polarization of the incident electromagnetic wave and the magnitude of the depolarized component of the scattered field is considered. © *2000 MAIK "Nauka/Interperiodica".*

Recently, particular interest has been attracted to the interaction of electromagnetic radiation of the microwave and extremely-high-frequency ranges with the so-called chiral media. The phenomenon of chirality is related to the violation of the mirror symmetry of the particles forming a medium [1]. A chiral medium usually consists of a single type of elements that are uniformly distributed throughout an isotropic medium and chaotically oriented [2]. The constitutive relations for such media relate the electric and magnetic field strengths to the electric **D** and magnetic **B** inductions. The interaction of an electromagnetic wave with a chiral medium is accompanied by a number of specific effects. First, in such a medium, the propagation of two waves with the clockwise and anticlockwise polarizations and different propagation constants is observed [2, 3]. Second, the reflection of an electromagnetic wave from a chiral medium leads to the appearance of the so-called depolarized component (the reflected wave contains components that are absent in the incident wave). This effect is observed at any polarization of the incident wave. The formation of such a depolarized field is a consequence of the fact that, for example, in the case of an *E*-polarized incident wave, the normal electric component excites both electric and magnetic dipole moments in the medium.

Below, we present the solution of the problem of the plane electromagnetic wave scattering by a chiral circular cylinder with a thin metal (infinite-conductance) rod positioned inside it along its geometric axis. The problem is solved by the method of partial regions. The scattering of plane electromagnetic waves by a homogeneous chiral cylinder is considered as a limiting case [4, 5]. For a chiral medium, the constitutive relations represented in one of the forms (with the time dependence $e^{i\omega t}$) are as follows:

$$\mathbf{D} = \varepsilon_c \mathbf{E} - i\xi\mu\mathbf{H}, \quad \mathbf{B} = \mu\mathbf{H} + i\xi\mu\mathbf{E}, \tag{1}$$

where $\varepsilon_c = \varepsilon + \mu\xi^2$ is the chiral permittivity, ε and μ are the dielectric permittivity and the magnetic permeability, and ξ is the chirality parameter (the case $\xi = 0$ corresponds to an ordinary dielectric medium). We note that, besides expressions (1), there exist other representations of constitutive relations for a chiral medium (see, e.g., [6, 7]).

The Maxwell equations for the field in a chiral medium can be written in the form

$$\begin{aligned} \nabla \times \mathbf{H} &= k(\varepsilon_c \mathbf{E} + \xi\mu\mathbf{H}), \\ \nabla \times \mathbf{E} &= k(\mu\mathbf{H} + \xi\mu\mathbf{E}), \end{aligned} \tag{2}$$

where k is the wave number for free space, **H** is normalized to $i\eta_0^{-1}$, and $\eta_0 = \sqrt{\mu_0/\varepsilon_0}$ is the wave resistance for vacuum.

We consider the incidence of a plane electromagnetic wave of a given polarization on an isotropic chiral cylinder of radius R with a thin conducting rod of radius R_0 inside it; the cylinder is infinite along the z-axis, and the rod axis is coincident with the geometric cylinder axis (Fig. 1a). Assuming that the field does not vary along the 0z-axis ($\partial/\partial z = 0$), we set the field of the incident wave of unit amplitude in the form

$$\begin{aligned} \mathbf{E}'(r, \varphi) &= \mathbf{z}_0 e^{-ikr\cos\varphi}, \\ \mathbf{H}'(r, \varphi) &= -\varphi_0 \cos\varphi e^{-ikr\cos\varphi} + \mathbf{r}_0 \sin\varphi e^{-ikr\cos\varphi} \end{aligned} \tag{3a}$$

for the case of an *E*-polarized incident wave and

$$\begin{aligned} \mathbf{H}'(r, \varphi) &= \mathbf{z}_0 e^{-ikr\cos\varphi}, \\ \mathbf{E}'(r, \varphi) &= -i\varphi_0 \cos\varphi e^{-ikr\cos\varphi} + i\mathbf{r}_0 \sin\varphi e^{-ikr\cos\varphi} \end{aligned} \tag{3b}$$

for the case of an *H*-polarized incident wave, where $\mathbf{r}_0$, $\boldsymbol{\varphi}_0$, and $\mathbf{z}_0$ are the unit vectors of the cylindrical coordinate system.

1063-7850/00/2601-0038$20.00 © 2000 MAIK "Nauka/Interperiodica"

It is well known that the wave propagation in a chiral medium obeys two coupled differential equations [3]:

$$\{\Delta + k_c^2\}E_z - (\xi\mu/\varepsilon_c)\{\Delta - k_c^2\}H_z = 0,$$
$$\{\Delta + k_c^2\}H_z - \xi\{\Delta - k_c^2\}E_z = 0, \quad (4)$$

where $k_c^2 = k^2\varepsilon\mu$ and Δ is a Laplacian with respect to the variables r and φ.

The system of equations (4) can be solved by applying the substitution [4]:

$$E_z = E_R + E_L, \quad H_z = \sqrt{\varepsilon_c/\mu}(E_R - E_L).$$

Then, using equations (4) for the electromagnetic field components represented in the form of Fourier series expansions in the coordinate φ, we obtain the following expressions ($R_0 < r < R$):

$$E_z = \sum_{n=-\infty}^{+\infty} (A_n^R J_n(k_R r) + B_n^R Y_n(k_R r) + A_n^L J_n(k_L r) + B_n^L Y_n(k_L r))e^{in\varphi},$$

$$H_z = \sqrt{\varepsilon_c/\mu} \sum_{n=-\infty}^{+\infty} (A_n^R J_n(k_R r) + B_n^R Y_n(k_R r) - A_n^L J_n(k_L r) - B_n^L Y_n(k_L r))e^{in\varphi},$$

$$H_\varphi = -\frac{1}{k\varepsilon\mu}\left\{\varepsilon_c \frac{dE_z}{dr} - \xi\mu\frac{dH_z}{dr}\right\},$$

$$E_\varphi = -\frac{1}{k\varepsilon}\left\{\frac{dH_z}{dr} - \xi\frac{dE_z}{dr}\right\}, \quad (5)$$

where $J_n(\chi)$ is a Bessel function; $Y_n(\chi)$ is a Neumann function; and A_n^R, A_n^L, B_n^R, and B_n^L are some unknown coefficients.

For the case of a homogeneous chiral cylinder (Fig. 1b), in expressions (5) we have to set $B_n^R = B_n^L = 0$ ($\forall n$).

Expressions (5) testify to the fact that, at any polarization of the incident wave, both E_z and H_z components occur in the chiral medium.

For the wave reflected from a chiral cylinder, other equations are valid ($r > R$):

$$(\Delta + k^2)\begin{Bmatrix} E_z'' \\ H_z'' \end{Bmatrix} = 0. \quad (6)$$

These equations allow for the fact that a depolarization of the electromagnetic field occurs in the outer region, and both normal components, E_z and H_z, are always present. Thus, in the outer region ($r > R$), we can represent the solution to equations (6) in the form

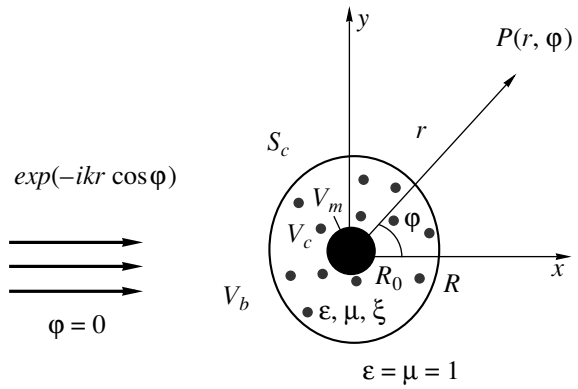

Fig. 1. Geometry of the problem: a metal rod covered by a chiral layer.

$$E_z'' = \sum_{n=-\infty}^{+\infty} C_n H_n^{(2)}(kr)e^{in\varphi},$$
$$H_z'' = \sum_{n=-\infty}^{+\infty} D_n H_n^{(2)}(kr)e^{in\varphi},$$
$$H_\varphi'' = -\sum_{n=-\infty}^{+\infty} C_n H_n^{(2)'}(kr)e^{in\varphi},$$
$$E_\varphi'' = -\sum_{n=-\infty}^{+\infty} D_n H_n^{(2)'}(kr)e^{in\varphi}, \quad (7)$$

where $H_n^{(2)}(\nu)$ is a Hankel function of the second kind and $H_n^{(2)'}(\nu)$ is its derivative with respect to the entire argument ν.

Using the boundary conditions at $r = R_0$

$$E_z = 0, \quad E_\varphi = 0 \quad (8a)$$

and at $r = R$

$$E_z = E_z' + E_z'', \quad H_z = H_z' + H_z'',$$
$$E_\varphi = E_\varphi' + E_\varphi'', \quad H_\varphi = H_\varphi' + H_\varphi'', \quad (8b)$$

we can easily obtain a system of six algebraic equations for the determination of the coefficients $A_n^{R,L}$, $B_n^{R,L}$, C_n, and D_n. Here, it is necessary to substitute expressions (3a) or (3b) for the incident field, depending on the type of its polarization. For the case of a homogeneous chiral cylinder (without a metal rod), the expressions for the aforementioned coefficients can be written in an explicit form ($B_n^R = B_n^L = 0$).

From formulas (7), we can derive the expressions for the reflected field in the far zone ($kr \longrightarrow \infty$) by

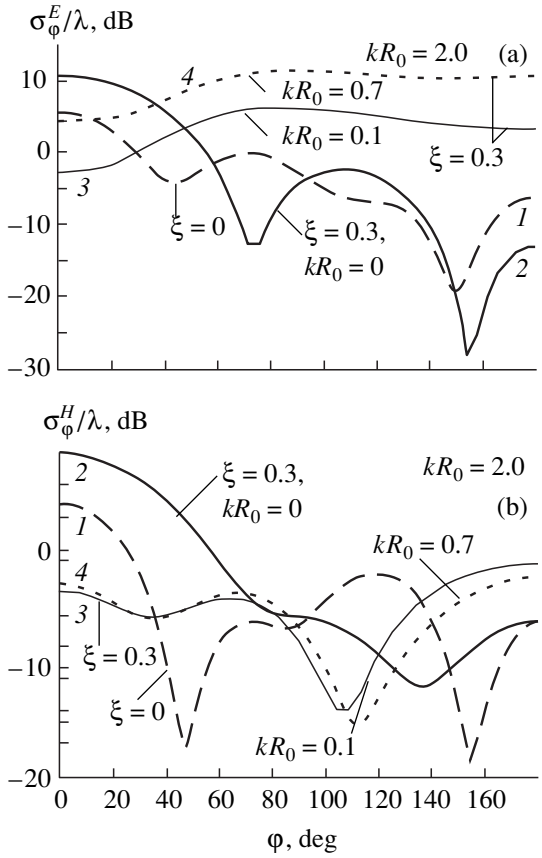

Fig. 2. Dependences of the scattering field cross-section on the angle of the wave incidence for (a) an *E*-polarized incident wave and (b) an *H*-polarized incident wave: (*1*) a homogeneous dielectric cylinder with losses; (*2*) a homogeneous chiral cylinder; (*3* and *4*), metal cylinders covered by chiral layers.

using the analytical representation of the Hankel function of the second kind [8]:

$$\begin{Bmatrix} E_z'' \\ H_z'' \end{Bmatrix} \approx \sqrt{2/\pi kr}\, e^{-i(kr-\pi/4)} \sum_{n=-\infty}^{+\infty} \begin{Bmatrix} C_n \\ D_n \end{Bmatrix} e^{in(\varphi+\pi/2)}. \quad (9)$$

For the far zone, it is common practice to introduce a new parameter, namely, the scattering field cross-section, which in our case is determined as follows:

$$\begin{Bmatrix} \sigma_\varphi^E/\lambda \\ \sigma_\varphi^H/\lambda \end{Bmatrix} = 10\log\left|\sum_n \begin{Bmatrix} C_n \\ D_n \end{Bmatrix} e^{in(\varphi+\pi/2)}\right|^2, \quad (10)$$

where the superscripts *E* and *H* refer to the cases of *E*- and *H*-polarized incident waves, respectively.

Figure 2 shows the dependences of the scattering field on the angle φ for *E*- and *H*-polarized plane electromagnetic incident waves, for different geometric dimensions of the metal rod and the chiral cylinder. The numerical analysis was performed for a chiral medium with the parameters $\varepsilon = 3.5 - i \times 0.2$, $\mu = 2.2 - i \times 0.2$, and $\xi = 0.3$. In such a medium, the effect of chirality on the wave processes is substantial. Figure 2a presents for comparison the scattering field diagrams for a homogeneous chiral cylinder ($kR_0 = 0$) and a homogeneous dielectric cylinder ($kR_0 = 0$, $\xi = 0$) in the case of an *E*-polarized incident wave. As one can see from Fig. 2a, for a polarized plane electromagnetic wave, the maximum reflection is observed at $\varphi = 0$ from both chiral and dielectric homogeneous cylinders. The introduction of a conducting rod smoothes out the scattering diagram, i.e., the scattering diagram ceases exhibiting sharp maxima or minima. An increase in the radius of the conducting rod kR_0 up to 0.7 does not affect the shape of the scattering pattern characterizing the wave scattering from the structure under consideration.

Figure 2b presents similar dependences for the case of an *H*-polarized electromagnetic incident wave. One can see that, for homogeneous cylinders, a maximum of the scattering field is observed at $\varphi = 0$, while for a chiral–metal scatterer, the scattering fields at $\varphi = 0$ and $\varphi = \pi$ are virtually equal. An increase in the radius kR_0 produces no changes in the shape of the scattering diagram.

The study of the field in the near zone (the calculation by formulas (7)) led us to an interesting conclusion about the depolarized component of the reflected field. In the case of an *E*-polarized plane electromagnetic incident wave, the introduction of a conducting rod into the chiral cylinder reduces the magnitude of this component, while in the case of an *H*-polarized plane electromagnetic wave, the introduction of a rod leads to its increase. It was also found that the presence of losses in the chiral medium (imaginary parts of ε and μ) increases the depolarized field for both types of the polarization of the incident wave.

REFERENCES

1. M. V. Kostin and V. V. Shevchenko, Radiotekh. Élektron. **43** (8), 921 (1998).
2. A. G. Dmitrenko and S. V. Korogodov, Radiofiz. **46** (4), 495 (1998).
3. V. A. Neganov, O. V. Osipov, and M. A. Sidorova, Fiz. Volnovykh Protsessov i Radiotekh. Sistemy **1** (1), 12 (1998).
4. A. I. Fedorenko, Radiotekh. Élektron. **40** (3), 381 (1995).
5. C. F. Bohren, J. Colloid Interface Sci. **66** (1), 105 (1978).
6. S. A. Tret'yakov, Radiotekh. Élektron. **39** (2), 184 (1994).
7. B. Z. Katsenelenbaum, E. N. Korshunova, A. N. Sivov, *et al.*, Usp. Fiz. Nauk **167** (11), 1201 (1997) [Phys.–Usp. (1997)].
8. *Handbook of Mathematical Functions with Formulas, Graphs, and Mathematical Tables*, Ed. by M. Abramowits and I. A. Stegun (Dover, New York, 1968; Nauka, Moscow, 1979).

Translated by E.M. Golyamina

Technical Physics Letters, Vol. 26, No. 1, 2000, pp. 4–5. Translated from Pis'ma v Zhurnal Tekhnicheskoĭ Fiziki, Vol. 26, No. 1, 2000, pp. 9–12.

The Rate of Transverse Propagation of Normal Zone in Aluminum-Stabilized Superconducting Windings

V. V. Lysenko and O. P. Anashkin

Kurchatov Institute Russian Scientific Center, Moscow, 123182 Russia

Received January 16, 1998; in final form, January 29, 1999

Abstract—Transverse propagation of the normal zone in superconducting windings of a conductor with a copper-aluminum stabilizing matrix was measured in compounded and uncompounded model coils. The special coil design enables one to simulate the one-dimensional propagation of normal zone in the winding in the radial direction. © *2000 MAIK "Nauka/Interperiodica".*

A distinction is usually made between two basic mechanisms of the normal zone propagation in immersion-type superconducting magnets, namely, the propagation along the conductor and the propagation due to diffusion of heat through interturn insulation [1]. Despite the fact that the characteristic ratio of the normal zone propagation rates for the longitudinal and transverse directions is of the order of 100, the mechanism of interturn propagation plays a major part in the process of normal zone growth in the majority of cases of practical importance [2].

This paper deals with the results of measurements of the rate of interturn propagation of the normal zone in the radial direction in model windings of a superconductor with a stabilizing matrix of aluminum plated with a thin layer of copper [3, 4]. The conductor measured 3.5×2 mm, with the copper coating thickness of about 50 μm. A niobium/titanium alloy-based composite superconducting wire, 0.7 mm in diameter, was sealed in the matrix groove. The conductor was insulated with a polyimide film, with the total insulation thickness of 0.12 mm. The measurements were made for conductors of two types differing by the matrix material, namely, Grade A5E technically pure aluminum and Grade A995 aluminum of relatively high purity. The values of residual resistivity of the conductors were 1.0×10^{-9} and 1.3×10^{-10} Ω m, respectively. The results of measurements of the rate of longitudinal propagation of the normal zone in these conductors, along with some other parameters, are given in [5].

The experiments were performed in small model coils of special design, which enabled one to simulate the process of one-dimensional propagation of the normal zone in the radial direction. In order to investigate the effect of liquid helium that might be present in the winding, the experiments were performed with both compounded and uncompounded coils. The coils were impregnated with ED20 epoxy compound by the wet winding technique. According to our estimates, in view of the density of winding, voids in the uncompounded winding accounted for not more than 3% of the overall volume.

The coils were wound onto textolite (resin-impregnated fabric laminate) frames and had an inside diameter of 58 mm, outside diameter of 110 mm, and length of 80 mm. The working layers to which the current was applied were the layers from the fourth to tenth, reckoning from the inside diameter. Three inner layers served to provide for the thermal boundary conditions. Each layer was wound using a separate piece of wire whose ends were led out to the frame ends where they were soldered to thick copper segments. The latter segments were thoroughly cooled with liquid helium, which ruled out the possibility of the normal zone transition from layer to layer due to propagation along the conductor. The layers were interconnected such that the direction of current in each subsequent layer was opposite to that in the preceding layer. Therefore, the self-magnetic field of the coil was low. A heater element in the form of a stainless foil strip 0.1 mm thick and two bandage layers were provided on top of the tenth layer of winding. The heater covered almost the entire external surface of winding in order to provide for an almost simultaneous transition of the layer to a normal state.

During measurements, the current of preassigned magnitude was delivered to the coil being investigated, the normal zone was initiated with the aid of the heater, and the voltage on the internal layers was recorded. The transport current in the coil and the external magnetic field were time-constant.

The figure gives the propagation rate values determined by the time of normal zone transit through three internal layers (from the eighth to fifth). The error of determining the propagation rate was approximately 10%. As is seen from the figure, the values of propagation rate for a conductor stabilized with Grade A5E aluminum proved to be much higher (by a factor of three to five) than the respective values for a conductor with the matrix on the basis of a higher purity A995 aluminum.

1063-7850/00/2601-0004$20.00 © 2000 MAIK "Nauka/Interperiodica"

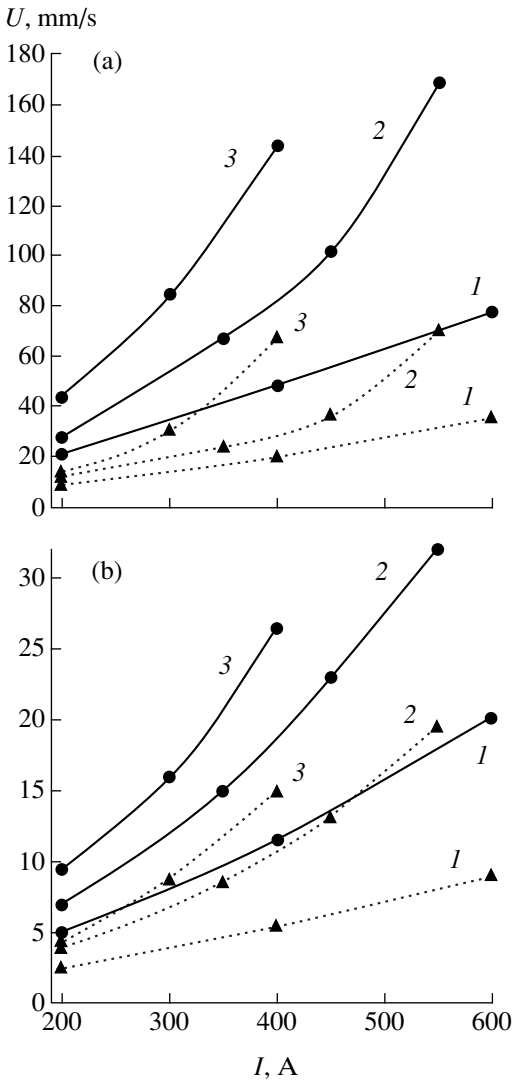

The rate of transverse propagation of the normal zone in a conductor stabilized with (a) Grade A5E aluminum and (b) Grade A995 aluminum as a function of current. The external magnetic field is (*1*) 0, (*2*) 2, and (*3*) 4 T. The circles indicate compounded winding, and the triangles indicate uncompounded winding.

The measurement results demonstrated a considerable decrease of the normal zone propagation rate (by a factor of two–three) in uncompounded windings as compared with compounded ones. This result may possibly be attributed to a higher transverse thermal conductivity of insulation in sized winding and to the effect of liquid helium contained in the voids of uncompounded winding. As great a difference between the values of propagation rate in compounded and uncompounded coils was also observed in the case of longitudinal propagation of the normal zone in such windings [5], which may only be explained by the effect of liquid helium and not by the difference in the thermal conductivity of insulation. Indeed, the contribution of insulation to the effective longitudinal thermal conductivity of the winding is negligibly small, and the effect of transverse diffusion of heat, in this case, is quite the opposite, that is, an increase in transverse heat transfer leads to a decrease in the rate of longitudinal propagation of normal zone. We believe that the effect of liquid helium present in the interturn space of uncompounded coils was the most important factor causing a decrease of the propagation rate in the case of transverse propagation of normal zone as well.

The experimentally obtained values of the propagation rate of the normal zone in aluminum-stabilized superconductors are essential to designing the shielding of large superconducting magnets manufactured from conductors of this type.

ACKNOWLEDGMENTS

This study was received the in-house grant no. 32 of the Kurchatov Institute Russian Scientific Center and a Leading Scientific School grant (96-15-98230) of the Russian Foundation for Basic Research.

REFERENCES

1. M. N. Wilson, *Superconducting Magnets* (Oxford Univ. Press, London, 1983; Mir, Moscow, 1985), p. 405.
2. C. H. Joshi and Y. Iwasa, Cryogenics **29**, 157 (1989).
3. V. E. Keilin, O. P. Anashkin, and A. V. Krivikh, Adv. Cryog. Eng. **38**, 699 (1992).
4. V. E. Sytnikov, A. V. Rychagov, Ju. P. Ipatov, *et al.*, Adv. Cryog. Eng. **38**, 703 (1992).
5. V. V. Lysenko and O. P. Anashkin, Pis'ma Zh. Tekh. Fiz. **23** (13), 52 (1997) [Tech. Phys. Lett. **23** (7), 518 (1997)].

Translated by H. Bronsteĭn

Technical Physics Letters, Vol. 26, No. 1, 2000, pp. 41–43. Translated from Pis'ma v Zhurnal Tekhnicheskoĭ Fiziki, Vol. 26, No. 1, 2000, pp. 84–89.

Doping of Silicon Layers from a Sublimating Erbium Source in Molecular Beam Epitaxy

S. P. Svetlov, V. Yu. Chalkov, V. G. Shengurov, E. A. Uskova, G. A. Maksimov, B. A. Andreev, Z. F. Krasil'nik, M. V. Stepikhova, and H. Ellmer

Research Physicotechnical Institute, Niznhi Novgorod State University, Nizhni Novgorod, Russia

Received August 6, 1999

Abstract—The preparation of light-emitting rare-earth-doped (Er) silicon structures has been considered. A new technique of erbium doping of silicon layer during its growth by the molecular beam epitaxy method is suggested. © *2000 MAIK "Nauka/Interperiodica".*

In the recent decade, we evidence an increase of the interest in erbium-doped silicon as a possible material for designing emitters operating at the wavelength of 1.54 μm, i.e., in the range of the minimum losses in quartz-fiber light-guides [1]. According to the well-known estimates, highly efficient devices can be designed only if the concentration of the optically active erbium-containing centers is not lower than 1×10^{18} cm^{-3}. At the same time, the introduction of a large amount of erbium should not deteriorate the crystal structure of doped silicon.

There are various methods providing the introduction of erbium into the silicon matrix such as the ion implantation [2], the plasma-enhanced chemical deposition from the gas phase [3], and the molecular-beam epitaxy (MBE) [4, 5]. However, ion implantation of erbium requires the use of high-energy ions (0.5–5.0 MeV), which gives rise to considerable deterioration of the silicon crystal lattice, which cannot be completely removed by the subsequent prolonged annealing of the specimens. In the method of plasma-enhanced chemical deposition from the gas phase, the epitaxial erbium-doped silicon layers contain carbon at high concentrations, which has a negative effect on the photoluminescence. The coevaporation of erbium and silicon in the MBE process allows one to grow thick erbium-doped silicon layers without the recrystallization stage essential in the method of ion implantation. In the conventional MBE method, erbium and most of other dopants are evaporated with the use of an effusion cell. A perfect effusion cell is an important and complicated unit of am MBE setup. Moreover, one cannot exclude the formation of clusters in the vapors of the material evaporated from the cell, which can also affect the quality of the epitaxial layers grown and the process of impurity incorporation into the material [6].

We had the aim to study the possibilities of doping of an epitaxial silicon layer with erbium during its growth using a flow of molecular erbium from the resistively heated strip of Er (as far as we know, it was the first attempt of this kind) and the structure, composition, electrical, and optical characteristics of the thus grown Er-doped epitaxial silicon layer.

The epitaxial silicon layers were grown by the method of sublimation MBE [5]. The source of Si atoms was a rectangular bar cut out from a high-resistance silicon ingot heated by a transmitted current to the temperature up to 1380°C. The flow of erbium atoms was created by its sublimation from an erbium strip resistively heated up to 800–950°C. The substrates were (100)-oriented (within ~0.15°) *p*-Si wafers with the resistivities of 12 and 0.005 Ω cm.

To remove a native silicon-oxide layer from the surface, the substrate was annealed for 10 min at 1250°C. Then, upon the decrease of the temperature down to 1000°C, a 0.2 μm-thick buffer Si layer was grown on the substrate. Growth of the erbium-doped layer was started at the moment, when the substrate temperature was decreased down to 550–500°C. The thus grown layers had the thicknesses ranging within 4–6 μm.

The defects in the epitaxially grown silicon layers were studied in an optical microscope on the layers subjected to preliminary selective etching. The structure perfection of the layers was checked by the reflection electron diffraction method. Erbium concentration was determined by the Rutherford back-scattering method with the use of 600 keV ^{4}He-ions. The concentration and distribution of the charge carriers in the layers were determined from the data on the Hall effect and the *C–V* characteristics measured at room temperature, respectively. The photoluminescence spectra were recorded at a resolution not lower than 1 cm^{-1} in a *Bomem DA3* vacuum Fourier-spectrometer in the range 3000–12000 cm^{-1}.

We have established that in the layers grown at the erbium-source temperatures 850 and 950°C, the erbium concentration in the layer attained the values of 5×10^{18} and $\sim 1 \times 10^{21}$ cm^{-3}, respectively (Rutherford back-scattering data). A typical Rutherford-back scat-

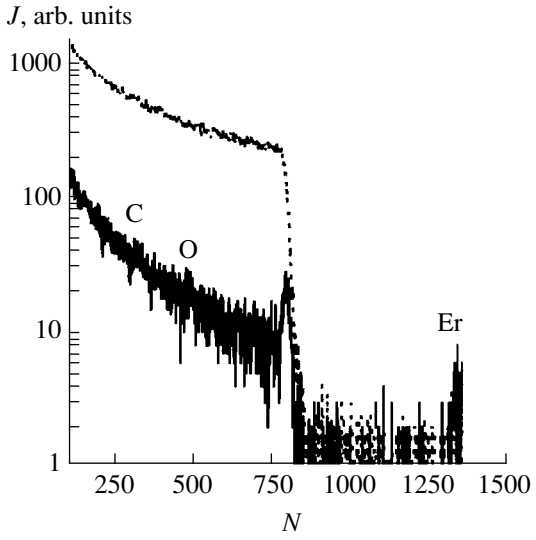

Fig. 1. Rutherford back-scattering spectra of ^{4}He-ions incident onto Er-doped Si-layers obtained at the erbium-source temperature 850°C (solid line indicated the ⟨100⟩ orientation and dashed line indicates an arbitrary orientation), N is the number of the recording channels.

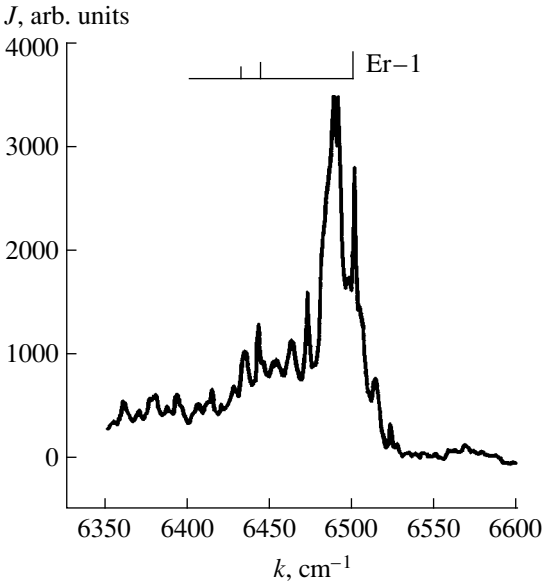

Fig. 2. Photoluminescence spectrum from the erbium-doped epitaxial silicon layer with the Er concentration up to 5×10^{18} cm^{-3} (k is the wave number).

tering spectrum from the epitaxial layer of erbium-doped (5×10^{18} cm^{-3}) silicon is shown in Fig. 1. Usually, the epitaxial layers had a sufficiently high degree of perfection: the minimum surface yield of helium ions was equal to 0.033, which corresponds to the theoretical estimates for the defect-free silicon. The only exception was a layer with the erbium concentration about 1×10^{21} cm^{-3}, showing a much worse crystallinity (the minimum yield of helium ions 0.33). These data were also confirmed by the electron-diffraction study: the first specimen provided the formation of a Kikuchi pattern, whereas the second one, the mosaics-block pattern.

A more detailed study of the real structure of the epitaxial layers showed that the surface of perfect single-crystal films ($N_{Er} \le 5 \times 10^{18}$ cm^{-3}) is characterized by a low density of point defects, 10^2 cm^{-2}. In the layers with the Er concentration exceeding 5×10^{18} cm^{-3}, the dislocation density attains the value ranging within 10^2–10^3 cm^{-2}; whereas, the stacking-fault density attains the value ranging within 10^3–10^4 cm^{-2}.

According to the electric measurements, the structures grown had the *n*-type conductivity (see table). An increase of the temperature of the Er-source in the range 800–900°C increased the electron concentration in the epitaxially grown layer from 2×10^{15} up to 4×10^{17} cm^{-3}.

Table

T_{Er}, °C	Electron concentration (in cm^{-3}) obtained from	
	C–V curves	Hall measurements
800	–	$(2.5–5) \times 10^{15}$
850	2×10^{16}	1.5×10^{16}
900	2×10^{17}	4×10^{17}

A further increase of T_{Er} up to 920–950°C changed the carrier concentration and the conductivity type: $p > 4 \times 10^{16}$ cm^{-3}. Similar changes in the concentration of Er-doped epitaxial silicon layers were also observed with the variation of other growth parameters used in this technology, e.g., with a deliberate increase of the pressure in the working chamber. It should also be noted that the measured charge-carrier concentration was lower, from one to three orders of magnitude, than the concentration of erbium atoms in the layer.

As an example, Fig. 2 shows the photoluminescence spectrum of the erbium-doped epitaxial silicon structure obtained at the erbium-source temperature 850°C. An intense photoluminescence was also observed in the vicinity of 1.54 μm (6400–6550 cm^{-1}) at low temperature (42 K), which was associated with the $I_{13/2} \longrightarrow 1_{15/2}$ transitions in the 4*f*-shell of an Er^{3+} ion. An intense low-temperature photoluminescence was also observed in the layer with the maximum erbium concentration ($\sim 1 \times 10^{21}$ cm^{-3}) attained in our experiments upon specimen annealing in the nitrogen atmosphere at 800°C.

Thus, we have suggested a new method for doping Si-layers with erbium from a metal source during the sublimation process, which provides the formation of epitaxial Si layers with a rather high degree of structural perfection emitting in the vicinity of 1.54 μm. At the erbium-source temperature ranging within 800–950°C,

the erbium concentration in silicon layers can be controlled within 10^{18}–10^{21} cm^{-3}.

ACKNOWLEDGMENTS

This study was supported by the Russian Foundation for Basic Research, project nos. 98-02-16619 and 99-03-32757 and the Program of Ministry of Science and Technologies *Fundamental Spectroscopy*, project no. 08.02.043.

REFERENCES

1. N. A. Sobolev, Fiz. Tekh. Poluprovodn. (St. Petersburg) **29** (7), 1153 (1995) [Semicond. **29** (7), 595 (1995)].
2. A. Polman, J. Appl. Phys. **82** (1), 1 (1997).
3. I. L. Rogers, P. S. Andry, and W. J. Varhue, Appl. Phys. **78** (2), 6241 (1995).
4. J. Simmer, A. Rettinger, G. Abstreiter, *et al.*, Mat. Res. Soc. Symp. Proc. **422**, 15 (1996).
5. V. G. Shengurov, S. P. Svetlov, D. A. Pavlov, *et al.*, Izv. Akad. Nauk, Ser. Fiz. **63** (2), 406 (1999).
6. *Molecular-Beam Epitaxy and Heterostructures*, Ed. by L. L. Chang and K. Ploog (Martinus Nijhoff, Amsterdam, 1985; Mir, Moscow, 1989).

Translated by L. Man

Technical Physics Letters, Vol. 26, No. 1, 2000, pp. 44–45. Translated from Pis'ma v Zhurnal Tekhnicheskoĭ Fiziki, Vol. 26, No. 1, 2000, pp. 90–94.

Orientation Effects under the Conditions of a Fröhlich Breakdown in Silicon Carbide Crystals

V. A. Karachinov

Yaroslav Mudryĭ State University, Novgorod, Russia

Received May 24, 1999

Abstract—The paper presents the results of an experimental study of brittle fracture of SiC crystals under the conditions of electric breakdown. *© 2000 MAIK "Nauka/Interperiodica".*

(1) For some technical applications of silicon carbide, it is necessary to obtain single crystals with a given shape, a given degree of doping, and a low concentration of extended defects [1, 2]. Among the known methods of dimension profiling of SiC, the electric erosion in liquid dielectrics is the one that makes it possible to satisfy the aforementioned requirements. The electric erosion is accompanied by different physical effects including the electrical breakdown of SiC [3–5].

Two types of breakdown, namely, the surface breakdown and the volume one, lead to the fracture of a SiC crystal through the formation of special types of defects (breakdown patterns), which can be inherited. In addition, the effect of pulsed electric discharges on SiC crystals, which are fairly brittle at temperatures below 600–500°C, may lead to the formation of cracks [6]. It is well known that the cracking of many organic crystals leads to the so-called Fröhlich breakdown, which is characterized by rapid development and arbitrary orientations of the breakdown directions [7].

This paper presents the results of an experimental study of brittle fracture of SiC crystals under the conditions of electrical breakdown.

(2) The electrical breakdown of SiC crystals was studied in a laboratory setup containing a single-pulse generator and a system of electrodes of the needle–plane type. The pulse energy could be measured within the interval $E_{puls} = 1.1 \times 10^{-2}$–0.9 J, and the voltage was within the interval U = 0–300 V.

In the experiments, we used steel electrodes, and the medium was transformer oil at room temperature.

The initial materials for the studies were SiC single crystals of 6H polytype in the form of thin plates and bulk crystals with both natural faces and surfaces subjected to polishing and etching in KOH melt. The sample thickness was 450–4000 μm, the uncompensated donor concentration was N_d–$N_a \approx 5 \times 10^{18}$ cm^{-3}, and the dislocation density was $N_d = 1 \times 10^4$–5×10^5 cm^{-2}.

The morphological features of the breakdown patterns obtained in SiC were studied by optical and chemical methods (a metallographic microscope and etching in KOH melt), as well as by scanning electron microscopy (BS-340).

According to the data of the scanning electron microscopy, the fracture zone formed by a partial breakdown of SiC was in some parameters similar to an indentation pattern produced by a sharp mechanical indenter [8]. The structure of the fracture zone contained a main pit and a system of radial and circular cracks. In addition, secondary cracks oriented parallel to the crystal surface and causing chips of material were present. The fracture occurred mainly along the cleavage planes, although some breaks along the slip planes were also observed [9].

The optical studies of the fracture zone were performed in both ordinary and polarized light. These studies revealed stressed regions and regions of SiC foliation the boundaries of which were visible owing to the interference of light [10]. Two dominant factors, namely, the face orientation and the dislocation structure of SiC, determined the evolution of the fracture zone. The table presents the experimental values of the threshold energy of the electric pulse that causes brittle

Table

Single crystals	Pulse energy, J (without a contact between the needle electrode and the face)			
Face	(0001)C	(0001)Si	$(11\bar{2}0)$	$(10\bar{1}0)$
Thin plates (the Lely method)	0.7	0.7	0.4	0.08–0.09
Bulk crystals (the LÉTI method, argon, T_p = 2400 K)	0.6	0.6	0.3	0.08

1063-7850/00/2601-0044$20.00

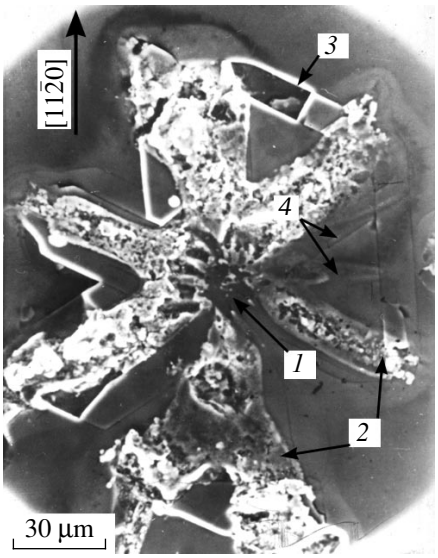

Breakdown pattern obtained with the needle electrode touching the surface of a thin single-crystal plate (photograph, scanning electron microscopy, the (0001)Si face, E_{puls} = 0.36 J, and τ = 120 μs): (*1*) the region of contact between the electrode and the face; (*2*) radial erosion pits; (*3*) border with a chip of material; and (*4*) breakdown channels.

fracture of 6H-SiC. The effect of the dislocation structure manifested itself in the form of groove patterns and cleavage (the (0001) plane).

(3) In the experiments with a needle electrode brought into contact with the (0001)Si face, star-shaped breakdown patterns (see figure), which resembled dislocation rosettes, were observed. However, by etching the crystals with such breakdown patterns in KOH melt, no traces of slip could be revealed. The etch patterns contained isolated groups of hexagonal etch pits (which presumably were related to the growth dislocations) and etch grooves oriented along the cracks.

As seen from the figure, the structure of the breakdown patterns contains radial erosion pits, breakdown channels, and cracks. The pits are filled with the products of SiC destruction and intersect at the point where the needle electrode touches the crystal surface. The tips of the pits are closed by fragments of a border formed by a circular crack. Within the border, chips of material with smooth surfaces were observed. By correlating the crystallographic indices of the fracture traces forming a star (pits, cracks, and chips) with the known elements of brittle fracture of 6H-SiC (of wurtzite type), we reveal two main fracture systems: along the $\{10\bar{1}0\}$ cleavage planes and along the (0001) cleavage plane.

The experiments showed that the radial erosion pits are formed by the channels of the partial breakdown of SiC. Their formation is related to oriented electron avalanches that have maximum energy in the $\langle 11\bar{2}0\rangle$ direction [11]. The thermal destruction of SiC, which occurs over the entire channel length, destroys the face surface and leads to the formation of a radial pit. The electron avalanches that occur in the $\langle 10\bar{1}0\rangle$ directions possess lower energies, their trajectories directed into the crystal bulk make greater angles with the surface, and they cause no breaks. The effects of orientation of the electric breakdown and, hence, the formation of the corresponding shock waves are the main mechanisms governing the formation of the system of cracks and chips in the star [12].

(4) In closing, we formulate the main results of the study:

(a) In a SiC crystal, a partial breakdown may be accompanied by a brittle fracture of the crystal through the formation of breakdown patterns whose morphology and structure depend on the face orientation and the specific features of the dislocation structure.

(b) The threshold values of the electric pulse energy sufficient for producing brittle fracture of the faces of a SiC crystal are determined.

(c) In the case of a needle electrode brought into contact with the crystal surface, the effect of the orientation of the electric breakdown forms a star-shaped breakdown pattern.

REFERENCES

1. Yu. L. Vodakov, G. A. Lomakina, and E. N. Mokhov, in *Doping of Semiconductors* (Nauka, Moscow, 1982), pp. 230–233.
2. V. A. Karachinov, in *Proceedings of the III International Conference "Crystals: Growth, Properties, Real Structure, and Applications," Aleksandrov, Russia, 1997*, Vol. 2, p. 154.
3. V. N. Levin, Yu. M. Tairov, M. G. Travadzhyan, *et al.*, Izv. Akad. Nauk SSSR, Neorg. Mater. **14** (6), 1062 (1978).
4. O. G. Bazhenov and V. A. Karachinov, Pis'ma Zh. Tekh. Fiz. **22** (21), 26 (1996) [Tech. Phys. Lett. **22**, 875 (1996)].
5. G. B. Lisenkov, V. P. Snegirev, and A. S. Tager, Pis'ma Zh. Tekh. Fiz. **10** (4), 215 (1984) [Sov. Tech. Phys. Lett. **10**, 89 (1984)].
6. V. A. Karachinov, Zh. Tekh. Fiz. **68** (7), 133 (1998) [Tech. Phys. **43**, 868 (1998)].
7. *Progress in Dielectrics*, Ed. by J. B. Birks and J. H. Schulman (Heywood, London, 1959; GÉI, Moscow, 1962).
8. Yu. S. Boyarskaya, D. Z. Grabko, and M. S. Kats, *Physics of Microindentation Processes* (Shtiintsa, Kishinev, 1986).
9. A. A. Predvoditelev, Kristallografiya **7** (6), 938 (1962) [Crystallography Reports **7**, 759 (1962)].
10. M. M. Fokht, *Photoelasticity. Polarization-Optical Method of Stress Study* (Gostekhizdat, Moscow, 1948).
11. Yu. A. Vodakov, A. O. Konstantinov, D. P. Litvin, *et al.*, Pis'ma Zh. Tekh. Fiz. **7** (12), 705 (1981) [Sov. Tech. Phys. Lett. **7**, 301 (1981)].
12. A. B. Tolstykh, in *Electric Discharge in Liquid and Its Application* (Naukova Dumka, Kiev, 1977), pp. 157–160.

Translated by E.M. Golyamina

Technical Physics Letters, Vol. 26, No. 1, 2000, pp. 46–48. Translated from Pis'ma v Zhurnal Tekhnicheskoĭ Fiziki, Vol. 26, No. 2, 2000, pp. 1–7.

Nickel Sputtering by High-Energy Heavy Ions

A. Yu. Didyk*, V. K. Semina*, A. Khalil, N. A. Vasil'ev**, A. É. Stepanov**, A. L. Suvorov**, and Yu. N. Cheblukov****

** Flerov Laboratory of Nuclear Reactions, Joint Institute for Nuclear Research, Dubna, Moscow oblast, 141980 Russia*

*** Institute of Theoretical and Experimental Physics, State Research Center of the Russian Federation, Moscow, 117259 Russia*

Received September 18, 1999

Abstract—Recent experimental data on the sputtering of coarse-grained metals by high-energy heavy ions are reviewed. It is pointed out that inelastic energy losses of ions have rather insignificant effect on the sputtering yield of metals. Experimental data on the sputtering of nickel by $^{86}Kr^{+}$ ions are presented. The accumulation of radiation defects in the crystal lattice of nickel in the course of irradiation leads to an increase in the metal sputtering yield from the surface of grains, making it comparable with the sputtering yield from the intergranular region. The results of such experiments are important for development of the heavy ion acceleration facilities and for the high-energy heavy-ion doping of deep layers in semiconductors. *© 2000 MAIK "Nauka/Interperiodica".*

INTRODUCTION

The sputtering of metals by ions in the low-energy range, where the elastic energy losses are dominating, is studied in sufficient detail. It has been established that the sputtering process in this energy range is well described by the cascade mechanism [1].

The interest of researchers toward investigations of the sputtering of coarse-grained metals by heavy ions in the range of inelastic energy losses has grown only in the past decade in connection with the task of acceleration and storage of high-intensity heavy-ion beams in the storage ring facilities such as heavy-ion drivers [2]. In particular, the sputtering yields of gold from coarse-grained targets bombarded by high-energy ^{238}U and ^{84}Kr ions were experimentally studied in [3, 4]. Recently, experimental data on the sputtering of Au, Zr, and Ti by fast Au ions were reported in [5], where it was also pointed out that the growing interest toward sputtering in the range of inelastic energy losses is related to the use of fast ion bombardment for the implantation of deep layers.

The experimental results reported in [3–5] are summarized in the table. All these experiments were performed with crystalline targets. In most cases (see table), the sputtering yields exceed, albeit rather insignificantly, the values calculated according to the cascade model. Comparatively small absolute values of the sputtering yield indicate that high-energy heavy ions travelling in a metal target do not form hot tracks that would lead to evaporation of the metal. A possible mechanism responsible for the energy transfer from the electron subsystem, excited as a result of the high-energy heavy-ion penetration, to the surface atoms and for their sputtering was considered in [6].

In the course of operation of a heavy-ion driver, the structural metal elements both in the linear accelerator and in the side walls of storage rings are exposed to considerable fluences of ions escaped from the acceleration process. In this case, the physics of metal sputtering from these elements may be quite different. The high-energy heavy-ion bombardment will result in the accumulation of radiation-induced defects in the metal crystal structure. In the sites of defect accumulation, the electron subsystem occurring in the hot state as a result of the heavy-ion penetration will effectively transfer energy to atoms of the substance. This may give rise to significant local heating of these atoms and result in the formation of high-temperature tracks [7]. Moreover, as noted in [8], this may switch on the evaporation sputtering mechanism, whereby the metal sputtering yield would increase to a considerable level.

Experimental sputtering yields S_{exp} of crystalline metals bombarded by heavy ions in the range of inelastic energy losses

Projectile/target	Ion energy, MeV	Sputtering yield		Ion energy losses, keV/Å
		experiment (S_{exp})	cascade theory (S_{th})	
$^{238}U/^{196}Au$	1400	12 ± 2	~1	9.9
$^{196}Au/^{48}Ti$	230	3.3 ± 0.5	~0.2	2.7
$^{196}Au/^{196}Au$	230	9.3 ± 0.9	~3	5.4
$^{196}Au/^{91}Zr$	230	1.7 ± 0.2	1.07	2.9
$^{84}Kr/^{196}Au$	200	1.0 ± 0.2	≤1	3.0

1063-7850/00/2601-0046$20.00 © 2000 MAIK "Nauka/Interperiodica"

EXPERIMENTAL

We have experimentally studied the sputtering of nickel by $^{86}Kr^{+}$ ions with an energy of E = 245 or 305 MeV at a high fluence of $Ft > 10^{15}$ cm^{-2}, where F is the ion beam current density and t is the irradiation time. In the course of irradiation, the ion beam current density was about $F \approx (1–2) \times 10^{11}$ cm^{-2} s^{-1}. The ion fluences and beam current densities were determined with a ±5% accuracy.

Prior to experiments, the nickel samples were electrically polished in order to provide for a good quality of the surface and then annealed in a vacuum of 10^{-3} Pa at 700°C for one hour. Before and after irradiation, the samples were studied in a Jeol JSM-840 scanning electron microscope (SEM). The samples were ion bombarded in a vacuum of 10^{-4} Pa. During the irradiation, the sample holder was cooled with flowing water so as to maintain the sample (glued to the holder with a heat-conducting glue) at room temperature.

RESULTS AND DISCUSSION

Figure 1 shows SEM images of the surface of a Ni sample (a) before and (b) after irradiation by 305-MeV $^{86}Kr^{+}$ ions to a total fluence of $Ft \approx 2 \times 10^{15}$ cm^{-2}. As seen from these micrographs, the ion bombardment leads to leveling of inhomogeneities on the sample surface, rendering the irradiated surface practically smooth. A well-pronounced effect (cf. Figs 1a and 1b) is the markedly stronger sputtering of nickel from the grain boundary region. The sputtering yield of nickel from this region reaches $S \geq 2000$ atoms/ion, which is four times the value for the grain surface.

The sputtering yields were estimated by approximately determining the amount of substance in the inhomogeneities sputtered from the sample surface. For a more precise determination of the sputtering yield, half of the irradiated surface of a nickel sample exposed to a fluence of $Ft \approx 2 \times 10^{15}$ cm^{-2} was screened with a diaphragm and the sample was additionally irradiated by 245-MeV $^{86}Kr^{+}$ ions to a fluence $Ft \approx 10^{15}$ cm^{-2}. The height of the step between doubly and singly sputtered areas was $h \approx 0.35$ μm (Fig. 2), which corresponds to a sputtering yield of $S_{Ni} \approx 3000$ atoms/ion. This result indicates that the sputtering yield of nickel from the grain surface at large fluences approaches the value for the grain boundary, that is, for the region of disordered crystalline structure of the metal.

The time of momentum transfer from the electron subsystem (excited by the heavy ion penetration) to atoms in the crystal lattice is of the order of $\tau \approx 10^{-12}$ s, during which the metal atoms cannot be heated to significant temperatures [7]. However, the energy transfer time reduces to $\tau \approx 10^{-13}$ s time in a crystal with sufficiently large number of radiation-induced defects. This may lead to a significant local heating of the metal, with

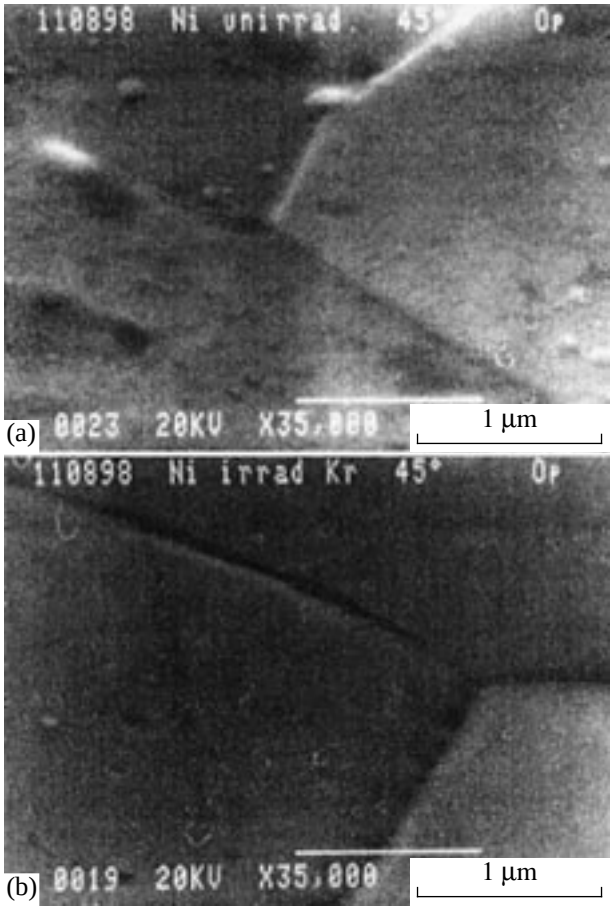

Fig. 1. SEM images of the surface of polycrystalline Ni target (a) before and (b) after irradiation by 305-MeV $^{86}Kr^{+}$ ions to a fluence of $Ft \approx 2 \times 10^{15}$ cm^{-2}.

the resulting melting and hot track formation [7]. The final temperature at the track axis can be estimated using the following formula [7]:

$$\Theta(0) = \sqrt{\frac{8\pi}{9}\frac{\hbar S^2}{a} N\sigma_0 \frac{\alpha}{\beta} r_0^2 T_0^{1/2}\left(\left(\frac{T_0}{\varepsilon_F}\right)^{3/2} - 1\right)},$$

where $\sigma = 2\pi a_0^2$, a_0 is Bohr's atomic radius, S is the sound velocity, N is the density of atoms in the target, r_0 is the initial radius of the region of electron excitation, T_0 is the initial electron temperature in this excited region, a is the lattice constant, α and β are constant quantities weakly dependent on the atomic number of the target for $Z \geq 20$ ($\alpha \sim 0.05$; $\beta \sim 0.1$ eV^{-1}).

A large sputtering yield of nickel observed in our experiments (Figs. 1 and 2) is apparently explained by the evaporation of metal atoms from the surface of tracks heated to a temperature much above the melting point of the target material. The melting temperature of nickel is T_m = 1873 K, while estimation by the formula gives $\Theta \approx 3700$ K.

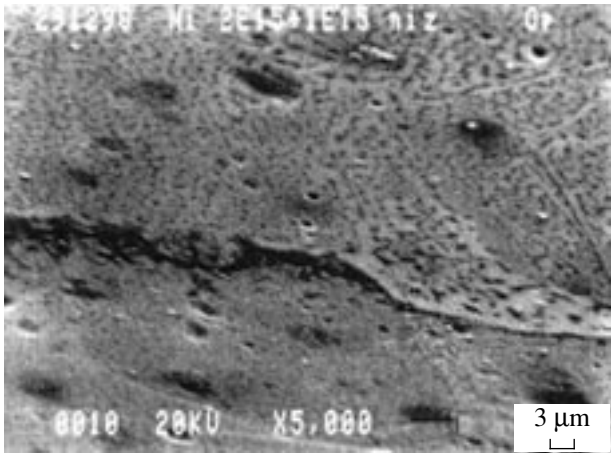

Fig. 2. SEM image of the surface of a polycrystalline Ni target irradiated by 305-MeV $^{86}Kr^{+}$ ions to a fluence of $Ft \approx 2 \times 10^{15}$ cm^{-2} and then additionally bombarded by 245-MeV $^{86}Kr^{+}$ ions to a fluence of 1×10^{15} cm^{-2} with half of the sample surface screened by a diaphragm. The step between two parts of the sample surface is clearly seen.

As is seen from the experimental data (Figs. 1 and 2), the presence of radiation defects in a metal markedly increases the effect of the inelastic energy losses of high-energy heavy ions on the sputtering yield of metal targets. For example, typical sputtering yields of metals from crystalline targets with small numbers of defects in the crystal structure are 1–10 atoms/ion [3–5]. As is seen on the example of nickel, the accumulation of defects in the metal crystal structure leads to increase in the sputtering yield from crystalline grains, which becomes comparable with the sputtering yield of amorphized metal.

The theory of track formation [7] does not contradict the experimental data obtained. Taking into account that the problem studied in this work is extremely important for development of the ion accelerating facilities and the solving the problems of high-energy ion implantation into solids, it is necessary to continue investigations in this direction. The first task is to measure the angular distribution of atoms sputtered from a target surface and to study dependence of the sputtering yield on the irradiation dose in relationship with the type and concentration of radiation defects in the crystal structure.

ACKNOWLEDGMENTS

The authors are grateful to Celia Élliot for useful remarks. The work was supported by the International Scientific-Technological Center, project no. 467.

REFERENCES

1. P. Sigmund, Phys. Rev. **184**, 383 (1969).
2. D. G. Koshkarev, Part. Accel. **16**, 1 (1984).
3. Yu. N. Cheblukov, D. G. Koshkarev, A. R. Peuto, *et al.*, Part. Accel. **37**–**38**, 351 (1992).
4. G. I. Akap'ev, A. N. Balabaev, and N. A. Vasil'ev, Zh. Tekh. Fiz. **68** (1), 134 (1998).
5. H. D. Mieskes, W. Assmann, M. Brodale, *et al.*, Nucl. Instrum. Meth. Phys. Res., Sect. B **146**, 162 (1998).
6. Yu. N. Martynenko and Yu. N. Yavlinskiĭ, Zh. Tekh. Fiz. **58** (6), 1164 (1988).
7. Yu. N. Yavlinskiĭ, Nucl. Instrum. Meth. Phys. Res., Sect. B **146**, 142 (1998).
8. Yu. N. Cheblukov, Proc. 1st Moscow Int. School in Physics (Institute of Theoretical and Experimental Physics, Moscow, 17–26 February 1998) [in Russian] (Usp. Fiz. Nauk, Moscow, 1999), p. 181.

Translated by P.P. Pozdeev

Technical Physics Letters, Vol. 26, No. 1, 2000, pp. 49–50. Translated from Pis'ma v Zhurnal Tekhnicheskoĭ Fiziki, Vol. 26, No. 2, 2000, pp. 8–12.

Laser-Initiated Anomalous Diffusion of Oxygen in a Surface Silicon Layer Enriched with Defects

A. F. Banishev, V. S. Golubev, and A. Yu. Kremnev

Institute of Problems in Laser and Information Technologies, Russian Academy of Sciences, Shatura, Russia

Received July 5, 1999

Abstract—The effect of anomalously slow relaxation of deformation of silicon surface after laser stimulation is revealed and described. This effect is attributed to "cold" diffusion of oxygen in the surface layer enriched with defects. © *2000 MAIK "Nauka/Interperiodica".*

Laser radiation is widely used in numerous processes of material treatment [1–4], in particular, in microelectronics for depositing thin oxide layers of preassigned shape and thickness on semiconductor surfaces [1–3], where laser radiation serves the function of the thermal activator of the rate of surface oxidation. However, when the surface of crystalline solids is subjected to the effect of laser pulses, structural defects such as vacancies and interstitial sites [5–9] may be generated in the surface layer, and the concentration of such defects during the course of a laser pulse may vary by several orders of magnitude as compared with the initial value and reach values of 10^{18}–10^{20} cm^{-3}. Therefore, the surface oxidation in this case is a fairly complex process of diffusion of oxygen into the surface layer of the material, in which the temperature and concentration of defects vary rapidly in time. The generation of a significant concentration of defects may substantially and uncontrollably change the rate and even the mechanism of surface layer oxidation, which is undesirable in depositing thin oxide layers of preassigned thickness.

One can expect the presence of an increased concentration of intrinsic defects and oxygen to result in a variation of the elastic and thermoelastic coefficients of the material (compression, shear, temperature expansion and thermal conductivity) and, as a consequence, in a variation of the dynamic characteristics of the deformation response of the surface to external stimulation.

In this study, we investigated the deformation response of the surface of single-crystalline silicon to the effect of short laser pulses in air and in vacuum, $P \approx 10^{-2}$ Torr. An anomalously long (in time) variation of surface relief upon irradiation in air was revealed. The surface deformation was recorded by the scattering of sampling beam of a He–Ne laser.

The experimental setup is shown schematically in Fig. 1. A sample of single-crystalline silicon with a mirror-finished surface oriented along the crystallographic direction (100) was placed in a vacuum chamber in which the pressure might vary form 10^{-2} Torr to 1 atm. The sample surface was irradiated with pulses of a YAG:Nd laser with a pulse energy $E \approx 0.5$–1 mJ and duration $\tau \approx 3 \times 10^{-7}$ s. Laser radiation was focused onto the sample surface in a spot sized $d \approx 0.3$–1 mm. The irradiation was performed by pulses with a power density below the melting threshold of the surface. The sounding of the irradiated surface region was made by the beam of a sampling He–Ne laser. Scattered radiation of the sampling laser was recorded at an angle $\alpha \approx 45°$ to the sample surface.

Figure 2 gives the variation of the signal intensity of scattered radiation of a sampling He–Ne laser on the silicon surface irradiated by pulses of a YAG:Nd laser in air and in vacuum. As one can see in the figure, the effect of YAG:Nd laser pulse results in an abrupt increase of scattering, with the scattering signal duration $t \approx 0.2$–0.5 s, which is almost six orders of magnitude longer than the duration of the effect of the YAG:Nd laser pulse on the surface, and the maximum

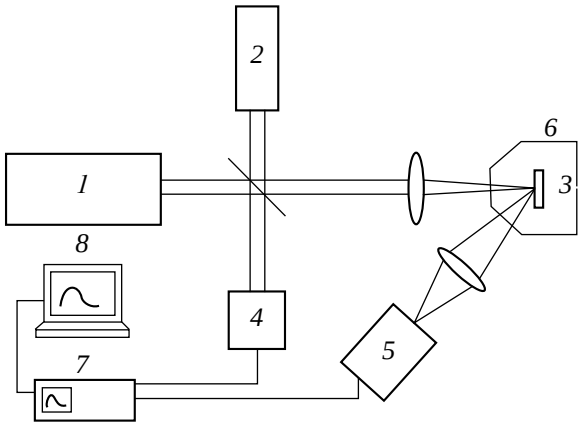

Fig. 1. Schematic of the experimental setup: (*1*) YAG:Nd laser, (*2*) He–Ne laser, (*3*) sample, (*4*) photodetector, (*5*) monochromator, (*6*) vacuum chamber ($P \approx 10^{-2}$ Torr), (*7*) oscillograph, (*8*) computer.

1063-7850/00/2601-0049$20.00 © 2000 MAIK "Nauka/Interperiodica"

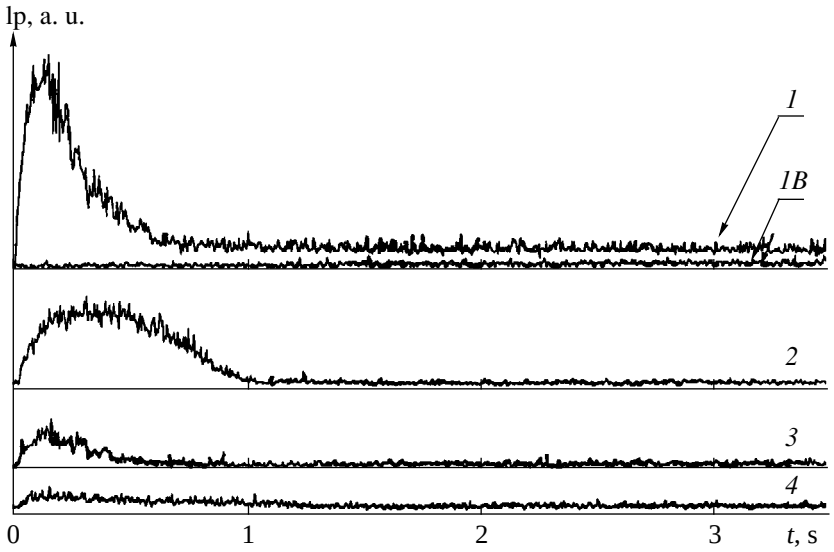

Fig. 2. The variation of scattering of sampling bean of a He–Ne laser on the silicon surface under the effect of successive single pulses of a YAG:Nd laser ($I = 2.5 \times 10^6$ W cm^2): (*1–4*) number of pulses (air), (*1B*) scattering of sampling beam upon irradiation in vacuum $P \approx 10^{-2}$ Torr.

of the scattering signal is shifted relative to the YAG:Nd laser pulse. Subsequent irradiation of the same surface region leads to a rapid decrease of the scattering signal amplitude. The scattered radiation intensity drops rapidly with the pressure in the vacuum chamber and, at $P \approx 10^{-1}$ Torr, the signal almost fully disappears.

The increase in scattering points to a variation in the surface relief (originally flat and mirror smooth) as a result of the effect of the YAG:Nd laser pulse. The variation of the surface relief may be caused mainly by thermal deformation, generation of significant concentration of structural defects in the surface layer, and surface oxidation. The thermal deformation is due to the surface layer heating, and because the surface temperature drops rapidly after termination of the laser pulse, the thermal deformation must disappear as rapidly. Therefore, the existence of scattering signal of such a long duration may hardly be attributed to thermal deformation of the surface. Apparently, the variation of the surface relief associated with the generation of defects and their subsequent slow recombination may neither be taken to cause the existence of the scattering signal for the same reason that the surface temperature drops rapidly and the defect recombination ceases (the remaining defects are quenched in the sample). The most likely reason for the existence of scattering signal may be the oxidation of the surface layer enriched with defects. In so doing, it appears to us that the existence of an increased concentration of defects in the surface layer is a condition of fundamental importance, which may lead to a considerable decrease in the migration energy of oxygen and, as a result, activate its diffusion in the cooled surface layer. This results in an increased duration of variation of the surface relief, associated with the oxidation of the surface layer, which is probably observed in the experiment. This assumption is further favored by the absence of scattering signal in vacuum and by the decrease of the scattering signal amplitude in the case of repeated irradiation of one and the same surface region in air.

Indeed, no oxidation of the surface layer occurs in the former case and, therefore, no surface relief variation is observed, while in the latter case one observes the saturation of the surface layer with oxygen, which results in a decreasing variation of the surface relief during subsequent irradiation pulses.

REFERENCES

1. V. P. Veĭko and S. M. Metev, *Laser Technologies in Microelectronics* (Bulgarian Acad. Sci., Sofia, 1991).
2. A. A. Vedenov and G. G. Gladush, *Physical Processes in Laser Treatment of Materials* (Énergoatomizdat, Moscow, 1985).
3. D. Bauerle, *Laser Processing and Chemistry* (Springer, New York, 1996).
4. S. Yu. Karpov, Yu. V. Koval'chuk, and Yu. V. Pogorel'skiĭ, Itogi Nauki Tekh. Fiz. Osnovy Lazern. Puchk. Tekhnol. **1**, 5 (1988).
5. V. I. Boĭko, Yu. S. Luk'yanchuk, and E. R. Tsarev, Tr. Inst. Obshch. Fiz. Akad. Nauk SSSR **30**, 6 (1991).
6. J. Lauzeral, D. Walgraef, and N. M. Ghoniem, Phys. Rev. Lett. **79** (14), 2706 (1997).
7. B. L. Volodin, V. I. Emel'yanov, and Yu. G. Shlykov, Kvantovaya Élektron. **20**, 57 (1993).
8. A. F. Banishev, V. I. Emel'yanov, and M. M. Novikov, Laser Phys. **2** (2), 178 (1992).
9. V. P. Veĭko, Ya. A. Imas, M. N. Libenson, *et al.*, Izv. Akad. Nauk SSSR Ser. Fiz. **49**, 1236 (1985).

Translated by H. Bronsteĭn

Technical Physics Letters, Vol. 26, No. 1, 2000, pp. 51–53. Translated from Pis'ma v Zhurnal Tekhnicheskoĭ Fiziki, Vol. 26, No. 2, 2000, pp. 13–18.

The Effect of Elastic Energy Accumulation and the Possibility of Controlling the Fracture Process in Complex Structures

S. G. Psakhie[1)], A. Yu. Smolin[1)], E. M. Tatarintsev[2)], and E. A. Shvab[2)]

[1)]*Institute of Strength Physics and Materials Science, Siberian Division, Russian Academy of Sciences, Tomsk, 634055 Russia*

[2)]*Tomsk State University, Tomsk, 634050 Russia*

Received July 29, 1999

Abstract—The behavior and fracture of complex structures under dynamic loading conditions were studied by computer simulation using the method of mobile cell automats. Possibility of the effect of elastic energy accumulation is demonstrated. The character of fracture in the systems studied can be considerably modified by very slightly changing initial geometry of the structure. © *2000 MAIK "Nauka/Interperiodica".*

INTRODUCTION

One of the major problems in modern technology is to provide for an increase in the viability of constructions serving under dynamic loading conditions. A well-known example is solving the task of ensuring the safety of passengers in cars and other vehicles in the case of collisions. In the general case, the solution consists in providing conditions for a controlled transfer of the kinetic energy of interaction (impact) into the energy of fracture liberated in less important parts and units of construction. It should be noted that an analogous problem is encountered in the materials science, since most of the modern construction materials are heterogeneous and possess complex internal structures. In optimizing the structure of a material intended for use under the dynamic loading conditions, it is necessary to take into account a possibility that redistribution of the elastic energy (related, e.g., to phase transitions, generation and accumulation of microscopic damage, etc.) would change the mechanical properties of the material in the course of loading [1–4].

Since real experiments involving the fracture of complex objects (e.g., crash tests) are rather expensive and the extraction of detailed information from the results of these experiments is usually a very difficult task, these problems are now frequently solved by methods of computer simulation. As a rule, the simulations are based on the methods of continuum mechanics. These methods provided a considerable progress in the fracture mechanics. Nevertheless, the continuum mechanics approach has certain restrictions related for the most part to the possibility of describing the production of damage and the formation and propagation of cracks. Problems of these kinds can be solved based on the method of mobile cell automats extensively developed in recent years. This method was successfully used in simulations of the fracture of various materials and constructions [4–8].

The purpose of this work was to study the possibility of controlled elastic energy "pumping" in the course of dynamic loading of complex structures. For correctly solving this task, it is necessary to thoroughly follow the behavior of a system, from appearance of the first damage to complete fracture of the construction simulated. For this reason, we have performed simulations using the method of mobile cell automats.

SIMULATION MODEL

Within the framework of the method employed, the material studied was represented by an ensemble of elements (cell automates) interacting with each other according to certain rules. In our model, in contrast to the classical method of cell automats [9, 10], the elements are allowed to move in space under the action of interactions between automats as well as external forces. Both translational and rotational motions are taken into consideration. The mechanical interactions are measured in terms of the automat overlapping and relative rotation [8]. In addition, each pair of elements is considered as a bistable automat characterized by the state of connection or disconnection, the transition from the former state to the latter representing an elementary fracture event. The equations of motion for the mobile cell automats derived within the framework of the Vinner–Rosenblut model represent a variant of the Newton equations for an ensemble of particles with an allowance for the multiparticle interactions [8].

This approach, by virtue of the mobility of individual elements, allows various processes occurring in real materials under loading to be simulated, including the mutual penetration and mixing of masses, generation

1063-7850/00/2601-0051$20.00 © 2000 MAIK "Nauka/Interperiodica"

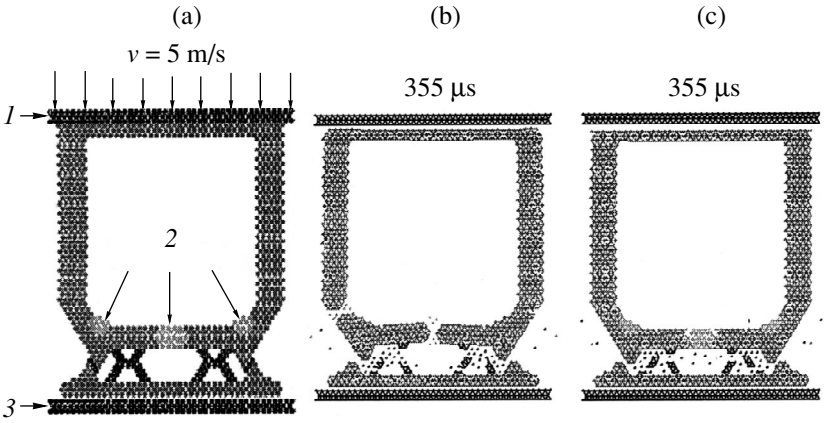

Fig. 1. Schematic diagrams (a) of the base model construction and the patterns of fracture in the frame (b) with and (c) without damping inserts at the time moment $t = 355$ μs: (*1*) piston; (*2*) damping inserts; (*3*) immobile obstacle.

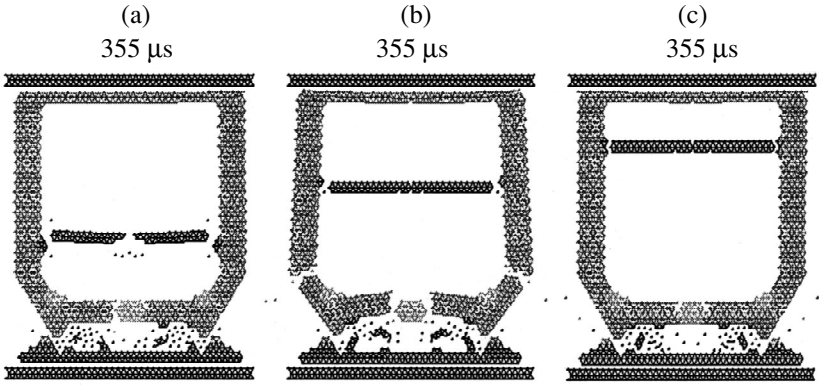

Fig. 2. Patterns of fracture in the frame structure with horizontal crosspiece in various positions at the time moment $t = 355$ μs.

and development of damage, and the formation of cracks. By setting special boundary conditions [5, 8], one may also simulate various regimes of loading, including compression, stretching, shear strain, etc.

In this work, we have simulated the loading of flat samples with a shape resembling construction of the front part of a car frame. The mechanical characteristics of a material studied corresponded to those of a ZrO_2 ceramics, for which the parameters of mobile cell automats are well determined [4, 8]. The sample, composed of the 0.1-cm automats, had a total width of 4 cm and a height of 5 cm. The sample shape and the loading mode are illustrated in Fig. 1a. The loading was effected by pushing the sample with a "piston" moving at a velocity of 5 m/s, so that the front of the construction collided with an immobile obstacle. Parameters of the obstacle automats corresponded to the mechanical properties of concrete.

RESULTS AND DISCUSSION

Multiply repeated experiments on the simulation of "collisions" showed that maximum local displacements are observed for elements at the center and corners of the front wall of the sample construction. In order to provide for a more uniform distribution of the energy "pumped into" the sample structure, we have introduced special damping inserts into these regions, made of a material with an elastic modulus equal to half of that for the base construction material. Figures 1b and 1c show the patterns of interautomat connections in the fractured samples with and without damping inserts, respectively, at the time instant $t = 355$ μs. As seen, the frame without inserts loses its carrying capacity, while the frame with inserts exhibits only insignificant damage.

An analysis of the simulation results showed that the presence of damping inserts in loaded samples leads to dynamic "accumulation" of the mechanical energy of collision. This effect is explained by the fact that, as indicated above, the regions of inserts are subject to maximum displacements in the course of loading. The inserts, because of their higher pliability, transfer the loading momentum along the sample rather than break, which leads to smearing of the stress concentrators and favors retaining of the structural integrity. This effect

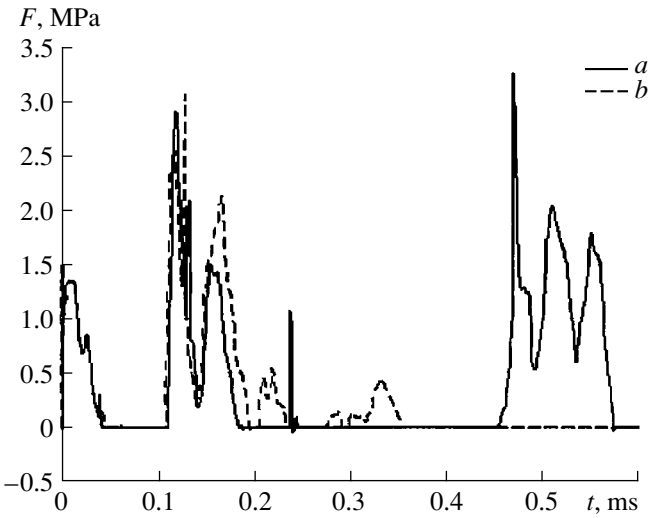

Fig. 3. Time variation of the response force acting upon the "piston" for the frame structures with crosspiece in different positions (curves *a* and *b* correspond to variants of the same notation in Fig. 2).

results in a significant increase of the threshold value of the energy that can be "pumped into" the structure, that is, of the energy that is absorbed in the sample until it would lose the carrying capacity. In fact, the elastic energy is "circulating" over the structure unless a stress concentrator would form with a power sufficient for the formation of a macrocrack.

In order to assess the possibility of controlling the variation of the pumped energy threshold by changing the structure geometry, we have studied a structure with a thin crosspiece in the internal region of the frame. The position of this crosspiece could be varied (Fig. 2). It must be noted that, irrespective of its position, the crosspiece was broken by a time instant of $t = 120$ μs. However, each structure with crosspiece exhibited a characteristic redistribution of the elastic energy flux in the system. In particular, the presence of the crosspiece led to the formation of a special "contour" featuring circulation of the elastic energy. This energy being liberated upon breakage of the crosspiece, each sample exhibited a particular dynamics of the formation and development of stress concentrators and, hence, was characterized by its own fracture history.

These results indicate that the response of a complex structure on the dynamic loading (Fig. 3) and the threshold value of energy "pumped into" the structure are not fully determined by general configuration (geometry) of the structure. For example, displacement of the crosspiece from back to the middle and closer to the front of the frame led to a significant decrease in the pumped energy threshold and altered the general pattern of fracture.

Thus, the results of our simulations clearly demonstrated the principal possibility of controlling the fracture process and increasing the viability of structures, which can be achieved both by slightly modifying their geometry and using special inserts.

REFERENCES

1. V. E. Panin, Fiz. Mekh. **1** (1), 5 (1998).
2. E. Haug, J. Clinckemaillie, X. Ni, A. K. Pickett, and T. Queckbarner, in *International Crashworthiess and Design Symposium* (ICD-95, 3–4 May 1995) (University of Valencia, Valencia, 1995).
3. G. Lonsdale, J. Clinckemaillie, S. Vlachoutsis, and J. Dubois, in *Lecture Notes in Computer Science* (Springer-Verlag, 1994), p. 55.
4. S. G. Psakhie, D. D. Moiseenko, A. I. Dmitriev, E. V. Shil'ko, S. Yu. Korostelev, A. Yu. Smolin, E. E. Deryugin, and S. N. Kul'kov, Pis'ma Zh. Tekh. Fiz. **24** (4), 71 (1998).
5. S. G. Psakhie, Ya. Khori, S. Yu. Korostelev, A. Yu. Smolin, A. I. Dmitriev, E. V. Shil'ko, and S. V. Alekseev, Izv. Vyssh. Uchebn. Zaved., Fiz. **38** (11), 58 (1995).
6. S. G. Psakhie, E. V. Shil'ko, A. I. Dmitriev, S. Yu. Korostelev, A. Yu. Smolin, and E. N. Korosteleva, Pis'ma Zh. Tekh. Fiz. **22** (12), 69 (1996).
7. S. G. Psakhie, A. Yu. Smolin, E. V. Shil'ko, S. Yu. Korostelev, A. I. Dmitriev, and S. V. Alekseev, J. Mater. Sci. Technol. **13** (11), 69 (1997).
8. S. G. Psakhie, S. Yu. Korostelev, A. Yu. Smolin, A. I. Dmitriev, E. V. Shil'ko, D. D. Moiseenko, E. M. Tatarintsev, and S. V. Alekseev, Fiz. Mezomekh. **1** (1), 95 (1998).
9. S. Wolfram, Rev. Mod. Phys. **55**, 601 (1983).
10. A. Yu. Loskutov and A. S. Mikhaĭlov, *Introduction to Synergetics* [in Russian] (Nauka, Moscow, 1990).

Translated by P.P. Pozdeev

Technical Physics Letters, Vol. 26, No. 1, 2000, pp. 54–55. Translated from Pis'ma v Zhurnal Tekhnicheskoĭ Fiziki, Vol. 26, No. 2, 2000, pp. 19–22.

p-GaSe-*n*-Recrystallized InSe Heterojunctions

V. N. Katerinchuk, Z. D. Kovalyuk, and V. M. Kaminskiĭ

Institute of Problems of Materials Studies,
National Academy of Sciences of Ukraine, Chernovtsy, Ukraine

Received June 16, 1999

Abstract—The photoelectric properties are investigated of heterojunctions (HJ) manufactured by recrystallization of InSe on a GaSe substrate. Substantial narrowing of the band is observed In spectra of photoresponse of HJ as compared with the photoresponse of the *p*-GaSe-*n*-InSe HJ obtained without recrystallization of InSe, which is caused by the formation of a solid solution of $In_{0.8}Ga_{0.2}Se$. An analysis of the temperature dependences of the current-voltage characteristics of obtained HJs reveals that the mechanism of current flow through a potential barrier exhibits a tunneling-recombination behavior. *© 2000 MAIK "Nauka/Interperiodica".*

Numerous authors [1–3] point out the high perfection and inertness of substrates of laminated materials, which are due to singularities of their crystalline structure. Some of these authors suggested the use of substrates with van der Waals bonds of the layers (as laminar crystals may be also called) for building up other laminated materials. In so doing, conclusions were made about the adequate degree of perfection of built up layers [4]. It is of interest to treat the processes occurring at the boundary of such heterosystems of laminar crystals. In this study, we used *p*-GaSe and *n*-InSe as the semiconductor pair in forming HJs.

The HJs were prepared by recrystallization of indium selenide on the surface of a higher temperature gallium selenide using the procedure of [5]. For this purpose, the samples were placed in evacuated quartz ampoules. The recrystallization process was carried out in the temperature range of 660–680°C. The contacts for samples were formed by fusing-in pure indium. All of the HJ samples were characterized by the presence of current rectification and by photosensitivity.

The recrystallized material was analyzed for monocrystallinity. A DRON-UM-1 facility was used for the purpose in a double-crystal spectrometer circuit using Cu-K_α-radiation. Various 00*l* reflections (l = 3, 6, 9, …) in the region of diffraction angles of initial InSe were obtained from the surface recrystallized layer. It follows from the epigrams previously taken in Cu-radiation that the layer being investigated has a monocrystalline structure.

Bond's method was used to measure the diffraction angles of 0012 reflection which enabled one to determine the lattice period from recrystallized layer, 24.748 Å. Initial InSe has c = 24.955 Å. The obtained difference may be observed in the case of formation of a solid solution of $In_{1-x}Ga_xSe$. In Vegard's law approximation, $c_x = c_{InSe} - (c_{InSe} - c_{GaSe})x$, the value of x = 0.2 was found. The formation of $In_{0.8}Ga_{0.2}Se$ is supported below by the results of measurements of the spectra of photoresponse of a large number of HJ samples.

Figure 1 gives the spectrum of photoresponse of the formed HJ and of HJ prepared by the method of optical contact of superconductors [6]. Comparison reveals that the formed recrystallized phase no longer corresponds to initial InSe. The shift of the long-wave edge of the photosensitivity band shown in Fig. 1 is approximately 0.15 eV and is caused by the formation of solid solution of $In_{0.8}Ga_{0.2}Se$. For samples prepared under different conditions of HJ formation, this shift varies between 0.1 and 0.2 eV. The band behavior is likewise subjected to changes. HJs prepared by the method of optical contact are characterized by the rise of photoresponse with the photon energy. The rise in photosensitivity is caused by an increase of the coefficient of light absorption in InSe [7] and leads to better collection and

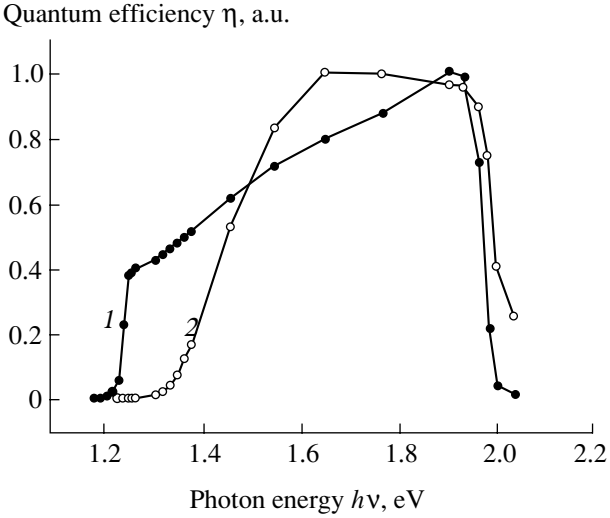

Fig. 1. Spectral dependences of the relative quantum efficiency of (*1*) *p*-GaSe-*n*-InSe and (*2*) *p*-GaSe-*n*-recrystallized InSe heterojunctions at room temperature.

1063-7850/00/2601-0054$20.00 © 2000 MAIK "Nauka/Interperiodica"

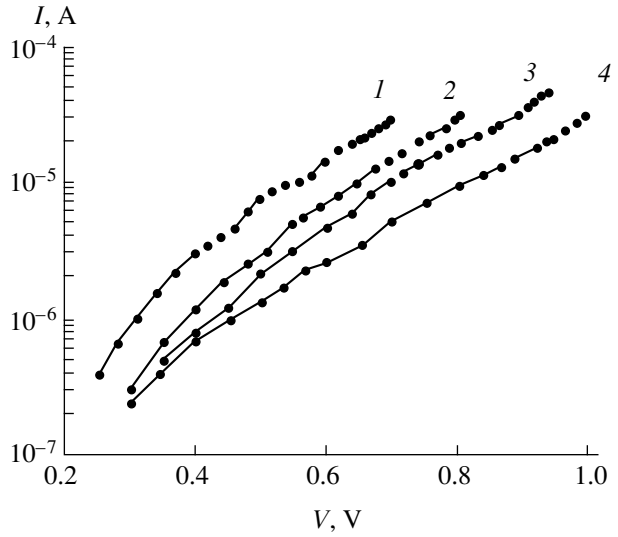

Fig. 2. Direct branches of the current-voltage characteristics of *p*-GaSe-*n*-recrystallized InSe heterojunction at different temperatures: (*1*) 300, (*2*) 270, (*3*) 240, and (*4*) 210 K.

separation of generated photocarriers on the HJ barrier. In the case of recrystallized InSe, the quantum efficiency of the photocurrent does not depend on the photon energy, which is indicative of the weak variation of the absorption coefficient in this material. This situation may be observed in the case of prevailing absorption of light by the surface of the recrystallized phase of InSe. In order to verify the latter fact, the mechanism of current flow through an HJ barrier was investigated. For this purpose, direct branches of the current-voltage characteristic of HJ, given in Fig. 2, were measured at different temperatures. In semilog coordinates, the current-voltage characteristics given in the figure are linear and may be described by the relation $I = I_0\exp(AU)$, where A is the parameter independent of temperature [8]. One can clearly see in the figure an almost parallel shift of the characteristics. This situation is observed in the case of the tunneling-recombination mechanism of current flow through an HJ barrier [8].

Based on the conclusions made by Milnes and Feucht [8], one can estimate the variation of the surface recombination rate S by the variation of the magnitude of tunneling-recombination current. Compared with HJs prepared by the method of optical contact of semiconductors, the surface recombination increases by two orders of magnitude. In view of this, note also some decrease in the magnitude of no-load voltage of the investigated HJs upon illumination.

REFERENCES

1. R. H. Williams and A. J. McEvoy, J. Vac. Sci. Technol. **2**, 867 (1972).
2. R. H. Williams and A. J. McEvoy, Phys. Status Solidi A **12**, 277 (1972).
3. D. B. Anan'ina, V. L. Bakumenko, L. N. Kurbatov, and V. F. Chishko, Fiz. Tekh. Poluprovodn. **10**, 2373 (1976) [Sov. Phys. Semicond. **10**, 1405 (1976)].
4. O. Lang and A. Klein, J. Cryst. Growth **146**, 439 (1995).
5. I. V. Alekseev, Fiz. Tekh. Poluprovodn. **32**, 588 (1998) [Sov. Phys. Semicond. **32**, 526 (1998)].
6. V. L. Bakumenko and V. F. Chishko, Fiz. Tekh. Poluprovodn. **11**, 2000 (1977) [Sov. Phys. Semicond. **11**, 1171 (1977)].
7. Landolt-Börnsteĭn, *Numerical Data and Functional Relationships in Science and Technology. New Ser. Group III: Crystal and Solid State Physics*, Ed. by O. Madelung (Springer, Berlin, 1983), Vol. 17.
8. A. G. Milnes and D. L. Feucht, *Heterojunctions and Metal-Semiconductor Junctions* (Academic, New York, 1972; Mir, Moscow, 1975), Chap. 2, p. 65.

Translated by H. Bronsteĭn

Technical Physics Letters, Vol. 26, No. 1, 2000, pp. 56–57. Translated from Pis'ma v Zhurnal Tekhnicheskoĭ Fiziki, Vol. 26, No. 2, 2000, pp. 23–27.

Dynamic Chaos in Recombination-Stimulated Atomic Processes

A. B. Avilov, B. A. Arapov, and B. L. Oksengendler

Osh State University, Osh, Kyrgyzstan

Institute of Nuclear Physics, Academy of Sciences of Uzbekistan, Tashkent, Uzbekistan

Received September 15, 1999

Abstract—The concept of dynamic chaos arising in a defect quasi-molecule is used for the first time for a systematic explanation of the discrepancy between theory and experiment in the field of recombination-stimulated reactions in semiconductors. © *2000 MAIK "Nauka/Interperiodica".*

Since the 1970s, it is known that charging of the defects and impurities related to deep energy levels in the forbidden band strongly influences the atomic rearrangements [1, 2]. This stimulation channel can be conveniently described within the framework of the Rice–Ramsperger–Kassel (RRK) approach [3], according to which the energy E_{ex} liberated during an electron transition is distributed between the vibrational degrees of freedom of a defect quasi-molecule (with $S = 3N$ degrees of freedom, where N is the number of atoms in the quasi-molecule). Then, vibrations of the S degrees of freedom interfere to excite a "reaction coordinate" describing the atomic rearrangement with an activation energy $E_{def} = E_d$.

In addition to the recombination-stimulated processes in semiconductors [1, 2], the RRK model has been successfully used to describe the dissociation of polyatomic molecules [3], the decomposition of vibrationally excited clusters [4], laser-induced photochemical processes [5], and even the decay of a compound nucleus [6, 7].

At the same time, the RRK approach leaves some questions open. For example [1, 2], the analysis of recombination-stimulated reactions in semiconductors has revealed that theoretical probability of this channel is always larger than the measured values:

$$W_{th} > W_{exp}.$$

Another challenge is conceptual and concerns the character of energy accumulation in a selected degree of freedom (reaction coordinate): does the process occur in a single step or by portions?

We believe that both difficulties can be removed by considering the process from the standpoint of the dynamic (deterministic) chaos concept [8].

The idea is as follows. Let a bound many-particle system (e.g., a quasi-molecule, cluster, or atomic nucleus) be excited in such a way that the excitation involves the majority (or all) of the degrees of freedom at the time instant $t = 0$. As is known [3], the probability that an energy E_d is accumulated in a given degree of freedom is

$$P = [1 - E_d/E_{ex}]^{S-1}, \quad (1)$$

where S is the total number of the degrees of freedom and E_{ex} is the initial excitation energy of the system.

Let us consider the energy accumulation in the given degree of freedom in more detail. It seems most realistic that the process goes step by step so that the amplitude of the vibration in this degree of freedom gradually increases. The larger the amplitude, the higher the probability that the excess energy would be transferred to other degrees of freedom to produce the randomization of states [8]. Furthermore, it is reasonable to expect that, provided E_{ex} is sufficiently large, the energy redistribution between vibrations in the selected and other degrees of freedom will become a systematically occurring event combining both deterministic and chaotic features. In other words, the molecule occurs in the state of deterministic chaos. It seems most appropriate to regard this state as intermittent, whereby the process of gradual energy accumulation in the given degree of freedom (laminar phase) alternate with the stage of randomization of the vibrations (turbulent phase), each phase of the two being characterized by its duration (Fig. 1). The durations of both laminar and turbulent phases exhibit random distributions with the probability density functions $P(t)$ and $\Omega(t)$, respectively.

Assume that the accumulation of energy E is possible only if the laminar phase duration exceeds a certain critical level t^* that can be expressed as

$$t^* = t_0[E_{ex}/(E_{ex} - E_d)]^{S-1}. \quad (2)$$

Here, t_0 is the average period of particle vibrations in the system. There are three possible types of intermittency, of which the process considered in this work (breakage of a given chemical bond in a polyatomic

quasi-molecule as a result of the superposition of vibrations with both positive and negative deviations of the bond from the equilibrium state) corresponds to type 3. According to [9], the distribution of the laminar phase durations is described by the function

$$P(t) = \exp 4\varepsilon t/(\exp 4\varepsilon t - 1)^{1.5}, \quad (3)$$

where ε is the parameter that indicates the degree of proximity of the given system to the bifurcation between purely deterministic behavior and the onset of chaos. In the case under consideration, ε must depend both on the degree of anharmonicity and on the level of excitation of the system. Consequently, the probability that a selected degree of freedom would accumulate the energy E_d before the onset of chaos is

$$\omega = \int_{t^*}^{\infty} p(t)dt \Big/ \int_{t_0}^{\infty} p(t)dt$$

$$= \frac{\exp\{-2\varepsilon t_0[E_{ex}/(E_{ex}-E_d)]^{S-1}\}}{\exp(-2\varepsilon t_0)} \quad (4)$$

$$\times\left[\frac{1-\exp(-4\varepsilon t_0)}{1-\exp[-4\varepsilon t_0(E_{ex}/(E_{ex}-E_d))]^{S-1}}\right]^{1/2}.$$

Note that ω is a function of all the energy parameters (E_{ex} and E_d) and of the number of the degrees of freedom S (Fig. 2).

Analogous probability expressions for the other types of intermittency can be derived similarly. They may be useful for the description of various physical systems different from polyatomic quasi-molecules.

Now, let us return to the problems of the RRK theory. Within the framework of the dynamic chaos concept, the probability of the process described by formula (1) can be written as

$$W = \omega[1 - E_d/E_{ex}]^{S-1}. \quad (5)$$

If the probability for a given degree of freedom to receive a necessary excitation energy E_{ex} is $R(E_{ex})$, then

$$\langle W\rangle = \int R(E_{ex})w(E_{ex})[1 - E_d/E_{ex}]^{S-1}dE_{ex}. \quad (6)$$

As for the problem of description of the fragmentation of defect clusters, one must also take into account the probability of the formation of clusters with various numbers of the degrees of freedom S. If the corresponding probability distribution function is φ(S), then

$$\langle\langle W\rangle\rangle = \iint R(E_{ex})\varphi(S)\omega(E_{ex}, S) \times [1 - E_d/E_{ex}]^{S-1}dE_{ex}dS. \quad (7)$$

Thus, it was established that nonlinear vibrations in a many-particle system with an excitation level sufficient for decomposition in at least one degree of freedom are characterized by a complicated instability state of the intermittency type. This phenomenon is a manifestation of the deterministic chaos effect. An adequate analysis of these effects allows decomposition of the system studied to be described within the framework of the RRK theory taking into account the character of the energy accumulation process. We believe that the strategy outlined above could find fairly wide application.

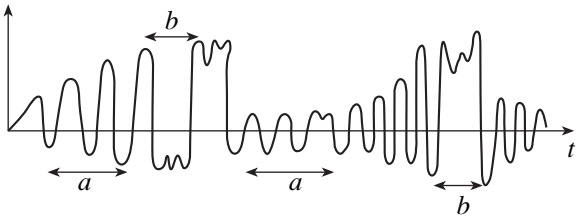

Fig. 1. Time variation of the reaction coordinate, including *a*—regular ("laminar") and *b*—stochastic ("turbulent") phases of motion.

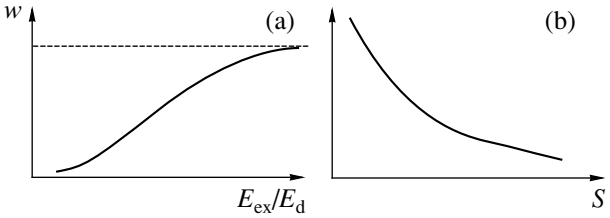

Fig. 2. Probability of attaining a critical reaction coordinate sufficient for the atomic rearrangement versus (a) the ratio of the excitation energy E_{ex} to the reaction threshold E_d and (b) the number of the degrees of freedom S.

REFERENCES

1. M. S. Yunusov, S. N. Abdurakhmanova, M. A. Zaĭkovskaya, *et al.*, *Subthreshold Radiation-induced Effects in Semiconductors* [in Russian] (Fan, Tashkent, 1989).
2. L. C. Kimerling, Solid State Electron. **21**, 1391 (1978).
3. P. J. Robinson and K. A. Holbrook, *Unimolecular Reactions* (Wiley-Interscience, London, 1972; Mir, Moscow, 1975).
4. N. Dzhelmley *et al.*, Int. J. Mass. Spectrom. Ion Processes **107**, 19 (1991).
5. A. H. Zewaĭl, Phys. Today **33** (11), 27 (1980).
6. N. Bohr, Nature **137**, 344 (1936).
7. A. Akhiezer and I. Pomeranchuk, *Aspects of the Theory of Atomic Nuclei* [in Russian] (Gostekhteorizdat, Moscow, 1948).
8. B. V. Chirikov, Phys. Rep. **52**, 463 (1979).
9. H. G. Schuster, *Deterministic Chaos—An Introduction* (Physik, Weinheim, 1984; Mir, Moscow, 1983).

Translated by A. A. Sharshakov

Technical Physics Letters, Vol. 26, No. 1, 2000, pp. 58–60. Translated from Pis'ma v Zhurnal Tekhnicheskoĭ Fiziki, Vol. 26, No. 2, 2000, pp. 28–34.

Swelling of Strongly Plastically Deformed Zinc during Its Annealing

G. A. Marinin, G. Ya. Akimov, and V. N. Varyukhin

Donetsk Physicotechnical Institute, National Academy of Sciences of Ukraine, Donetsk, Ukraine

Received February 1, 1999; in final form, August 6, 1999

Abstract—The effect of the annealing temperature on the density of a zinc wire (Zn 99.95%) obtained by the hydrostatic extrusion with the subsequent drawing has been studied in the range of 20–250°C. The total strain with respect to transverse reduction was $\lambda = 99.5\%$. It was revealed that annealing of plastically deformed zinc at 150° gives rise to swelling—an increase of the volume of strongly deformed zinc) and an accompanying decrease in its density. The swelling maximum (the density minimum) is observed in the vicinity of the temperatures 80–100°C. © *2000 MAIK "Nauka/Interperiodica".*

The phenomena of swelling and pore formation in structural metals and alloys operating in the elements of the active zones and the influence of internal stresses on the process of radiation-induced swelling have long been known [1]. It is also well known that deformation of metals and alloys provides an increase of the density of point defects and that the formation of microcracks and pores occurs already at the initial stage of deformation of crystalline solids [2, 3]. These facts give grounds to believe that swelling caused by pore formation in the specimens preliminarily subjected to considerable plastic deformations can also occur in nonirradiated metals and alloys during their subsequent annealing providing relaxation of internal stresses.

Below, we describe the study of zinc specimens whose physical and mechanical properties are of great practical and theoretical importance for understanding the nature of brittleness, plasticity, and superplasticity of solids. We had the aim to study the influence of a considerable plastic deformation of zinc specimens and their subsequent annealing on their density.

Cast zinc (Zn 99.95%) was deformed from the diameter of 36 to 6 mm by the method of the hydrostatic extrusion under a pressure of 1.0–1.2 GPa. Plasticity of the thus obtained zinc wire was increased by drawing it through a number of draw plates with the transverse reduction for one pass $\lambda = 5$–6%, which diminished its diameter from 6 to 2.5 mm. The total strain due to hydrostatic extrusion and drawing attained the value of $\lambda = 99.5\%$. After two-year storage of the thus obtained zinc wire, it was studied by the method of hydrostatic weighting (in distilled water at the temperature 20 ± 0.25°C) and on a VLR-200 analytical balance both in the initial state and upon annealing at the temperatures of 65, 105, 150, 200, and 250°C. Specimens were slowly (1°C/min) heated and kept for 10 minutes at each annealing temperatures and then were cooled in the furnace in the air atmosphere. After 24 h, the specimens were weighted and then annealed again at a higher temperature. The weighting accuracy in air was ±0.001 mN, the accuracy of weighting in the liquid was ±0.005 mN. The macroscopic zinc density was determined within an accuracy of ±0.002 g/cm^3. The results thus obtained are shown in Figs. 1 and 2.

Weighting of the specimens in air at room temperature (Fig. 1, curve *1*) showed that upon several stages of annealing in the temperature range 80–250°C, the zinc weight P_1 decreased the more, the higher the annealing

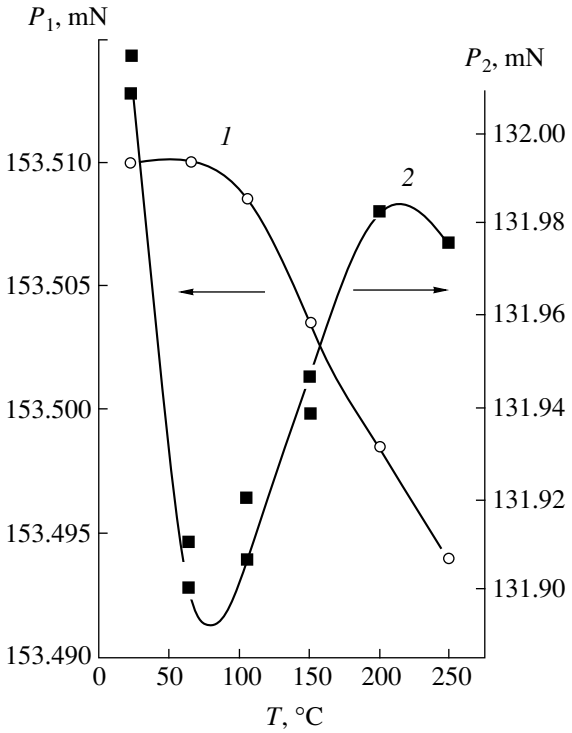

Fig. 1. Effect of temperature T on the weight of zinc wire in air P_1 (curve *1*) and in liquid P_2 (curve *2*).

1063-7850/00/2601-0058$20.00 © 2000 MAIK "Nauka/Interperiodica"

temperatures. This decrease in the zinc weight can be caused by the sublimation process, because the elasticity of zinc vapors equals $P \approx 1.3 \times 10^{-4}$ Pa at 180°C and $P = 1.3 \times 10^{-2}$ Pa at 250°C [4].

The weight P_2 of the specimen during the hydrostatic weighting varies in a complicated way (Fig. 1, curve *2*). At the annealing temperatures up to 100°C, the weight first decreases and then, at the annealing temperatures 100–200°C, increases. The maximum decrease of the zinc weight exceeds by an order of magnitude the error of weighting. The calculations showed that the change of the specimen weight in the liquid is associated with its swelling and a reduction of the macroscopic density (Fig. 2).

The data obtained indicate that zinc swelling attains the maximum value upon annealing at the temperatures T = 80–100°C. Annealing at higher temperatures results in a decrease of specimen swelling, which almost disappears upon annealing at 250°C. Annealing of the initial material in the temperature range 25–250°C showed no detectable density changes.

The measurements of the zinc-wire plasticity (at the extension rate 10 mm/min and the initial intergrip distance 100 mm; a PMU-0.05-1 tensile testing machine), the metallographic studies of the zinc microstructure, and the measurements of the grain size by the secant method with averaging of the results over at least 100 grains showed that the initial zinc wire had a finely granular structure with the grain size ranging within 10–50 μm. The grains were slightly elongated along the wire axis. The annealing at the temperatures up to 200°C resulted in no noticeable changes in the grain size, the specimen plasticity remained quite high at room temperatures, whereas the relative elongation of the wire prior to its rupture attained 30–37%. Upon annealing at 250°C, a fast increase of the grain size with the formation of a bamboolike single-crystal structure was observed, and the zinc wire became brittle.

Thus, zinc swelling and its subsequent decrease are observed in a material partly recrystallized in the process of its annealing. In this case, zinc preserves its high plasticity in the temperature range providing no considerable grain growth. A decrease in swelling is accompanied by a more intense zinc sublimation during heating. The intense recrystallization process observed at 250°C occurs only upon a decrease of swelling and provides growth of large grains.

It is well known that, at low deformation rates ($\dot{\varepsilon} < 10^{-3}$ s^{-1}), strengthening is provided by several factors, in particular, by the diffusion redistribution of point defects and microshear relaxation of local stresses [5]. In the process of conventional and superplastic deformation associated with incomplete material accommodation with respect to grain-boundary glide, one observes the pore formation, which affects the subsequent deformation [6, 7]. At the initial stage of deformation, cracks are formed mainly along the grain boundaries and their triple junctions [2]. The mechanism of "grain boundary pores" in superplastic alloys was considered elsewhere [8–10]. It was indicated that annealing of a superplastic Zn–22% Al alloy above 100°C increases the number of pores and, thus, also loosens the structure along the grain boundaries (by the mechanism of solution deposition) [8, 9].

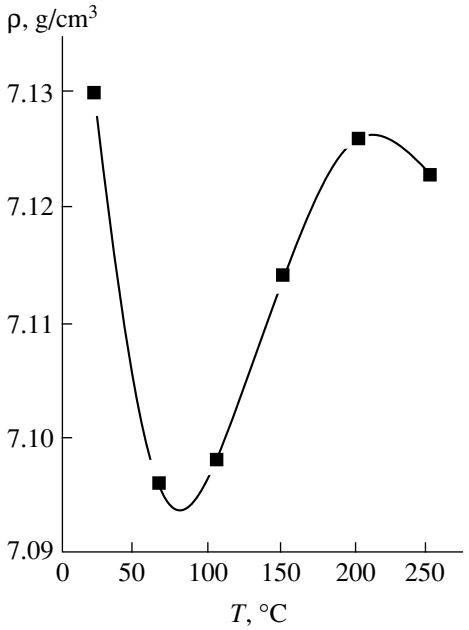

Fig. 2. Macroscopic density ρ of strongly deformed zinc upon its annealing at different temperatures.

In deformation under high pressures, the pore formation is hindered because of a reduced diffusion coefficient, which results in lower plasticity of the superplastic Zn–0.4% Al alloy (the so-called baroplastic effect [10]). The study of the baric dependences of the relative changes in the bulk of brittle and plastic zinc [11] showed the nonlinear character of the volume variation for brittle zinc in the vicinity of the pressure of the brittle plastic transition.

The phenomenon of swelling of strongly plastically deformed zinc during its annealing cannot be interpreted in terms of grain-boundary discontinuities formed by the mechanism of solution deposition as in the case of annealing of superplastic alloys [8, 9]. Strongly deformed pure zinc is not a superplastic material. Zinc swelling is observed only upon its heating up to 80–100°C, and therefore the most probable mechanism of pore growth is the formation of vacancies and their migration from the grain bulk into the pores. One of the possible causes of formation and growth of pores in polycrystal zinc is a pronounced anisotropy of its properties. Thus, in the temperature range 0–100°C, the linear expansion coefficient along the direction parallel to the main axis of a single crystal is four times higher than in the perpendicular direction [12]. It seems that

this can give rise to plastic deformation of grains in polycrystal zinc accompanied by pore formation and their subsequent growth at higher annealing temperatures.

A decrease of zinc swelling at temperatures exceeding 80–100°C can be explained by the fact that along with the processes providing the pore formation, another process also takes place—pore healing due to an increase of zinc-vapor elasticity during sublimation [4]. This also results in the reduction of the weight and the volume of the specimen during annealing. The calculations show that the change in the volume caused by sublimation is lower by an order of magnitude than the change in the volume determined from hydrostatic-weighting data. Therefore, the major contribution into an increase of the specimen density during annealing in the temperature range 100–200°C should come from healing of the inner pores, i.e., from a decrease of swelling. With a decrease of swelling, the decrease of the total grain-boundary length is observed only at temperatures above 200°C.

Thus, it can be assumed that along with the texture, the presence of impurities at grain boundaries, and the cellular dislocation structure (as in aluminum strongly deformed by extrusion [13]), the process of swelling (i.e., pore formation, including pores along grain boundaries) not only increases specimen plasticity, but also hinders the recrystallization process, which is seen from a drastic increase in grain growth with the formation of a bamboolike structure observed only upon the return to the initial volume and density values.

There are no doubt that further studies of swelling of strongly plastically deformed zinc observed during its annealing would be of great practical and theoretical importance.

ACKNOWLEDGMENTS

The authors are grateful to V.I. Barbashov for valuable discussion of the results obtained.

REFERENCES

1. V. S. Neustroev, Z. E. Ostrovskiĭ, and V. K. Shamardin, Fiz. Met. Metalloved. **86**, 115 (1998).
2. A. D. Vasil'ev, I. D. Gornaya, V. F. Moiseev, *et al.*, Metallofiz. **4** (2), 91 (1982).
3. A. Damask and G. Dienes, *Point Defects in Metals* (New York, 1963; Mir, Moscow, 1966).
4. *Handbook of a Chemist* (Khimicheskaya Literatura, Moscow, 1951).
5. I. A. Gindin and I. M. Neklyudov, *Physics of Programmed Strengthening* (Naukova Dumka, Kiev, 1979).
6. C. Zener, *Elasticity and Anelasticity of Metals* (Chicago, 1948); in *Elasticity and Anelasticity of Metals*, Ed. by Vonsovskiĭ (IL, Moscow, 1954).
7. M. M. J. Ahmed, F. A. Mohamed, and T. G. Zangdna, J. Mater. Sci. **14**, 2913 (1979).
8. R. I. Kuznetsova and O. A. Kaĭbyshev, Dokl. Akad. Nauk SSSR **257** (4), 863 (1981).
9. R. I. Kuznetsova and V. F. Korshak, Fiz. Met. Metalloved. **58** (5), 914.
10. I. I. Papirov, V. I. Zaĭtsev, G. Ya. Akimov, *et al.*, Dokl. Akad. Nauk SSSR **267** (2), 370 (1982).
11. V. N. Voryukhin, O. I. Datsko, and A. V. Reznikov, Fiz. Tverd. Tela, No. 14, 75 (1984).
12. *Handbook of a Metal-Worker* (Mashinostroenie, Moscow, 1965).
13. A. A. Galkin, O. I. Datsko, V. I. Zaĭtsev, *et al.*, Fiz. Met. Metalloved. **28** (1), 187 (1969).

Translated by L. Man

Technical Physics Letters, Vol. 26, No. 1, 2000, pp. 6–7. Translated from Pis'ma v Zhurnal Tekhnicheskoĭ Fiziki, Vol. 26, No. 1, 2000, pp. 13–16.

Hole Conduction in Zinc Selenide Crystals Doped with Elements of Group V from the Vapor Phase

V. P. Makhniĭ, M. M. Sletov, and Yu. Ya. Chaban

Chernovtsy State University, Chernovtsy, Ukraine

Received June 15, 1999

Abstract—The optical and electrical properties of zinc selenide crystals doped with elements of group V from the vapor phase are described. The possibility is demonstrated of obtaining *p*-type layers with an intense blue luminescence line. © *2000 MAIK "Nauka/Interperiodica".*

Zinc selenide is one of the most promising materials for developing injection blue light-emitting diodes [1]. At the same time, the production of crystals and layers of the *p*-type conductivity with predominantly marginal luminescence still remains an urgent problem. At present, fairly complex techniques are employed to solve this problem, such as the ionic [2], molecular-beam [3] or MOCVD [4] epitaxy, annealing in activated vapors of selenium [2], or a combination of several of these techniques. As distinct from the above-identified techniques, some accounts were made of the preparation of *p*-ZnSe layers by high-temperature diffusion of acceptor impurity of lithium from the liquid [5] or vapor [6] phase. In this paper, we describe the electrical and optical properties of zinc selenide crystals doped with elements of group V from the vapor phase.

Initial substrates were provided by specially undoped single crystals of ZnSe melt grown under an inert gas pressure. In the room temperature range, they exhibited a weak electron conduction of $\sim 10^{-12}\ \Omega^{-1}\ \mathrm{cm}^{-1}$. Doping was performed in quartz ampoules evacuated to 10^{-4} torr at a temperature of 1000–1200 K. The basic substrate and the weighed sample (elementary As, Sb, or Bi) were placed at different ends of the ampoule. The surface layers of annealed samples demonstrate the hole conduction, as indicated by the sign of thermal emf. The activation energy E_a of electrically active acceptor centers was found from the temperature dependences of resistance between two ohmic contacts prepared by the chemical deposition of copper. Note that these contacts on the initial substrates possess substantially nonlinear current-voltage characteristics. The photoluminescence (PL) was excited by an N_2 laser, and the radiation spectra were measured using an MDR-23 grating monochromator and a standard system of synchronous detection in the automatic recording mode. The same facility, with a vibrating mirror and xenon lamp instead of laser, was used to measure λ-modulated spectra of optical transmission and reflection.

The values of the depth of location of electrically active centers in the investigated samples are given in the table.

The values are averaged over the results of measurement of electrical conductivity, as well as of λ-modulated transmission spectra. The shallowest acceptor level ($E_a \approx 30$ meV) corresponds to interstitial selenium atoms Se_i [2] whose concentration increases as a result of substitution of Se in sites by elements of group V. Centers with $E_a \approx 180$–200 meV correlate with the depth of location of negative singly charged vacancies of zinc V'_{Zn} [2]. The levels with a depth of 110–130 meV correspond to impurity atoms of group V [7]. The highest hole conduction is observed in Sb-doped crystals, as indicated by the minimum value of thermal emf. Electrically active donor levels in the initial substrates are fairly deep and may be associated with interstitial atoms of zinc [2].

The spectrum of photoluminescence of initial crystals at 300 K is represented by the blue and orange lines with maxima $\hbar\omega$ at 2.68 and 1.98 eV, respectively (see figure). The edge line is characterized by the following singularities. First, the position of its maximum does not depend on the excitation level L. Second, the dependence of the intensity I_b on L is close to linear upon

Table

Impurity	As	Sb	Bi	Initial
r_a, Å	1.22	1.41	1.49	–
E_a, meV	30, 100, 200	30, 110, 180	30, 130, 190	600
Thermo emf, μV/K	45	20	50	–
I_b/I_o	0.3	20	45	50

1063-7850/00/2601-0006$20.00

variation of the excitation level within three orders of magnitude. And, finally, the difference $E_g - \hbar\omega + kT/2 = 2.7 - 2.68 + 0.013 = 0.033$ eV is close to the activation energy of the shallowest acceptor level Se_i. The orange line is associated with recombination on donor-acceptor pairs (DAP) whose composition includes negative doubly charged vacancies of zinc V''_{Zn} (acceptors) and positive singly charged vacancies of selenium $V^{\bullet}_{Se}$ (donors). In order to suppress the intensity I_o of the orange line, one must reduce the concentration of the vacancies $V^{\bullet}_{Se}$ which, in addition, compensate the hole conduction of ZnSe. This, in particular, may be attained by doping zinc selenide crystals with elements of group V. The latter enter the interstices of anion sublattice to fill V_{Se} and (or) displace Se to the interstices. In this case, the impurity atoms of the group exhibit the acceptor properties and lead to the emergence of hole conduction. Also contributing to an increase in the latter conduction is interstitial selenium, which is a shallow acceptor. The elements of group V fill the free sites of the anion sublattice to lead to a decrease in the V_{Se} vacancies entering the composition of DAP. This, in turn, leads to suppression of the orange line, which is observed in the experiment (see table and figure). The increase of the intensity of the blue line in doped crystals is due to an increase in the number of Se_i. It is logical to assume that their concentration in a first approximation will be defined by the atomic radius r_a of doping impurity, which increases during transition from As to Bi. This is illustrated by the table data.

Therefore, the foregoing results strongly suggest the possibility of producing *p*-type layers with predominantly blue luminescence by doping ZnSe crystals with elements of group V from the vapor phase.

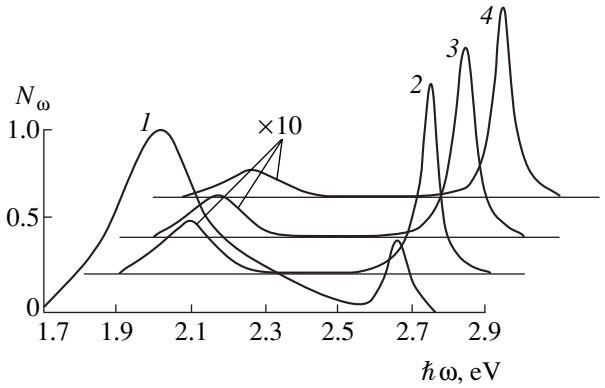

The photoluminescence of ZnSe crystals: (*1*) initial and doped (*2*) As, (*3*) Sb, and (*4*) Bi at 300 K.

REFERENCES

1. A. N. Georgobiani and M. B. Kotlyarevskiĭ, Izv. Akad. Nauk SSSR, Ser. Fiz. **49** (10), 1916 (1985).
2. *The Physics of A^2B^6 Compounds*, Ed. by A. N. Georgobiani and M. K. Sheinkman (Nauka, Moscow, 1986).
3. K. Akimoto, T. Miyajima, and Y. Mozi, Jpn. J. Appl. Phys. **28** (4), L531 (1989).
4. T. Yasuda, I. Mitsuishi, and H. Kukimoto, Appl. Phys. Lett. **52**, 57 (1988).
5. A. N. Krasnov, Yu. F. Vaksman, Yu. N. Purtov, and V. V. Serdyuk, Fiz. Tekh. Poluprovodn. **26** (6), 1151 (1992) [Sov. Phys. Semicond. **26** (6), 645 (1992)].
6. V. P. Makhniĭ, Opt. Spektrosk. **81**, 827 (1996) [Opt. Spectrosc. **81** (5), 756 (1996)].
7. R. N. Bhargava, J. Cryst. Growth **59**, 15 (1982).

Translated by H. Bronsteĭn

Technical Physics Letters, Vol. 26, No. 1, 2000, pp. 61–63. Translated from Pis'ma v Zhurnal Tekhnicheskoĭ Fiziki, Vol. 26, No. 2, 2000, pp. 35–40.

Investigation of Thin-Film Samples by the Method of Photothermal Reflection with Harmonic Excitation, Using the Heterodyning of Exciting and Sampling Radiation

K. V. Lapshin, A. N. Petrovskiĭ, V. V. Zuev, A. D. Kiryukhin, and D. V. Labuzov

Moscow Institute of Engineering Physics (Technical University), Moscow, Russia

Received June 7, 1999

Abstract—A method of determining the phase shift and thermal parameters of thin films is suggested and experimentally tested. © *2000 MAIK "Nauka/Interperiodica".*

The method of harmonic "mirage" effect is based on the phenomenon of harmonic variation of the refractive index of a sample under the effect of heat and electron (hole) waves caused by illumination of the sample by high-power exciting radiation. This variation of the sample refractive index may be recorded by transmitting low-power laser radiation through the sample and by using value of deviation of this radiation at the outlet from the sample to estimate the thermal (electron) response of the sample and thermal and electron parameters of the sample. The scanning beam oscillation frequency will be equal to the modulation frequency of exciting radiation with a phase shift defined by the thermal and electron response of the sample, by the thickness of sample layers (in the case of a multilayer sample), and by the modulation frequency of exciting radiation.

The harmonic "mirage" effect is widely employed industrially, in particular, for detection of hidden defects and noncontact monitoring of the thermal and electron parameters of thin films (especially those with high thermal conductivity and diffusivity whose measurements by contact methods cannot produce reliable results).

We suggest a new efficient method of determining the phase shift and thermal (electron) parameters of a sample which utilizes the beats of exciting and sampling radiation. The use of beats enables one to move the phase measurements from the range of hundreds and thousands of kilohertz to the kilohertz range in which the phase shift may be determined using standard low-frequency synchronous detectors commercially manufactured in Russia (we investigated thin films using a UPI-2 pulse amplifier-converter).

1. The block diagram of the setup employed in the experiment for investigation of thin films is given in Fig. 1.

The source of exciting radiation was provided in the experiment by an OGM-5M continuous argon laser *1* with a radiation wavelength $\lambda \cong 0.5$ μm, with the preassigned radiation power of 1 W during the experiment.

Exciting radiation was applied to an acoustooptic modulator *2* designed to special order for this experiment. Used as exciting radiation in the experiment is one of two first modes of modulated radiation (with the modulation frequency of radiation intensity equal to the frequency applied to the acoustooptic modulator), with the set value of radiation power in this mode being the maximum possible (the power was varied by changing the angle of entry of radiation into the crystal of the acoustooptic modulator). The first and zero modes employed in the experiment were cut out by a diaphragm *3*, which did not transmit the remaining modes (including the second first mode).

Unmodulated radiation (zero mode) was applied to a second acoustooptic modulator *4*, after which the first modulated mode (the minimum set value of radiation power, with the pumping of energy into the third mode), cut out by a diaphragm *5* and attenuated by a system of light filters *6*, was used as sampling radiation. The power of sampling radiation was more than an order of magnitude less than that of exciting radiation, which made it possible to ignore the effect of sampling radiation on the formation of thermal response in the sample.

The values of modulation frequency of acoustooptic modulators were preassigned from G4-143 high-frequency generators *7* and *8*. The modulation of exciting and sampling radiation ω_1 and ω_2, respectively, was preassigned by way of modulation of high-frequency signals from the G4-143 generators with low frequencies (differing by several percent in magnitude) delivered from G6-28 generators *9* and *10* of signals of special shape. Signals from the synchronization inputs of two G6-28 generators were applied to an adder *11*; a Ch3-54 counting-type frequency meter *12* was used to read their beat equal to the difference between the modulation frequencies of sampling and exciting

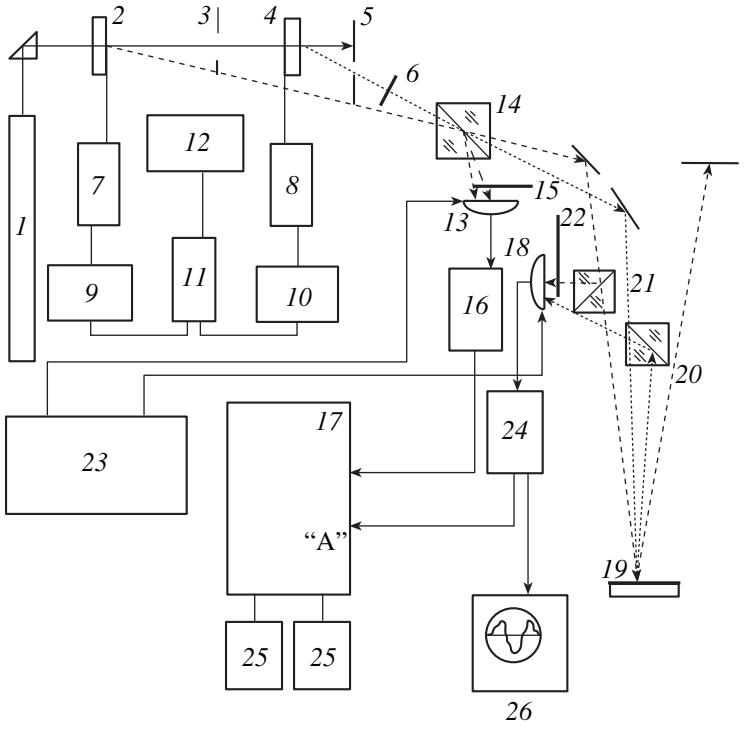

Fig. 1. Block diagram of the experimental setup.

radiation and maintained at 5 kHz throughout the experiment.

The reference signal was preassigned by reading the beat between sampling and exciting radiation applied to an FD-24K photodiode *13* after reflection of a part of sampling and exciting radiation by a dividing cube *14*. The power of the part of exciting radiation incident on the photodiode was attenuated by a light filter *15* and was comparable with the power of the part of sampling radiation incident on the photodiode, so that the total power P_1 was

$$P_1 \sim I_1(t) \sim 2 + \cos\omega_1 t + \cos\omega_2(t) \cong 2 + 2\cos\omega_1 t\cos(\Delta\omega t/2) \quad (1)$$

at $\Delta\omega = \omega_1 - \omega_2 \ll \omega_1, \omega_2$.

With the photodiode response time τ being less than the period of oscillation of intensity $T = 2\pi/\omega_1$, the electric signal from the photodiode repeats the time variation of intensity I. This signal from the photodiode *13* was delivered to a specially designed operational amplifier *16* with an appropriate transmission band, from which the signal was applied to the reference input of a UPI-2 pulse amplifier-converter *17*. Here, the demodulation of the signal occurs as well as the isolation of the low-frequency component proportional to $\cos(\Delta\omega t/2)$, whose frequency was 2.5 kHz.

A second FD-24K photodiode *18* was subjected to sampling radiation reflected from a sample *19* separated by a dividing cube *20* from the radiation incident on the sample as well as to a part of exciting radiation diverted by a dividing cube *21* and attenuated by a light filter *22* to a power whose value is comparable with that of the power of sampling radiation incident on the photodiode. The sampling beam reflected from the sample will differ from that incident on the sample by some modulation frequency-dependent phase shift $\delta(\omega)$, which is due to the sample response. In this case, the power P_2 incident on the second FD-24K photodiode *18* may be given by

$$P_2 \sim I_2(t) \sim 2 + \cos\omega_1 t + \cos(\omega_2 t + \delta) \cong 2 + 2\cos(\omega_1 t + \delta/2)\cos(\Delta\omega t/2 + \delta/2). \quad (2)$$

For simplicity, we assumed in (1) and (2) that the possibilities of radiations incident on the photodiodes are the same. Under real experimental conditions, it is the values of the coefficients appearing in (1) and (2) that will change rather than the form of the frequency dependences.

The photodiodes *13* and *18* were supplied from a UNIP-7 two-channel dc supply source *23*.

The forming of useful signal was defined by the dependence of the reflectivity of the sample surface on the surface temperature which, in turn, depended on the thermal response of the sample to exciting radiation. Both exciting and sampling radiation hit a single point of the sample secured on a table with micron feed providing for adjustment within 10 μm. In order to reduce parasitic oscillation, the experimental setup was mounted on a sheet of foam plastic 10 cm thick.

A signal from a photodiode was delivered to an operational amplifier *24* and then to the input A of the UPI-2 pulse amplifier-converter *17*. The UPI-2 readings were taken from two Q channels of the amplifier to two V7-16A digital voltmeters *25*. The visual observation of signal beats was performed with the aid of an S1-67 monitoring oscillograph *26*.

2. The sample used in the experiment was a tungsten film 3 μm thick spray-coated onto a silicon substrate.

The graph of the signal phase as a function of the root of the signal modulation frequency, constructed during the experiment, is given in Fig. 2.

One can see from the graph that, with f_1 = 150 kHz, a kink is observed. From the physical standpoint, this may be explained by the fact that, during the period of variation of intensity $T_1 = 1/f_1$, there is enough time for thermal diffusion with the coefficient D_T to effectively proceed over the entire film thickness μ up to the second medium, i.e., silicon substrate, where the condition of transmission of thermal excitation changes at the interface. Therefore, the kink is characterized by the fact that the length of thermal diffusion over the period is equal in the order of magnitude to the silicon film thickness μ [1]:

$$\mu \approx (D_T/f_1)^{1/2}. \quad (3)$$

If we take the tabulated value of D_T for tungsten (0.6 cm^2/s) [2], expression (3) will yield the value of the film thickness of 20 μm, which is quite reasonable in view of the method of preparation of the film. Given the film thickness, one can use expression (3) to determine the thermal characteristic of the material D_T: a comparison of the value of this characteristic with the tabulated value enables one to estimate the quality of deposition of coating.

In this study, we performed investigations of thin films in low-frequency synchronous detectors using the effect of recording of low-frequency beats between modulated high frequencies with respect to intensity by sampling and exciting radiation and demonstrated the sphere of possible application of the suggested procedure. To our knowledge, this is the first ever publication on the subject. The paper further contains experimental results of measurements of the thermal diffusivity of a silicon sample.

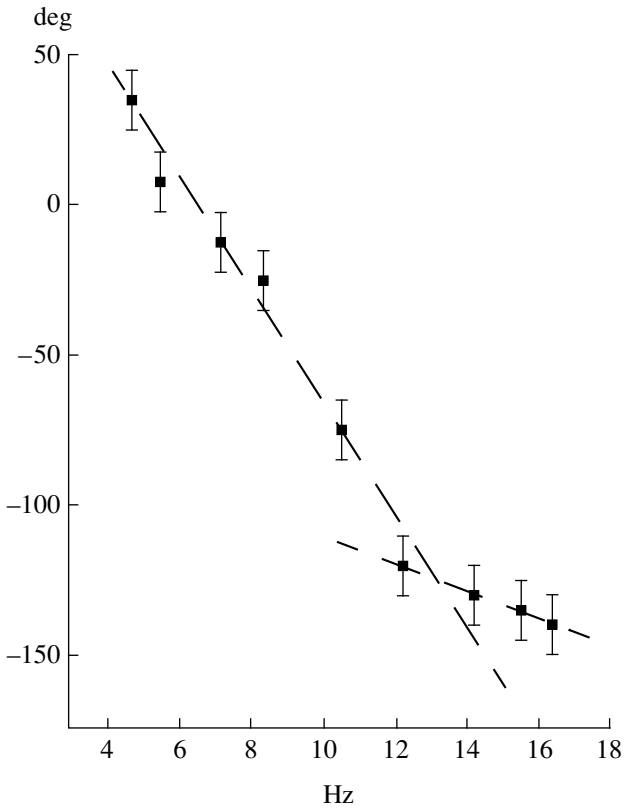

Fig. 2. The phase of photothermal signal as a function of the root of the modulation frequency of exciting radiation.

REFERENCES

1. V. V. Zuev, A. N. Petrovskiĭ, and A. O. Sal'nik, Preprint No. 046-87, MIFI (Moscow Inst. of Engineering Physics, 1987).
2. *Physical Encyclopedia*, Ed. by A. M. Prokhorov (Sovetskaya Éntsiklopediya, Moscow, 1988), Vol. 1.

Translated by H. Bronsteĭn

Technical Physics Letters, Vol. 26, No. 1, 2000, pp. 64–66. Translated from Pis'ma v Zhurnal Tekhnicheskoĭ Fiziki, Vol. 26, No. 2, 2000, pp. 41–46.

Mechanism for the Suppression of Lower Hybrid Current Drive in the FT-2 Tokamak

V. N. Budnikov, V. V. D'yachenko, P. R. Goncharov, V. B. Ermolaev, L. A. Esipov, E. R. Its, M. Yu. Kantor, D. V. Kuprienko, S. I. Lashkul, K. A. Podushnikova, I. E. Sakharov†, E. O. Chechik, and S. V. Shatalin

Ioffe Institute for Physics and Technology, Russian Academy of Sciences, Politekhnicheskaya ul. 26, St. Petersburg, 194021 Russia

St. Petersburg State Technical University, Politekhnicheskaya ul. 29, St. Petersburg, 195251 Russia

Received September 27, 1999

Abstract—The mechanism for the switching off of the lower hybrid current drive in the FT-2 tokamak is studied. It is shown that the lower hybrid wave-driven current is switched off when a parametric instability, which causes lower hybrid waves to decay into slowed waves interacting with plasma ions, develops at the plasma periphery. The onset of a parametric instability is attributed to the fact that the electron temperature falls off in the course of discharge, thereby lowering the instability threshold. *© 2000 MAIK "Nauka/Interperiodica".*

It is well known that lower hybrid (LH) current drive in tokamaks terminates at plasma densities significantly below the density corresponding to the LH resonance. According to [1, 2], this effect is caused by a parametric decay of LH waves into slowed waves, which interact with plasma ions more efficiently than with plasma electrons. Here, we present the experimental results from the FT-2 tokamak that support this hypothesis.

The main parameters of the FT-2 device and of the Ohmic discharges in FT-2 are as follows: R = 55 cm, a = 8 cm, B_T = 2.2 T, I_P = 20 kA, $T_{e\mathrm{OH}}$ = 400 eV, $T_{i\mathrm{OH}}$ = 90 eV, and Z_{eff} = 3. A 100-kW 920-MHz RF pulse was launched by a double-waveguide grill with a longitudinal refractive index $N_\parallel \sim 2.5$. The plasma density corresponding to a linear transformation of the launched LH wave was 3.5×10^{13} cm^{-3}. In order for the current that is generated just at the beginning of the RF pulse to be switched off before the pulse has come to an end, the central plasma density was chosen to be 2×10^{13} cm^{-3}.

During the RF pulse, the discharge was observed to evolve from one regime to another. A drop in the plasma loop voltage (Fig. 1a) presents direct evidence for LH current drive in the initial stage of the microwave pulse. As the loop voltage rises, the plasma ions are strongly heated and the plasma density increases, which points to the LH ion heating regime.

Throughout the current drive stage, the plasma density and ion temperature change only slightly (Figs. 1b, 1c), while the electron temperature falls off significantly (Fig. 1d), because the ohmic power P_E, which is determined by the power balance relation

$$P_E = I_P U_{\mathrm{loop}} - \frac{d(LI_P^2/2)}{dt}$$

decreases during the RF pulse. In (1), $L = 4\pi R\left(\ln\frac{b}{a} + \frac{l_i}{2}\right)$ is the inductance of the plasma column and b is the radius of the loop measuring the plasma loop voltage. The change in the internal inductance l_i of the plasma column (Fig. 1e) was measured by ploidal magnetic probes, which determined the value of the quantity $\beta_j + l_i/2$. The time evolution of β_j (Fig. 1f) was computed from the measured radial profiles of the electron and ion temperatures and plasma density shown in Fig. 2.

Rapid changes in P_E (Fig. 1g) at the times at which the RF pulse is switched on and off indicate a significant redistribution of the plasma current at those times. The LH-driven current inferred from these changes amounts to 70% of the total plasma current at the instant at which the pulse is switched on and to 45% of the total current in the ion heating stage. One of the main reasons why the electron temperature remains low until the end of the microwave pulse is a small fraction of Ohmic current throughout the heating stage. Another reason may be enhanced heat losses due to strong turbulence, which develops after the plasma has evolved to this stage [3].

A wave launched by a grill with a refractive index of about $N_\parallel \sim 2$–3 is not subject to the LH resonance in the plasma and interacts exclusively with runaway elec-

† Deceased.

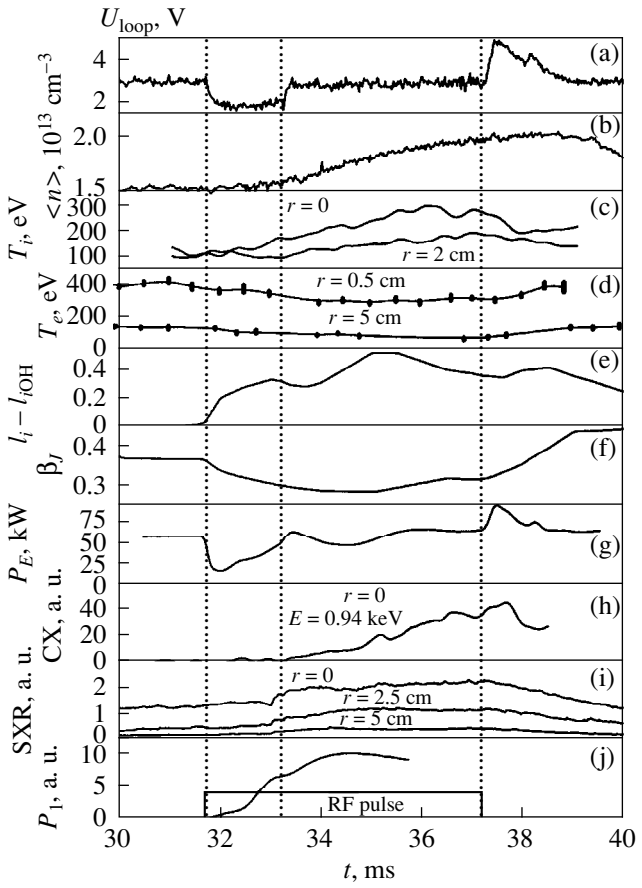

Fig. 1. Time evolutions of the plasma parameters during the RF pulse: (a) loop voltage, (b) electron density, (c) ion temperature, (d) electron temperature, (e) internal inductance of the plasma column, (f) the quantity β_j, (g) Ohmic power, (h) the flux of charge-exchange atoms with an energy of 0.94 keV, (i) the fluxes of soft X radiation, and (j) the amplitude of the first satellite.

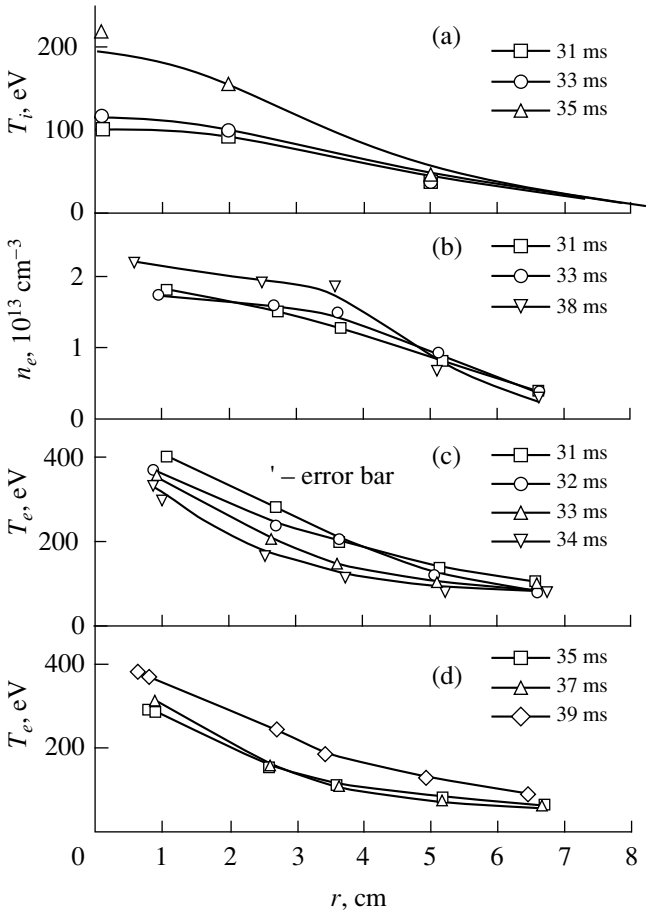

Fig. 2. Time evolutions of (a) the plasma density, (b) the ion temperature, and (c, d) the electron temperature during the RF pulse.

trons with energies of 25–50 keV, thereby generating a toroidal plasma current. In the ion heating regime, new mechanisms for the absorption of LH power come into play, specifically, interactions of LH waves with plasma ions and electrons of lower energy. This is evidenced by the following experimental facts.

The dominant effect is strong plasma heating in the central region (Fig. 1d), where the excitation of LH waves with a transverse refractive index $N_\perp = c/v_i \sim 600$ is evidenced by an increase in the flux of charge-exchange atoms with an energy of 1 keV (Fig. 1h). Waves with such a high refractive index ($N_\perp \sim c/3v_{Ti}$) should be completely absorbed by the ions [4]. An analysis of the ion energy balance shows that, after the current drive terminates, the ions absorb up to 6 kW of the input RF power.

From the dispersion relation for LH waves, we can estimate the longitudinal refractive index of the waves interacting with ions as $N_\parallel \sim 10$. Such waves interact with electrons with energies above 2 keV via the Landau mechanism. As a result, in this energy range, the electron density increases, which is confirmed by a rapid growth of the intensity of soft X radiation from the discharge center (Fig. 1i) just before the current drive comes to an end. A measurement of the X-ray spectrum by the method of foils showed that the electron density rises in the energy range 2–10 keV.

Slowed waves can arise due to the parametric decay of an LH wave launched into the plasma [1]. In our experiments, the decay process was monitored by a five-electrode Langmuir probe [5], which was placed in the limiter shadow and functioned as a microwave antenna. When a microwave pulse was switched on, two peaks appeared in the microwave fluctuation spectrum, one of which occurred at a pump frequency of 920 MHz and the other was shifted toward the low-frequency range by 30 MHz [6]. The amplitude of the central peak did not change during the pulse, while the amplitude of the satellite increased by about one order of magnitude (Fig. 1j). The fact that no blue satellite was observed in the fluctuation spectrum points to the

parametric decay of an LH wave. The frequency shift of the red satellite corresponds to the ion cyclotron frequency at a radial distance of 7 cm from the discharge center on the side of the weaker magnetic field. We think that, in this region, the injected LH wave with frequency f_0 decays parametrically into daughter waves with frequency $f_0 - f_{ci}$ and with a higher refractive index; these interact less intensively with the runaway electrons carrying plasma current during the RF pulse. From Fig. 1j, we can see that the parametric instability develops before the phenomena described above come into play. The injected LH wave starts to decay, because, during LH current drive, the electron temperature falls off, thereby lowering the threshold $P_{thr} \sim T_e/n_e$ for the onset of a parametric instability [7].

Hence, the termination of LH current drive in the FT-2 tokamak may be attributed to a decrease in electron temperature, as a result of which the threshold for the onset of parametric instabilities is lowered and LH waves start to decay. The slowed-down decaying daughter waves begin to interact with plasma ions at lower plasma densities than do the waves emitted by the antenna. Presumably, the same mechanism underlies the parametric instability in the central plasma region observed on FT-2 by the enhanced scattering technique [8]. The parametric decay of LH waves ultimately leads to a transition from the regime in which the launched RF power is absorbed by electrons to the regime in which it is absorbed by ions and to the termination of LH current drive.

ACKNOWLEDGMENTS

This work was supported in part by the Russian Foundation for Basic Research (project nos. 97-2-18084 and 98-2-18346) and INTAS (grant no. 95-1351).

REFERENCES

1. V. N. Budnikov, L. A. Esipov, and M. I. Irzak, Pis'ma Zh. Tekh. Fiz. **16** (13), 15 (1990) [Sov. Tech. Phys. Lett. **16**, 417 (1990)].
2. V. N. Budnikov and M. I. Irzak, Plasma Phys. Controlled Fusion **38** (12A), 135 (1996).
3. V. N. Budnikov, V. V. Bulanin, A. D. Gurchenko, *et al.*, Fiz. Plazmy **24** (3), 262 (1998) [Plasma Phys. Rep. **24**, 233 (1998)].
4. C. Karney, Phys. Fluids **22**, 2188 (1979).
5. L. A. Esipov, I. E. Sakharov, E. O. Chechik, *et al.*, Zh. Tekh. Fiz. **67** (4), 48 (1997) [Tech. Phys. **42**, 367 (1997)].
6. M. Yu. Kantor, A. A. Borevich, V. N. Budnikov, *et al.*, in *Proceedings of 26th European Conference on Controlled Fusion and Plasma Physics, Maastricht, 1999*, p. 1789.
7. M. Porkolab, Phys. Fluids **20**, 2058 (1977).
8. V. N. Budnikov, L. A. Esipov, M. I. Irzak, *et al.*, Pis'ma Zh. Éksp. Teor. Fiz. **48** (9), 480 (1988) [JETP Lett. **48**, 522 (1988)].

Translated by O. E. Khadin

Technical Physics Letters, Vol. 26, No. 1, 2000, pp. 67–69. Translated from Pis'ma v Zhurnal Tekhnicheskoĭ Fiziki, Vol. 26, No. 2, 2000, pp. 47–52.

The Effect of "Supercollimation" of X-Radiation in a Narrow Rough Slit

L. I. Ognev

Kurchatov Institute Russian Scientific Center, Moscow, 123182 Russia

Received April 27, 1999

Abstract—The X-ray beam propagation in a narrow channel is calculated with due regard for diffraction effects and scattering from the wall roughness; the employed approach involves the use of the complex refractive index. © *2000 MAIK "Nauka/Interperiodica".*

Mingazin *et al.* [1] observed the formation of bands in the angular beam distribution during transmission of hard X-radiation through a slit formed by two tightly compressed polished glass plates ("slitless X-ray collimator"). However, the slit width obtained in the geometrical optics approximation for this experiment [2] is much less than that following from the diffraction approximation estimates (see [3]). Therefore, it is of interest to treat the X-ray beam propagation in narrow channels with due regard for diffraction effects and scattering from the wall roughness.

As was demonstrated by way of numerical simulation [3], when an X-ray beam is trapped in a rough narrow dielectric channel, transmitted radiation features a Gaussian distribution of intensity on the transverse coordinate, which corresponds to the dominant mode. In so doing, the beam angular width is much less than the angle of total external reflection and is close to the diffraction (for the given width) slit. The scattering of X-ray radiation from rough surfaces is usually investigated within the Andronov-Leontovich approximation [4]. The case treated by us falls outside the scope of the Andronov-Leontovich approximation [4]. It falls outside the range of validity of the latter approximation because the diffraction spreading of the beam leads to losses even with zero angle of slip relative to the channel surface. In this study, we employed the approach involving the use of the complex refractive index allowing for the decay of coherence upon incoherent scattering [5] on the basis of Tatarskiĭ's statistical method (see [6, 7]). The dielectric permeability of transition layer on random boundary $x = \xi(z)$ was represented in the form $\varepsilon(x, z) = \varepsilon_1 + (\varepsilon_0 - \varepsilon_1)H[x - \xi(z)]$, where ε_1 and ε_0 respectively denote the dielectric permeability of the medium and air, z and x are the coordinates along and across the rough channel, and $H(x)$ is the step function. The equation for the averaged, slowly varying scalar amplitude of the electric vector $A(x, z)$ ignoring the scattering to large angles with due regard for the small beam width is written ignoring the term $\partial^2 A(x, z)/\partial z^2$. Assuming a small variation of $A(x, z)$ over the roughness correlation length z_{corr}, we can use the property of the correlator

$$\langle \delta\varepsilon'(x, z)A(x, z)\rangle = \langle A(x, z)\rangle(-ik/4)\int_{-\infty}^{\infty}\langle \delta\varepsilon'(x, z)\delta\varepsilon'(x, z')\rangle dz', \quad (1)$$

valid for δ-correlated fluctuating medium [7]. The coherent part of the amplitude $A(x, z)$ may be calculated from the statistically averaged "parabolic" equation (the angular brackets correspond to averaging) [5, 7],

$$2ik\partial\langle A(x, z)\rangle/\partial z - \Delta_\perp\langle A(x, z)\rangle - k^2\chi(x)\langle A(x, z)\rangle - ik^2W(x)\langle A(x, z)\rangle = 0, \quad (2)$$
$$\langle A(x, z = 0)\rangle = A_0(x),$$

where $\chi(x, z) = (\langle\varepsilon(x)\rangle - \varepsilon_0)/\varepsilon_0$. The term of equation (2) with $\chi(x)$ corresponds to the X-ray beam absorption on the channel walls, and the term with $W(x)$ corresponds to incoherent scattering,

$$W(x) = (-ik/4)\int_{-\infty}^{\infty}\langle \delta\varepsilon'(x, z)\delta\varepsilon'(x, z')\rangle dz' = -\frac{k}{4}\frac{(\varepsilon_0 - \varepsilon_1)^2}{\pi(\varepsilon_0)^2}\int_{-\infty}^{+\infty}dz'\int_{-\infty}^{x/\sigma}\exp(-\xi^2)d\xi \times \int_{x/\sigma}^{\frac{x/\sigma - R(z')\xi}{(1 - R^2(z'))^{1/2}}}\exp(-\eta^2)d\eta, \quad (3)$$

where $\delta\varepsilon'(x, z) = (\varepsilon(x, z) - \langle\varepsilon(x)\rangle)/\varepsilon_0$, $R(z)$ is the autocorrelation coefficient, and σ is the dispersion of distribution $\xi(z)$. It can be demonstrated that the quantity $W(x)$ in the middle of the transition layer ($x = 0$) and ($x = d$) is independent of σ and almost proportional to the roughness correlation length z_{corr}.

1063-7850/00/2601-0067$20.00

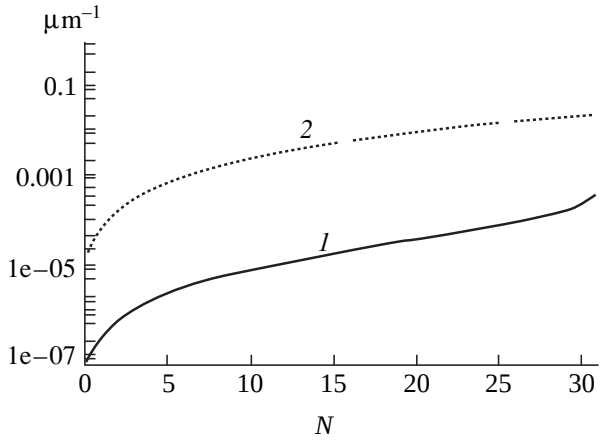

Fig. 1. The dependence of the beam attenuation coefficients on the mode number N due to absorption (solid line *1*) and incoherent scattering (broken line *2*) for σ = 400 Å and z_{corr} = 5 μm; E = 10 keV. The quartz channel width is d = 0.5 μm. The angle of entry of the beam $\vartheta_N \approx 1.2 \times 10^{-4} N$.

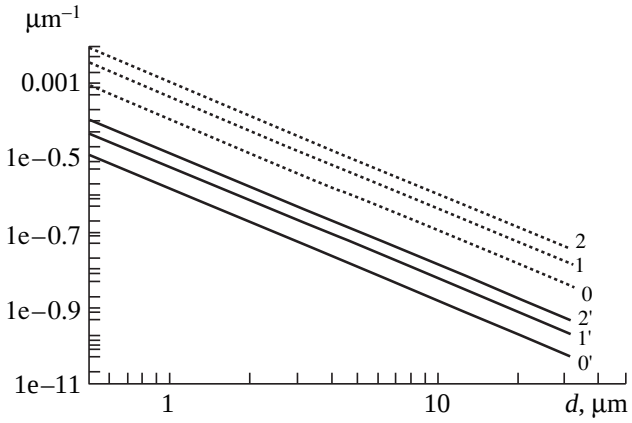

Fig. 2. The dependence of the attenuation coefficients of X-ray beam with an energy of 1 keV in a channel between silicon plates on the slit width d for modes 0, 1, and 2; σ = 400 Å, z_{corr} = 5 μm. The attenuation associated with scattering, $\beta_{scatter}$, is indicated by broken lines, and that associated with absorption, β_{absorp}, by solid lines.

The wave amplitude may be represented as an expansion in modes or eigenfunctions $\varphi_j(x)$ which are solutions of the equations

$$\Delta_\perp \varphi_j(x) = k[2k_{jz} - k\mathrm{Re}(\chi(x))]\varphi_j(x).$$

Thus, the attenuation coefficients may be found as the overlap integrals $\beta_l = -(k/2)\int \varphi_l^*(x)[\mathrm{Im}(\chi(x)) + W(x)]\varphi_l(x)dx$. For lower-order modes, the beam attenuation coefficients are proportional to σ as a result of incoherent scattering, because the height of roughness largely defines the width $W(x)$,

$$\beta_{scatter} \sim k^2(\varepsilon_0 - \varepsilon_1)^2 \times \sigma \int_{-\infty}^{\infty} dz' \int_{-\infty}^{0} \exp(-\xi^2/2)d\xi \int_{0}^{\frac{-R(z')\xi}{(1-R^2(z'))^{1/2}}} \exp(-\eta^2/2)d\eta.$$

The proportionality of the loss of beam intensity to the height of channel roughness for extra small slip angles is also observed in the results of direct numerical integration of parabolic equation with random boundary [3] (Fig. 5).

The results of calculations of the attenuation coefficients of a beam with an energy of 10 keV in channel of quartz glass 0.5 μm wide for different transverse modes N are given in Fig. 1 in the units of [μm^{-1}] separately for absorption and scattering from the wall roughness. The angles corresponding to the N mode are determined as $\varphi_N = \lambda/2d(N + 1/2)$ with $N \geq 1$. Here, σ = 400 Å and the correlation length z_{corr} = 5 μm. The value of the attenuation coefficient of the dominant coherent mode agrees with the results of numerical integration of the parabolic equation with random channel boundary [3], which lends support to the validity of the mode approximation employed.

The dependence of the attenuation coefficients of an X-ray beam with an energy of 1 keV on the slit width for three lower-order modes is given in Fig. 2. One can see from the figure that $\beta \sim 1/d^3$. This dependence takes account of both the decrease of diffraction effects with the increasing beam width $\sim\lambda/d^2$ and the decrease of the beam fraction interacting with the surface $\sim\sigma/d$. When silicon is replaced by lead, the value of the attenuation coefficients increases by a factor of 1.5. The increase of β with decreasing energy E is faster than $\sim 1/E$, which is associated both with the increase of the importance of diffraction and with the increase of the optical density of the channel wall material.

Experimentally, the effect may be measured by the decrease of the angular width of the transmitted beam to the diffraction value of λ/d, which is considerable compared with the angle of total external reflection. The effective narrowing of the angle of capture of radiation into the channel may be used to improve the angular discrimination of X-radiation detectors.

The obtained results further lead to a new interpretation of the experimental results of [1, 2]. According to the data on the angular distance between the interference peaks in the transmitted beam in view of diffraction, the slit between polished plates has a width of ~10 [3] rather than 1 μm as follows from [2] in the geometrical optics approximation. In the case of oblique incidence of the output beam, higher-order transverse modes are excited, which give numerous diffraction peaks in the transmitted beam. At the same time, if a transverse unpolished region is left in the plates, the independence of the outlet region of the slope at the inlet is associated with the strong absorption of higher-

order transverse modes with preservation of the lower-order symmetric mode.

REFERENCES

1. T. A. Mingazin, V. I. Zelenov, and V. N. Leĭkin, Prib. Tekh. Éksp., No. 1, 229 (1981).
2. V. N. Leĭkin, T. A. Mingazin, and V. I. Zelenov, Prib. Tekh. Éksp., No. 6, 33 (1984).
3. T. A. Bobrova and L. I. Ognev, Preprint No. 6051/11, IAE (Kurchatov Inst. of Atomic Energy, Moscow, 1997) (available in English at http://xxx.itep.ru/abs/physics/9807033).
4. A. V. Vinogradov, N. N. Zorev, I. V. Kozhevnikov, and I. G. Yakushkin, Zh. Éksp. Teor. Fiz. **89** (6), 2124 (1985) [Sov. Phys. JETP **62**, 1225 (1985)].
5. L. I. Ognev, in *Abstracts of Papers to the XXVII International Conference on the Physics of Interactions of Charged Particles with Crystals*, Moscow, Russia, 1997 (Moscow, 1997), p. 76.
6. V. Holy and K. T. Gabrielyan, Phys. Status Solidi B **140** (1), 39 (1987).
7. L. I. Ognev, Zh. Tekh. Fiz. **64** (5), 78 (1994) [Tech. Phys. **39** (5), 499 (1994)].

Translated by H. Bronsteĭn

Technical Physics Letters, Vol. 26, No. 1, 2000, pp. 70–74. Translated from Pis'ma v Zhurnal Tekhnicheskoĭ Fiziki, Vol. 26, No. 2, 2000, pp. 53–63.

Two Mechanisms of Phase Modulation in Multimode Fiber-Optic Interferometers

L. I. Kosareva, O. I. Kotov, L. B. Liokumovich, S. I. Markov, A. V. Medvedev, and V. M. Nikolaev

St. Petersburg State Technical University, St. Petersburg, Russia

Received September 20, 1999

Abstract—The mechanisms of phase modulation of optical radiation in multimode light guides are treated, namely, the first mechanism with equal relative phase increments for all modes and the second mechanism including the mode interaction and characterized by different relative phase increments for each mode. It is demonstrated theoretically that, in the case of several modulating effects on the light guide, the behavior of signals of modal interference from each one of those effects upon variation of the parameters of the medium surrounding the fiber depends on the type of effect. The variations of signals from the effects of the first type are in full agreement. Signals from effects of the second type or of different types may vary differently. In experiments with an intermode fiber-optic interferometer 500 m long, modulators associated with the mechanism of the first type exhibited a high correlation (97%) of the behavior of signals upon drift of the light guide temperature. The variations of signals from modulators of the second type and of different types were almost uncorrelated (6 and 1%). © *2000 MAIK "Nauka/Interperiodica".*

The phase modulation propagating in multimode fiber-optic light guides occurs as a result of diverse external effects such as variations of temperature, pressure, mechanical displacement, electric, magnetic and acoustic field, and so on [1]. This effect finds application in optical-fiber sensors (OFS) of physical quantities [2, 3] and in lines of data acquisition [4], and it shows up as "modal" noise in fiber-optic communication lines [5].

For recording the phase modulation, such devices involve single-fiber circuits in which use is made of interference between different modes and of spatial filtering of a part of the interference pattern [2, 3]. Such systems may be appropriately referred to as "intermode fiber-optic interferometers."

Two problems cause the most difficulties in the devices under consideration, namely, (1) fading of the useful signal, associated with quasistatic variations of the parameters of surrounding medium [6]; and (2) the presence of several spaced modulating effects which must be recorded simultaneously. The latter problem arises in distributed sensors of physical quantities [3] or in lines of data acquisition with discontinuous input of information by means of fiber-optic phase modulators [4].

In so doing, the behavior of signals from different effects under conditions of fading may be the same or different, which defines the method of signal recording and processing. In this study, the correlation of signals from different effects in an intermode interferometer is investigated, and the obtained results are interpreted in terms of two mechanisms of formation of phase modulation of coherent radiation in multimode light guides.

The first mechanism is characteristic of physical effects causing a relative phase increment of individual mode, which is independent of the mode number,

$$\frac{\delta\theta_m}{\theta_m} = KV,\ K = f(L_1, V, \ldots),\ K = \text{const}(m), \quad (1)$$

where θ_m is the phase delay of the mth mode in the light guide region subjected to the effect V, and K is the coefficient of relative phase increment for the given effect. This mechanism is operative under conditions of uniform heating, and isotropic pressure and tension of fiber-optic light guide [1, 2].

The second mechanism is associated with cases when external stimulation leads to a relative phase variation of the mode, depending on the mode number,

$$\frac{\sigma\theta_m}{\theta_m} = K_m V, \quad K_m \neq \text{const}(m), \quad (2)$$

where K_m is the coefficient of relative phase increment under the effect V for the mth mode. This situation arises under effects which cause the interaction of modes, namely, bending, transverse pressure, local twisting, and heating [7, 8].

Below, the main attention is given to the experimental and theoretical treatment of the correlation properties of the behavior of signals from different sources of phase modulation under conditions of slow variation of

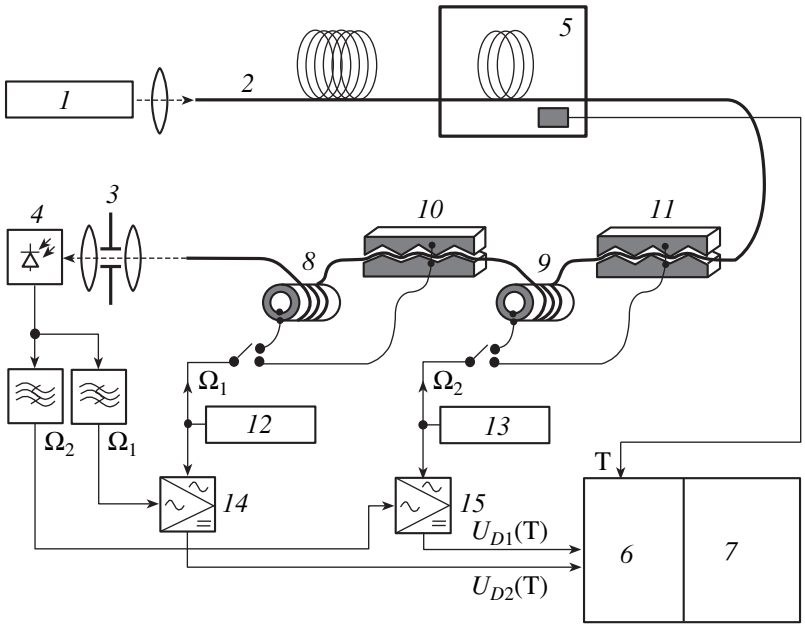

Fig. 1. Block diagram of the experimental setup.

the parameters of a light guide, which simulate the processes of "fading."

The experimental setup (Fig. 1) employed a helium-neon gas laser *1* with $\lambda = 0.63$ μm and a power of 2 mW, and a gradient fiber *2* 500 mm long with the core diameter of 50 μm and with two protective coatings (∅ = 0.8 mm). The radiation at the light guide output was focused by a lens with a built-in iris diaphragm *3* to a silicon photodiode detector *4*. The diaphragming is required to isolate the intermode interference signal. A part of a light guide 10 m long was placed in a thermostat *5*, the temperature in which was monitored by a sensor and, after an ADC *6*, recorded by a computer *7*.

Fiber-optic phase modulators of two types were used in the setup, corresponding to the above-identified mechanisms of phase modulation. Modulators of the first type, *8* and *9*, had the form of a piezoceramic cylinder 30 mm in diameter, with a fiber-optic light guide 3 m long wound on its external surface (Fig. 1). A variation of the cylinder diameter under the effect of electric signals caused in its turn a variation of the optical length of the light guide and of the phase difference of the interfering modes. In modulators of the second type, *10* and *11*, the fiber in protective envelopes was placed between a pair of serrated metal plates with a pair of piezoceramic bars (Fig. 1). The entire structure was placed in a housing with adjusting screws which enabled one to vary the static pressure on the plates to select the working point. The resulting bends of the light guide caused the mode interaction, which, in turn, led to a variation of the mode amplitudes and phases [7, 8, 10].

The phase modulators were excited by harmonic signals (generators *12*, *13*) on the frequencies Ω_1 and Ω_2 in the range of 1–30 kHz.

The experiment involved simultaneous recording of the level and sign of harmonics of the output signal with the frequencies Ω_1 and Ω_2 ("responses" from different modulators) under conditions of slow variation of the temperature of the part of fiber placed in the thermostat. For this purpose, the output-signal components were selected with respect to frequency and detected by synchronous detectors *14* and *15* (time constant of 0.1 s). The output signals of the detectors, U_{D1} and U_{D2}, were applied to the ADC and recorded by the computer.

In scanning the temperature of the light guide segment, the computer registered a two-dimensional sampling of values $\{U_{D1k}; U_{D2k}\}$. Because the 10-m portion of the light guide varied by several tens of degrees, the resultant sampling is adequately representative of the statistics of operation of the intermode interferometer under real conditions. The experimental results (Fig. 2) reveal a considerable difference in the correlation of the values of output signals depending on the type of modulator.

The correlation coefficient of signals from the modulators was calculated by the conventional formula [9]

$$\rho_{12} = \frac{c_{12}}{\sigma_1 \sigma_2}, \tag{3}$$

where $c_{12} = \langle U_{D1} U_{D2} \rangle$ is a covariance and $\sigma^2_{1,2} =$

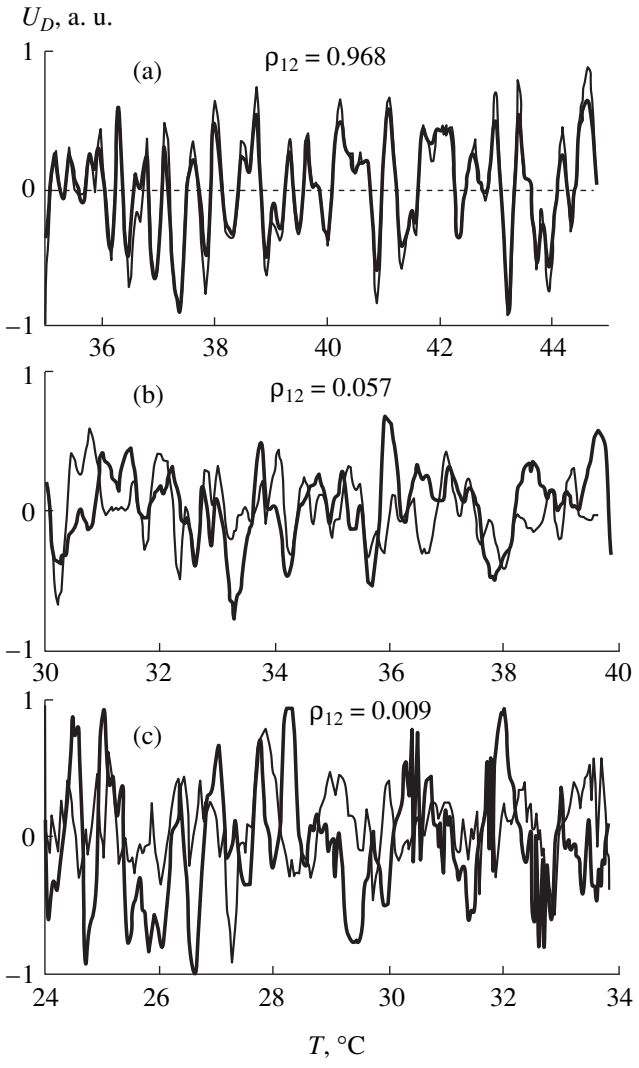

Fig. 2. Signals of synchronous detectors as functions of the light guide temperature (the bold line indicates the U_{D1} signal, and the fine line indicates the U_{D2} signal): (a) modulators of type I (M1 and M3), (b) modulators of different types (M1 and M2), and (c) modulators of type II (M2 and M4).

$\langle U^2_{D1,\,2k} \rangle$ denotes dispersions for simultaneous sampling $\{U_{D1k}; U_{D2k}\}$.

Figure 2 gives fragments of derived correlations in the range of temperature variation $\Delta T \sim 10$°C. In order to calculate the correlation coefficients, use was made of the sampling obtained in the range of $\Delta T \sim 60$°C.

The signals from two modulators of the first type are almost fully correlated (Fig. 2a); the correlation coefficient $\rho_{12} = 0.968$. This result did not depend on the location of the modulators and amplitudes of modulating signals (provided the conditions of smallness of signals were valid), the number of light guide turns on the modulator, and the size of the diaphragm at the output of the optical circuit.

The signals from two modulators of different types (Fig. 2b) are in fact uncorrelated ($\rho_{12} = 0.057$) in a wide range of the experimental conditions, namely, the position of modulators, degree of diaphragming, and amplitudes of the exciting signals.

The signals from two modulators of the second type were not fully correlated either ($\rho_{12} = 0.009$), in spite of the fact that the modulators proper and their operating conditions were selected to be as similar as possible (Fig. 2c).

In order to interpret the derived correlations, one must treat the intensity of light at the fiber output, with due regard for the above-identified conditions of phase increment for modulators of different types.

In diaphragming, the light wave intensity for monochromatic excitation may be written as [1, 6]

$$I = \sum_{m=1}^{N} a_m + \sum_{m \neq n}^{N} \sum^{N} a_{mn} \cos(\Delta\beta_{mn} L + \Delta\Phi_{mn}), \quad (4)$$

where

$$a_m^2 = \frac{1}{2} A_m^2 \iint E_m^2(r, \varphi) ds,$$

$$a_{mn} = A_m A_n \iint_{\Delta S} E_m(r, \varphi) E_n(r, \varphi) ds,$$

A_m is the coefficient of excitation of the mth mode; $E_m(r, \varphi)$ is the mode function of the mth mode of the transverse coordinates r, φ; ΔS is the surface on the output end of the fiber, isolated by the diaphragm; $\Delta\beta_{mn}L + \Delta\Phi_{mn} = (\beta_m - \beta_n)L + \Phi_m - \Phi_n$ is the phase delay difference of radiation of the mth and nth modes in the light guide; β_m is the propagation constant of the mth mode; L is the light guide length; and Φ_m is the phase shift of the mth mode, defined by numerous phase increments of the light wave for the time of propagation in the fiber, as a result of "defects" (nonuniformities and bends) leading to longitudinal irregularity of the light guide and to mode interaction [5, 7, 8]. As is known [6, 7], the diaphragming of output radiation in intermode fiber-optic interferometers is necessary for transforming the phase modulation of light waves into the modulation of intensity. In recording the total radiation, the coefficients $a_{mn} = 0$ and the interference signal are absent by virtue of orthogonality of the modes.

The effects on the fiber-optic light guide by the phase modulator of physical quantity V to be measured cause variations of the phases of individual modes and their differences, this leading to a variation in the intensity $\delta I(V)$, i.e., signal of intermode interference.

For informative description of the effect of the first type, we will use the model of modulation of the geometric length of light guide $\delta L(V)$. The inclusion of variation of the refractive index of the core upon real

mechanical elongation of the fiber renders the relevant formulas more cumbersome, without changing the essence of the processes and the results of treatment. The phase difference of the modes may be represented as

$$\Delta\varphi_{mn} = \Delta\beta_{mn}L + \Delta\Phi_{mn} + \Delta\beta_{mn}\delta L(V). \quad (5)$$

In case several sources of phase modulation of the first type are available, each one of those sources will cause a corresponding phase increment.

The variation of light intensity δI caused by $\delta L(V)$ may be derived from expression (4),

$$\delta I = \delta L(V)\left\{\sum_{m\neq n}^{N}\sum^{N} a_{mn}\sin(\Delta\beta_{mnL} + \Delta\Phi_{mn})\Delta\beta_{mn}\right\}, \quad (6)$$

where the smallness of phase increment $\Delta\beta_{mn}$ $\delta L(V) \ll 1$ is included. For example, for two different effects V_1 and V_2 leading to elongations δL_1 and δL_2, the "responses" with respect to intensity will be

$$\delta I_1 = \delta L_1(V_1)\left\{\sum_{m\neq n}^{N}\sum^{N} a_{mn}\sin(\Delta\beta_{mn}L + \Delta\Phi_{mn})\Delta\beta_{mn}\right\},$$
$$\delta I_2 = \delta L_2(V_2)\left\{\sum_{m\neq n}^{N}\sum^{N} a_{mn}\sin(\Delta\beta_{mn}L + \Delta\Phi_{mn})\Delta\beta_{mn}\right\}. \quad (7)$$

If the elongation $\delta L(V)$ is fixed, the magnitude and sign of the respective variation of intensity are defined by the sum in curly brackets. As the external conditions, first of all, the light guide temperature, vary, the parameters $\Delta\beta_{mn}$ vary to cause the so-called "fading" of signal of the intermode interferometer [6].

Because, as follows from (6) and (7), the variations of intensity due to elongations δL_1 and δL_2 differ only by the registered magnitude of the effect, the variation of signals during the variation of the light guide temperature will be uniform, and the correlation coefficient is unity:

$$\rho_{12} = \frac{\langle\delta I_1\delta I_2\rangle}{\sqrt{\langle\delta I_1^2\rangle\langle\delta I_2^2\rangle}} = \frac{\delta L_1\delta L_2\left\langle\left(-\sum_{m\neq n}^{N}\sum^{N} a_{mn}\sin(\Delta\beta_{mn}L + \Delta\Phi)\beta_{mn}\right)^2\right\rangle}{\sqrt{\delta L_1^2\delta L_2^2}\left\langle\left\langle\left(-\sum_{m\neq n}^{N}\sum^{N} a_{mn}\sin(\Delta\beta_{mn}L + \Delta\Phi)\beta_{mn}\right)^2\right\rangle\right\rangle^2} = 1. \quad (8)$$

Therefore, the degree of fading of the output signal components under any effects of the first type is the same for any parameters of the circuit such as the degree of diaphragming at the light guide output, location and amplitude of the effects (provided the condition of smallness is valid), mode composition, etc.

It will be recalled that harmonic modulating effects were used in the experiment for more convenience in signal discrimination and in quantitative measurements of signals. The signal components from different modulators were selected by frequency, after which their amplitude and sign were recorded by synchronous detection.

Effects of the second type, leading to phase modulation with phase increment of the modes depending on the mode number (expression (2)), may be explained in terms of mode coupling. In so doing, the phase delay increment of the mode over the interaction length l may be written in terms of increments of propagation constants in this segment,

$$\beta_m(V) = \beta_m + \sigma\beta_m = \beta_m + \sum_{n=1}^{N}\frac{k_{mn}^2}{\Delta\beta_{mn}}, \quad (9)$$

where k_{mn} denotes the coefficients of mode coupling [8, 10].

Then, the increment of output intensity due to the relevant effect will take the form

$$\delta I = \left\{\sum_{m\neq n}^{N}\sum^{N} a_{mn}\delta\beta_{mn}l\sin(\Delta\beta_{mn}L + \Delta\Phi_{mn})\right\}, \quad (10)$$

where $\delta\beta_{mn} = \delta\beta_m - \delta\beta_n$ is a set of sign-variable quantities defined by the effect leading to mode coupling. For two effects, we have

$$\delta I_1 = l_1\left\{\sum_{m\neq n}^{N}\sum^{N} a_{mn}\delta\beta_{mn}^{(1)}\sin(\Delta\beta_{mn}L + \Delta\Phi_{mn})\right\},$$
$$\delta I_2 = l_2\left\{\sum_{m\neq n}^{N}\sum^{N} a_{mn}\delta\beta_{mn}^{(2)}\sin(\Delta\beta_{mn}L + \Delta\Phi_{mn})\right\}. \quad (11)$$

In this case, unlike (7), the signals from different effects differ by the coefficients at sinusoidal terms in the sum. Therefore, during drift of the light guide temperature, δI_1 and δI_2 may vary differently.

We will assume that, because of the complexity and plurality of factors of the mechanism of mode coupling, different effects (differing by the physical mechanism, amplitude, interaction length l, etc.) lead to different sets of $\delta\beta_{mn}^{(1)}$ and $\delta\beta_{mn}^{(2)}$ of different magnitudes and

signs. In calculating the correlation coefficient for signals (11), the averaging over T (in view of $\langle \sin^2(aT)\rangle = 1/2$ and $\langle \sin(aT)\sin(bT)\rangle = 0$ for $a \neq b$) yields

$$\rho_{12} = \frac{\langle \delta I_1 \delta I_2 \rangle}{\sqrt{\langle \delta I_1^2 \rangle \langle \delta I_2^2 \rangle}}$$

$$= \frac{l_1 l_2 \sum_{m \neq n}^{N} \sum^{N} a_{mn}^2 \delta\beta_{mn}^{(1)} \delta\beta_{mn}^{(2)}}{\sqrt{l_1^2 l_2^2 \left(\sum_{m \neq n}^{N} \sum^{N} a_{mn}^2 (\delta\beta_{mn}^{(1)})^2 \right) \left(\sum_{m \neq n}^{N} \sum^{N} a_{mn}^2 (\delta\beta_{mn}^{(2)})^2 \right)}}. \quad (12)$$

Because, as was already mentioned, the sets $\delta\beta_{mn}^{(1)}$ and $\delta\beta_{mn}^{(2)}$ include different sign-variable coefficients, one can see from (12) that, for high values of N, the correlation coefficient of signals (11) $\rho_{12} \longrightarrow 0$. As in the previous case, this result does not depend on the system parameters at the light guide input and output.

Note, finally, that for two effects of different types the fading of signals is uncorrelated. For two effects of different types,

$$\delta I_1 = \delta l_1 \left\{ \sum_{m \neq n}^{N} \sum^{N} a_{mn} \Delta\beta_{mn} \sin(\Delta\beta_{mn} L + \Delta\Phi_{mn}) \right\},$$

$$\delta I_2 = l_2 \left\{ \sum_{m \neq n}^{N} \sum^{N} a_{mn} \delta\beta_{mn}^{(2)} \sin(\Delta\beta_{mn} L + \Delta\Phi_{mn}) \right\}, \quad (13)$$

one can readily see that a variation of sine arguments leads to different variations of δI_1 and δI_2, and the correlation coefficient tends to zero for the same reasons as in the previous case.

Therefore, the obtained results demonstrate that the mechanism of mode coupling, which is usually ignored, may cause uncorrelated signal responses. These singularities must be taken into consideration in developing optical-fiber sensors, data acquisition lines, and other devices employing intermode interference.

In addition, these results appear to be useful from the standpoint of refining models of mode noise in multimode fiber-optic systems.

REFERENCES

1. M. M. Butusov, S. L. Galkin, S. P. Orobinskiĭ, and B. P. Pal, *Fiber Optics and Instrument Making* (Mashinostroenie, Leningrad, 1987).
2. N. N. Evtikhiev, É. A. Zasovin, and D. I. Mirovitskiĭ, Itogi Nauki Tekh. Svyaz' **8**, 24 (1991).
3. Yu. V. Gulyaev, M. Ya. Mesh, and V. V. Proklov, *Modulation Effects in Fiber-Optic Light Guides* (Radio i svyaz', Moscow, 1991).
4. B. Culshaw, P. R. Ball, J. C. Pond, and A. A. Sadler, Electronics and Power **11** (2), 148 (1981).
5. B. Crosignani, and A. Yariv, J. Opt. Soc. Am. **73** (8), 1022 (1983).
6. S. A. Kingsly and D. E. N. Davies, Electron. Lett. **14** (11), 322 and 335 (1978).
7. O. I. Kotov, O. L. Marusov, and V. M. Nikolaev, Pis'ma Zh. Tekh. Fiz., **16** (7), 47 (1990) [Sov. Tech. Phys. Lett. **16** (7), 47 (1990)].
8. H.-G. Unger, *Planar Optical Waveguides and Fibres* (Clarendon Press, Oxford, 1977; Mir, Moscow, 1980).
9. J. S. Bendat and A. G. Piersol, *Random Data: Applied Analysis* (Mir, Moscow, 1989).
10. H. F. Taylor, J. Lightwave Technol. **1** (LT-2), 617 (1984).

Translated by H. Bronsteĭn

Technical Physics Letters, Vol. 26, No. 1, 2000, pp. 75–76. Translated from Pis'ma v Zhurnal Tekhnicheskoĭ Fiziki, Vol. 26, No. 2, 2000, pp. 64–68.

Visualization of the Ion Projected Range Region in GaAs Irradiated with Argon Ions

V. M. Busov, G. B. Venus, G. M. Gusinskiĭ, N. D. Il'inskaya, V. O. Naĭdenov, A. A. Pasternak, E. L. Portnoĭ, and S. I. Troshkov

Ioffe Physicotechnical Institute, Russian Academy of Sciences, St. Petersburg, 194021 Russia

Received September 29, 1999

Abstract—Cleavages of GaAs samples irradiated with 2.1, 4.6, and 8.4 MeV Ar^+ ions were studied by scanning electron microscopy (SEM). SEM visualization of the ion projected range region was used to determine the range of Ar^+ projectiles in the semiconductor target. © *2000 MAIK "Nauka/Interperiodica".*

INTRODUCTION

At present, considerable interest of researchers is drawn to investigation of the interaction of accelerated heavy ions with solids in the ion energy range of 10^2–10^4 keV.

This interest is primarily explained by prospects in the development of micro- and nanoelectronic technologies, 3D technologies, and nondestructive analytical methods. Programs for such investigations are in progress in all large heavy particle accelerators. By now, the main physical processes involved in the interaction between high-energy ions with solids (crystals, amorphous solids, metals, etc.) have been elucidated to a considerable extent [1–3]. At the same time, technological applications related to particular solid-state structures require much more detailed and profound knowledge of the processes involved. In particular, the task of modification of multilayer semiconductor structures by accelerated heavy ion beams implies precise determination of the stopping losses, projected range, and straggling (longitudinal and lateral scatter) of heavy-ion projectiles in semiconductor targets.

Another important aspect of the study of heavy ion retardation in solid targets is related to investigations of the structure of nuclei, including the lifetimes of their excited states [4] (in particular, high-spin nuclear levels extensively studied in recent years in the context of the superdeformation phenomenon [5]). The reason is that most of the nuclear energy levels are characterized by lifetimes falling within the range from 10^{-14} to 10^{-11} s. The main technique used for determining these lifetimes is based on analysis of the shape of gamma-radiation spectra from recoil nuclei excited by nuclear reactions and distorted by the Doppler effect [6]. Since a measure of time in this method is the characteristic time of recoil retardation in the target substance, the reliability of information about the stopping energy losses of heavy (recoil) nuclei is directly related to the accuracy of lifetime determination.

At present, theoretical estimates of the electron and nuclear components of the stopping power of solids, as well as the projected range and straggling, are either taken from special tables [1] or calculated using an equivalent TRIM computer program. As the velocity of primary heavy ions increases, the electron-induced stopping losses grow linearly, then (after reaching a certain "critical" ion velocity of the order of 1–3% C) follow a dome-shaped curve, and finally drop with increasing ion velocity. For a comparatively high primary ion velocity, the accuracy of data in the tables [1] is quite acceptable (10–15%), but the errors can markedly increase [7, 8] in the region of linear growth. This is primarily related to uncertainty [9] in the theoretical estimates of the critical velocity [10], which serve as a basis for calculation of the tabulated data [1]. The maximum uncertainty may appear in the calculation of straggling: according to [1], this error may reach up to ±20% for light ions and even 200% for heavy projectiles.

It should be noted that experimental data are frequently obtained by Doppler gamma-spectroscopy techniques [11, 12]. For this reason, any new approach to determining the projected range and stopping powers of heavy ions in various media are of considerable importance for both fundamental and applied physics.

Below we propose a comparatively simple method for determining the projected range and stopping energy losses of heavy ions in semiconductors.

EXPERIMENTAL METHOD AND RESULTS

The proposed method is based on the fact that the secondary-electron scanning electron microscopy (SEM) images of semiconductor samples, irradiated by heavy ions with an energy of several MeV and a dose of 10^{11}–10^{13} cm^{-2}, exhibit differential brightness in the ion projected range region and beyond this range. Our experiments were performed with a GaAs crystal. A thoroughly prepared sample surface with several

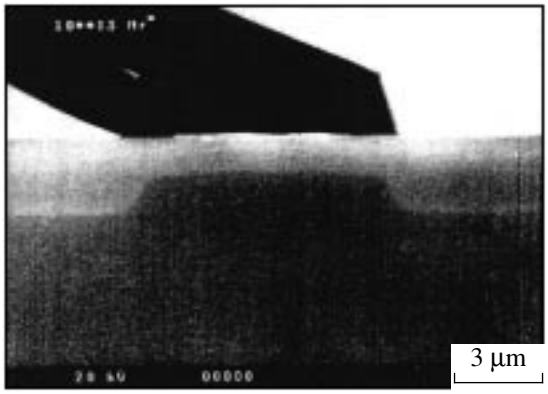

Fig. 1. SEM micrograph of a GaAs sample cleavage upon Ar^+ ion bombardment (see the text for explanation).

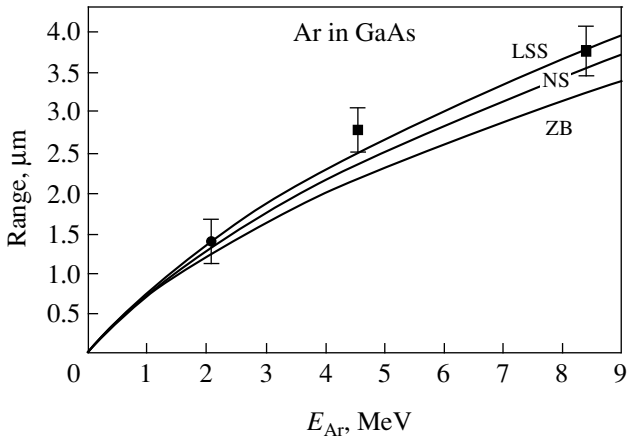

Fig. 2. The plots of projected range versus energy for Ar^+ ions in GaAs (see the text for explanation).

bands of a photoresist mask was exposed to Ar^+ ions with the energy of 2.1, 4.6, or 8.4 MeV.

Figure 1 shows a micrograph of the mirror cleavage of a GaAs sample with photoresist. The sample was irradiated with 4.56-MeV Ar^+ ions to a dose of 10^{13} cm^{-2}. As is seen, the ion penetration depth under the photoresist mask band is smaller as compared to that outside this region (i.e., under the open surface). Thus, it is possible to detect the ion range and measure the energy loss in the photoresist layer in the region of nuclear losses. The image presented in Fig. 1 was obtained using a Cam-Scan S4-90FE scanning electron microscope operated in the secondary-electron mode with a probing electron beam energy of 20 keV.

Processing of the results obtained in a series of experiments showed that the image contrast is strongly dependent on the ion type and irradiation dose. For argon ions, a contrast between ion-modified and non-modified regions was observed for the irradiation doses exceeding 5×10^{11} cm^{-2}, which was explained by a difference in the spectra of secondary electrons emitted from these regions.

Figure 2 shows the data for three different energies of Ar^+ ions. As seen, the measured ion ranges (black points) exceed the values calculated using the TRIM program (ZB curve) [1] and the longitudinal straggling (indicated by the error bars) is approximately the same in all points. For the comparison, Fig. 2 shows data from the well-known Nortcliffe–Shilling (NS) tables [2] with an allowance for a difference between the projected and total ranges (data in the NS tables refer to the range along the track) and the values calculated according to the Lindhard–Sharff–Schiott (LSS) theory [3]. The nuclear losses, assumed to be the same in all cases, were described using the universal potential adopted in [1].

We believe that further development of the proposed approach would lead to a rather simple method for determination of the stopping losses and projected ranges of heavy ions in semiconductor materials in a broad energy range.

ACKNOWLEDGMENTS

This work was supported by the All-Russia Interinstitution Scientific-Technological Program “Physics of Solid-State Nanostructures,” project no. 99-200036.

REFERENCES

1. F. Ziegler, J. Biersack, and U. Littmark, *The Stopping Powers and Ranges of Ions in Matter* (Pergamon, New York, 1985), Vol. 1.
2. L.C. Nortcliffe and R.F. Shilling, Nucl. Data Tables A **7** (3–4), (1970).
3. I. Lindhard, M. Sharff, and H.E. Schiott, Mat. Fys. Dan. Vid. Selsk. **33** (14), 1 (1963).
4. A. E. Zobov, I. Kh. Lemberg, and A. A. Pasternak, Izv. Akad. Nauk SSSR, Ser. Fiz. **54**, 998 (1990).
5. T. Rzaca-Urban, A. A. Pasternak, R. Lieder, *et al.*, Nucl. Phys. A (in press).
6. I. Kh. Lemberg and A. A. Pasternak, *Modern Gamma-Spectroscopy Techniques* [in Russian] (Leningrad, 1985).
7. Yu. N. Lobach, A. A. Pasternak, J. Srebrny, *et al.*, Acta Phys. Polon. B **30**, 234 (1999).
8. K. Arstila, J. Keĭnonen, and P. Tikkanen, Nucl. Instrum. Meth. Phys. Res., Sect. B **101**, 321 (1995).
9. K. Arstila, J. Keĭnonen, and P. Tikkanen, Phys. Rev. B: Condens. Matter. **41**, 6117 (1990).
10. W. Brandt and M. Kitagawa, Phys. Rev. B: Condens. Matter. **25**, 5631 (1982).
11. I. Kh. Lemberg and A. A. Pasternak, Nucl. Instrum. Meth. **140**, 71 (1977).
12. A. Antilla, S. Brandenburg, I. Keĭnonen, and M. Blister, Nucl. Phys. A **334**, 205 (1980).

Translated by P.P. Pozdeev

Technical Physics Letters, Vol. 26, No. 1, 2000, pp. 77–78. Translated from Pis'ma v Zhurnal Tekhnicheskoĭ Fiziki, Vol. 26, No. 2, 2000, pp. 69–71.

Trivalent Titanium as a Probe for Studying the Structure of the Nearest Ionic Environment in Inorganic Systems

I. M. Batyaev, T. N. Vinogradova, and Yu. G. Kobezhikov

Russian State Pedagogical University, St. Petersburg, Russia

Received June 15, 1999

Abstract—The synthesis of a new type of glass having the composition Al_2O_3–P_2O_5 with a titanium impurity and its optical and luminescence properties are reported. *© 2000 MAIK "Nauka/Interperiodica".*

This study was undertaken with the aim to show that trivalent titanium can be used as a probe for studying the environment of various ions in inorganic systems.

The use of a Eu^{3+}-ion probe for studying material structures was described in [1].

Since 1982, trivalent titanium ions have been used as activators in the α-corundum crystals for designing materials for tunable lasers [2].

We used trivalent titanium ions for creating laser materials in glassy matrices [3–5].

When studying spectral–luminescence characteristics, we paid attention on the character and the value of splitting of the $3d^i$-level of titanium depending on the matrix composition and its structure occurring in full accordance with the theory of a crystal field.

Depending on the composition and the structure of a glassy matrix, it is possible to lift the degeneracy of the $3d^i$-levels and thus increase the number of levels up to five, which, in fact, signifies the complete lift of the degeneracy of the ^2D term.

The qualitative aspect of the theory of crystal field was considered in the simple and clear form elsewhere [6].

Splitting of the *d*-orbitals in fields of various symmetries is a well-known phenomenon [6].

The quantitative calculation of splitting in the theory of a crystal field does not encounter any considerable difficulties, because the group–theoretical analysis of the impurity-ion states in crystals is developed quite well [7].

Splitting of *d*-orbitals in ions depends on the structure of the corresponding coordination polyhedron: the symmetry transformation "spherical symmetry $\longrightarrow$ octahedron (O_h, C_{4V}) $\longrightarrow$ octahedron (trans D_{4h}) and plane square (D_{4h})" results in a four-level splitting of the $b_{1g}(d_{x2-y2})$, $b_{2g}(d_{xy})$, $d\log(d_{z2})$, and $\log(d_{zx}, d_{yz})$ orbitals. The further lowering of the symmetry should give rise to a further splitting of *d*-orbitals and the appearance of the fifth level.

The relationships between the point symmetry groups can be found in numerous monographs on crystallography [8].

The complete splitting of 3*d*-orbitals should be observed in ions with the nearest environment of a very low symmetry and, in particular, in ions contained in glassy systems.

Glass and glassy systems are noncrystalline (amorphous) substances forming no characteristic coordination polyhedra [9].

Therefore, splitting of 3*d*-orbitals in glassy matrices is more complete, and some glassy systems demonstrate complete splitting of the $3d^i$-orbital of Ti^{3+}-ions.

In the course of our study, we synthesized a glass of the composition $25\%Al_2O_3$–$75\%P_2O_5$ (mol %) with $0.5\%Ti_2O_3$. This violet-color glass was optically transparent in the whole visible range. The electron absorption spectrum showed a broad band with the maximum at 595 nm and a clearly pronounced arm in the range 660–800 nm. The data obtained were attributed to the electronic transitions $^2B_2 \longrightarrow {}^2B_1$ and $^2B_2 \longrightarrow {}^2A_1$. The 10Dq value in the $Al(PO_3)_3$–Ti^{3+} glass was much lower than that in the Al_2O_3–Ti^{3+} crystals, which is explained by a higher degree of the tetragonal distortion of the $[TiO_6]$ chromophore.

The glass sample showed an intense luminescence at $\lambda_{max} = 890$ nm and had the halfwidth $\Delta\lambda = 200$ nm, and the arm in the range 780–820 nm. The experimentally observed bands were attributed to the $^2A_1 \longrightarrow {}^2E$ transition, and the clearly seen arm was considered as an indication to splitting of the lower ^2E doublet into two singlets. Thus, we obtained a system with five-level splitting of $3d^i$-orbitals of trivalent titanium at 298 K, which indicated a distorted octahedral coordination of titanium (III) [5]. Similar splitting into five levels was earlier observed by Nelson, Wong, and Schawlow in $Al_2O_3 : Ti^{3+}$ crystals in the temperature range from 4 to 77 K [10].

Splitting of the $3d^i$ orbitals of titanium (III) indicates that it can be used as a probe for studying the structure

1063-7850/00/2601-0077$20.00

of the nearest environment, because the energy difference between the levels allows one to draw certain conclusions about the strength of the crystal field and the structure of the nearest environment of an ion.

REFERENCES

1. V. F. Zolin and P. P. Koreneva, *Rare Earth Probe in Chemistry and Biology* (Nauka, Moscow, 1980).
2. P. F. Moulton, J. Opt. Soc. Am. B **3** (1), 125 (1986).
3. S. B. Sukhanov and I. M. Batyaev, Opt. Spektrosk. **72** (6), 1367 (1992).
4. I. M. Batyaev and E. B. Kleshchinov, Opt. Spektrosk. **81** (5), 823 (1996).
5. I. M. Batyaev and Yu. G. Kobezhikov, Opt. Spektrosk. **85** (1), 68 (1998).
6. I. B. Bersuker, *Electronic Structure and Properties of Coordination Compounds* (Khimiya, Leningrad, 1976).
7. D. T. Sviridov, R. P. Sviridova, and Yu. F. Smirnov, *Optical Spectra of Transition Metal Ions in Crystals* (Nauka, Moscow, 1976).
8. M. A. El'yashevich, *Atomnaya i Molekulyarnaya Spekroskopiya* (Fizmatgiz, Moscow, 1962).
9. S. A. Dymbovskiĭ and E. A. Chechetkina, *Glass Formation* (Nauka, Moscow, 1990).
10. E. D. Nelson, J. Y. Wong, and A. L. Schawlow, Phys. Rev. **156** (2), 298 (1967).

Translated by L. Man

Technical Physics Letters, Vol. 26, No. 1, 2000, pp. 79–80. Translated from Pis'ma v Zhurnal Tekhnicheskoĭ Fiziki, Vol. 26, No. 2, 2000, pp. 72–76.

Effect of a Thin Diamondlike Coating on the Emission Characteristics of Tungsten Tips

S. A. Pshenichnyuk and Yu. M. Yumaguzin

Baskotorstan State University, Baskotorstan, Russia

Received July 5, 1999

Abstract—The effect of an ion-beam deposited carbon coating on a tungsten tip on field emission of electrons has been studied. The analysis of the current–voltage characteristics showed a considerable enhancement of the emission current caused by a decrease in the working function and higher stability of emission from the tip coated with a thin carbon film. © *2000 MAIK "Nauka/Interperiodica".*

Today, thin diamondlike carbon films are considered to be promising materials for manufacturing field-emission cathodes reliably operating under the conditions of a relatively low vacuum [1]. Several authors have already reported an increase of the emission current and stable field emission from silicon and molybdenum tips coated with diamondlike films by the methods of chemical vapor deposition (CVD) and electrophoresis. The tips are preliminarily kept in a suspension of a diamond powder in ethanol to provide artificial nucleation, which can result either in the formation of a polycrystal layer or in growth of individual diamond crystallites either on the side surface of the tip or at its end [2]. We studied tungsten emitters coated with thin diamondlike films having an amorphous structure (checked by the field-emission electron microscopy of the tip surface during the measurements of its emission characteristics). Carbon coatings on the metal-tip surface were obtained by the method of ion-beam deposition described elsewhere [3]. Prior to the film deposition, the surface of a tip rigidly fixed on an arc was cleaned for 1 minute by a transmitted current heating it to a temperature up to 1100°C. The carbon layer was deposited for an hour by a 1-μA current of 80 eV-ions. The thickness of the diamondlike coating on the tip surface did not exceed 10 nm.

To clarify the role of the coating, we compared the emission characteristics of the pure tungsten tip and the tungsten tip coated with a carbon film using the following method. As is well known, the slope of the current–voltage characteristics in the Fowler–Nordheim coordinates is determined by the quantity $\varphi^{3/2}/\beta$, where φ is the work function from the areas of the emitter surface used in the measurements, and β is the geometric parameter of the tip. Thus, if the β value remains constant for the tungsten cathode and the same cathode coated with a diamondlike film, one can estimate the change in the work function from the film surface with a high precision and, thus, determine the effect of the coating on the emission characteristics of the tip. For tungsten tips with the curvature radius of about 1 μm and the coatings not exceeding 10 nm in thickness, the deposition of the film almost does not change the emitter shape and, thus, the field strength at its surface.

We experimentally studied the emission from a tungsten tip by determining the temperature of the holding arc, which provided the formation of the characteristic emission pattern of atomically pure tungsten. This temperature did not change the geometric shape of the tip, which was checked by considering its current–voltage characteristics. Then, the tip was transferred into a special chamber, where it was heated to the preliminarily determined temperature and coated with a diamondlike film. Then the emitter was transferred back to the chamber of a field-emission spectrometer to measure the current–voltage characteristics from the coated emitter in a vacuum not lower than 10^{-9} Torr.

Figure 1 shows the temporal dependences of a complete photoemission current from a pure tungsten tip and from the same tip coated with a diamondlike film. Both dependences were measured immediately upon slight heating of the emitter with the aim to remove a layer of adsorbed atoms. The removal of this layer could be seen from the emission pattern formed on the

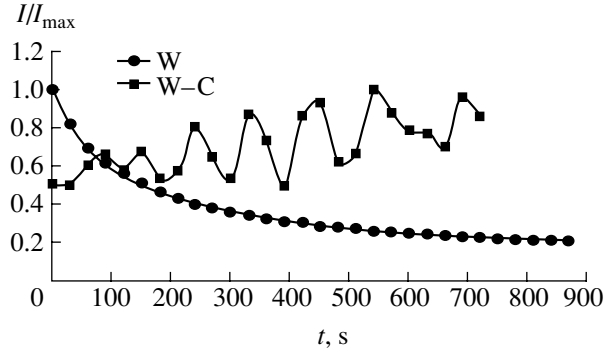

Fig. 1. Temporal dependences of the total emission current from a tungsten tip coated with a diamondlike film (W–C) and uncoated (pure) tungsten tip (W).

1063-7850/00/2601-0079$20.00 © 2000 MAIK "Nauka/Interperiodica"

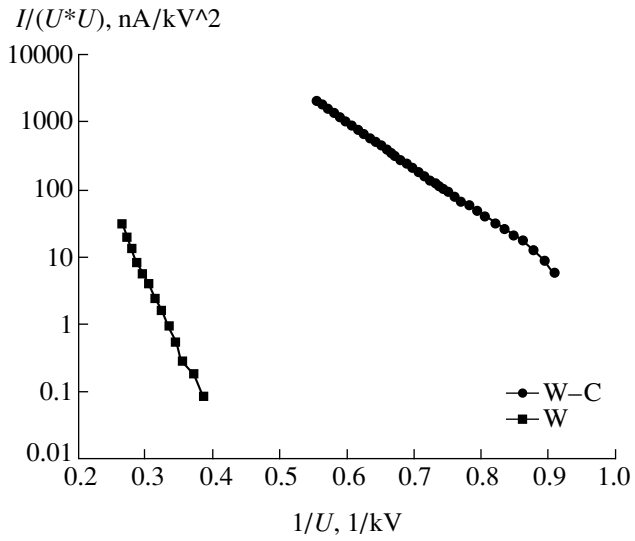

Fig. 2. Current–voltage characteristics for a pure tungsten tip (W) and a tip coated with a diamondlike film (W–C) in the Fowler–Nordheim coordinates.

luminescent screen. As is seen from Fig. 1, within ten minutes upon the application of a high voltage to the tip, the current from the pure tungsten tip considerably reduced, because of the ion bombardment of the tip surface and adsorption of the residual-gas molecules. This was clearly seen from the emission pattern, which, first, corresponded to the pattern from an ideal tungsten tip at the initial moment and, then, within a certain time, became rather blurred. It should be emphasized that each subsequent heating of the emitter restored the image of a pure tungsten tip. On the contrary, the current from the field emitter coated with a diamondlike film showed no such irreversible current reduction. In other words, in the latter case we observed the long-term stability. The field-emission electron microscopy data indicate that the coated tip surface is insensitive to the bombardment with residual-gas ions. The observed large-amplitude current fluctuations can be interpreted as follows.

The current was most stable either at low or at high emission voltages. This is explained by the existence of a certain transient range of fields providing the most intense migration of surface atoms and the appearance and disappearance of the emitting areas. It seems that, at low fields, the field-stimulated surface migration is too low, whereas at high fields, all the emitting areas are "functioning" and the pattern stability is provided by the stationary field distribution over the emitter surface and the forces acting onto the surface atoms from the emitter. The curve in Fig. 1 corresponding to the coated cathode was deliberately recorded in the range of "moderate" fields, i.e., for the least stable situation. A weak sensitivity of the emitter to the residual gas in this case is associated not with chemical inertness of the film surface (because its structure differs from the structure of "tetrahedral" amorphous carbon with a pronounced sp^3-hybridization, which is the closest to the diamond structure), but rather with the stability of carbon materials against the bombardment with the residual-gas ions. However, we cannot exclude possible hindrance of adsorption on the material surface because of the absence of dangling bonds.

The changes in the work function for the surface of the tungsten tip during deposition of a thin carbon layer can be determined from the current–voltage characteristics constructed in the Fowler–Nordheim coordinates (Fig. 2). It is seen that the tip coating allows one to increase the emission current by more than two orders of magnitude, with the other conditions being the same. Since these dependences correspond to the total current from the tip (and not from any of its individual faces), one has to use a certain averaged work function for the surface, which, for tungsten, equals 4.5 eV. The work function for a coated surface estimated from the curve slopes equals 2.1 eV; i.e., it has a value providing electron tunneling into vacuum at considerably lower applied fields.

Finally, we also managed to obtain thin amorphous carbon coatings on the surfaces of thin tungsten tips. It was established that such treatment of the emitter considerably increases the stability of the field-emission current from the cathode and emission intensity, which is explained by a considerable reduction of the work function for the surface (estimated from the slope of the current–voltage characteristics in the Fowler–Nordheim coordinates). We also managed to interpret an increased stability of the emission observed for emitters coated with thin diamondlike films.

REFERENCES

1. M. W. Geis, J. C. Twichell, and T. M. Lyszczsarz, J. Vac. Sci. Technol. B **14** (3), 2060 (1996).
2. E. Givargizov, V. V. Zhirnov, A. V. Kuznetsov, *et al.*, J. Vac. Sci. Technol. B **14** (3), 2030 (1996).
3. S. A. Pshenichnyuk, Yu. M. Yumaguzin, and R. Z. Bakhtizin, Prib. Tekh. Éksp., No. 6, 143 (1998).

Translated by L. Man

Technical Physics Letters, Vol. 26, No. 1, 2000, pp. 8–9. Translated from Pis'ma v Zhurnal Tekhnicheskoĭ Fiziki, Vol. 26, No. 1, 2000, pp. 17–20.

Asymptotic Behavior of the Resonance for Two-Dimensional Waveguides Coupled via a Hole

I. Yu. Popov and S. V. Frolov

State Institute of Fine Mechanics and Optics (Technical University), St. Petersburg, Russia

Received December 28, 1998

Abstract—The principal terms of the asymptotic expansion of a resonance (quasi-eigenfrequency) are derived for waveguides coupled via a small hole. The Dirichlet condition is assumed to be fulfilled at the boundary. The results are compared to estimates obtained earlier. The construction is performed by matching asymptotic expansions for solutions of boundary-value problems. © *2000 MAIK "Nauka/Interperiodica".*

The problem of bound states and resonances in waveguides, which are coupled via small windows, has attracted special interest in recent years mainly in connection with problems of nanoelectronics. By using the variational methods, the existence of bound states close to the lower boundary of a continuous spectrum was proved and they were estimated at a small-width coupling hole [1, 2]. The asymptotic behavior of a given eigenvalue was constructed (with respect to the hole width) [3]. However, the problem of asymptotic behavior of resonances was not solved, although certain estimates (rigorous from physics viewpoint) were obtained earlier [4]. This paper answers this problem. Construction is executed by matching asymptotic expansions for solutions of boundary-value problems [5–7].

Let us consider the problem of resonances in a system of two waveguides (see figure) with widths d_+ and d_- connected via a hole with a width $2a$; assume that $d_+ > d_-$ and the hole size is small compared to the wavelength. In order to solve the Dirichlet problem for the Helmholtz equation, we construct the asymptotic behavior of the quasi-eigenfrequency $\lambda_a = k_a^2$ with respect to the parameter a near the lower boundary $\frac{\pi^2}{d_-^2}$ of a continuous spectrum branch. Note that the continuous spectrum starts at the point $\frac{\pi^2}{d_+^2}$, $\frac{\pi^2}{d_+^2} < \frac{\pi^2}{d_-^2}$. Let us examine the asymptotic series of the following form:

$$\left(\frac{\pi^2}{d_-^2} - k_a^2\right)^{1/2} = \sum_{j=2}^{\infty} \sum_{i=0}^{[(j-1)/2]} k_{ji} a^j \left(\ln\frac{a}{a_0}\right)^i. \qquad (1)$$

Here, a_0 is the characteristic unit length (e.g., d_-).

In order to determine the coefficients k_{ij} in (1), we use the method of matching the asymptotic expansions of quasi-eigenfunctions having the form

$$\psi_a(x) = \left(\frac{\pi^2}{d_-^2} - k_a^2\right)^{1/2} \times \sum_{j=0}^{\infty} a^j P_{j+1}\left(D_y, \ln\frac{a}{a_0}\right) G^-(x, y, k)|_{y=0}, \quad x \in \Omega^- \backslash S_{a^{1/2}}, \qquad (2)$$

$$\psi_a(x) = \sum_{j=1}^{\infty} \sum_{i=0}^{[(j-1)/2]} \nu_{ji}(x/a) a^j \left(\ln\frac{a}{a_0}\right)^i, \quad x \in S_{2a^{1/2}}, \qquad (3)$$

$$\psi_a(x) = -\left(\frac{\pi^2}{d_-^2} - k_a^2\right)^{1/2} \times \sum_{j=0}^{\infty} a^j P_{j+1}\left(D_y, \ln\frac{a}{a_0}\right) G^+(x, y, k)|_{y=0}, \quad x \in \Omega^+ \backslash S_{a^{1/2}}. \qquad (4)$$

Here, S_t is the sphere of the radius t with the center coinciding with the middle of the hole, $\nu_{ji} \in W^1_{2,\,\mathrm{loc}}(\Omega^+ \cup \Omega^-)$, P_m are certain polynomial in D_y, and $G^\pm$ is the Green function for waveguides $\Omega^\pm$. Matching expansions (2) and (3), as well as (3) and (4), we derive the following values of the first four coefficients k_{ij}:

$$k_{20} = \frac{\pi^3}{2d_-^3}, \qquad (5)$$

$$k_{30} = 0, \qquad (6)$$

1063-7850/00/2601-0008$20.00

$$k_{40} = \frac{\pi^4}{4d_-^2}\left(\frac{\pi}{d_+^2\sqrt{d_-^2 - d_+^2}} - \frac{1}{2d_-}\right.$$
$$\left.\times\left(g_{1n}^+\left(0, \frac{\pi}{d_-}\right) + g_{1n}^-\left(0, \frac{\pi}{d_-}\right)\right) + \frac{\pi}{8d_-^3}\right), \quad (7)$$

$$k_{41} = -\frac{\pi^5}{2d_-^5}, \quad (8)$$

where $g_{1n}^+\left(0, \frac{\pi}{d_-}\right)$ and $g_{1n}^-\left(0, \frac{\pi}{d_-}\right)$ are the values of the normal derivatives of the functions $g_1^+(x, k)$ and $g_1^-(x, k)$, respectively, at the point $\left((0; 0), \frac{\pi}{d_-}\right)$. These functions are involved in the asymptotics of the normal derivatives of Green functions. Note that the first term in (7), which is purely imaginary, is the dominant part in the asymptotics of the imaginary resonance part. The asymptotics of the quasi-eigenfrequency has the following final form:

$$\lambda_a = \frac{\pi^2}{d_-^2} - k_{20}^2 a^4 - 2k_{20}\left(k_{40} + k_{41}\ln\frac{a}{a_0}\right)a^6$$
$$-\left(k_{40}^2 + 2k_{40}k_{41}\ln\frac{a}{a_0} + k_{41}^2\left(\ln\frac{a}{a_0}\right)^2\right)a^8 + o(a^8). \quad (9)$$

Let us consider the case of $d_- = d_+ = d$. In this situation, the scheme described above already yields not the resonance (quasi-eigenfrequency) asymptotics, but several first terms of the asymptotic expansion of the eigenfrequency, which is close to the boundary of the continuous spectrum (the first term of this asymptotics was determined in [3]). The functions G^+ and G^- now coincide, and the values of the function ψ_a differ in the domains $\Omega^-\backslash S_{a^{1/2}}$ and $\Omega^+\backslash S_{a^{1/2}}$ only by signs. Taking this into account, we derive the following values of k_{ij}:

$$k_{20} = \frac{\pi^3}{d^3}, \quad (10)$$

$$k_{30} = 0, \quad (11)$$

$$k_{40} = \frac{\pi^4}{d^3}\left(\frac{3\pi}{16d^2} - g_{1n}\left(0, \frac{\pi}{d}\right)\right), \quad (12)$$

$$k_{41} = -\frac{\pi^5}{d^5}. \quad (13)$$

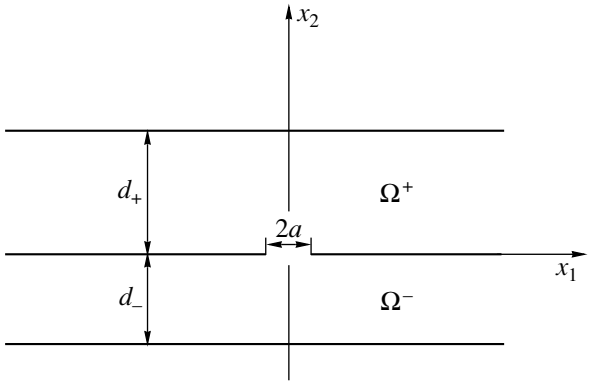

Geometric configuration of the system: $d_\pm$ is the width of the waveguide $\Omega_\pm$ and $2a$ is the width of the coupling hole. The selected coordinate system is shown.

The expression for λ_a is given by the same formula (9) with other coefficient values (10)–(13).

ACKNOWLEDGMENTS

This work was supported in part by the Russian Foundation for Basic Research and by the International Science Foundation.

I. Yu. Popov is grateful to the Center of Theoretical Physics (Loumini, Marseilles, France), where part of this work was carried out, and for hospitality and support.

REFERENCES

1. P. Exner and S. Vugalter, Ann. Inst. Henri Poincare **65** (1), 109 (1996).
2. P. Exner and S. Vugalter, J. Phys. A: Math. Gen. **30** (22), 7863 (1997).
3. I. Yu. Popov, Pis'ma Zh. Tekh. Fiz. **25** (3), 57 (1999) [Tech. Phys. Lett. **25** (2), 106 (1999)].
4. C. Kunze, Phys. Rev. B: Condens. Matter **48** (19), 14338 (1993).
5. A. M. Il'in, *Coordination of Asymptotic Expansions of Solutions of Boundary-Value Problems* [in Russian] (Nauka, Moscow, 1989).
6. R. R. Gadyl'shin, Algeb. Analysis **4** (2), 88 (1992).

Translated by A. Seferov

Technical Physics Letters, Vol. 26, No. 1, 2000, pp. 81–84. Translated from Pis'ma v Zhurnal Tekhnicheskoĭ Fiziki, Vol. 26, No. 2, 2000, pp. 77–85.

The Dynamics of Double Reversal of Wave Fronts in Photorefractive Crystals

F. N. Nikiforov, I. V. Murashko, I. A. Vodovatov, V. Yu. Petrun'kin, and E. V. Mokrushina

St. Petersburg State Technical University, St. Petersburg, 195251 Russia
Ioffe Physicotechnical Institute, Russian Academy of Sciences, St. Petersburg, 194021 Russia
Received September 20, 1999

Abstract—Averaged equations are derived describing the process of relaxation of reversed waves in the case of complex light fields in a scheme of double reversing mirror. Qualitative agreement between the experimentally derived and calculated time dependences is obtained for an optical circuit employing a $Bi_{12}TiO_{20}$ crystal.

The investigation of four-wave interaction of light in photorefractive materials is of interest in the context of developing optical devices such as neuron nets for pattern recognition, information processing, and for other purposes (see [1]). In this study, we treat theoretically the dynamics of double incoherent reversal of complex wave fronts (see [2–4]) under different initial conditions.

We proceed from the premise that, in a photorefractive crystal, the scattered field (less the reversed wave) is random. This fact may be used to derive simple equations which describe fairly accurately the phenomena of interest to us.

We will formulate the problem as follows: two waves $\mathbf{E}_1$ and $\mathbf{E}_2$ are incident on a photorefractive medium on the right and left. We will represent the field in the medium in the form of expansion (Fig. 1b)

$$\begin{aligned}\mathbf{E}_1 &= \mathbf{E}_{1p} + \mathbf{E}_{1c} + \mathbf{E}_{1f},\\ \mathbf{E}_2 &= \mathbf{E}_{2p} + \mathbf{E}_{2c} + \mathbf{E}_{2f},\end{aligned} \tag{1}$$

where $\mathbf{E}_{1p}$ is the direct wave incident on the left, $\mathbf{E}_{1c}$ is the wave reversed with respect to $\mathbf{E}_2$, and $\mathbf{E}_{1f}$ is the wave scattered from random nonuniformities of the index of refraction (fanning). The wave $\mathbf{E}_2$ propagating on the other side of the crystal is resolved into the same components. The waves $\mathbf{E}_1$ and $\mathbf{E}_2$ are incoherent, and their interaction with the medium may be treated independently.

We will assume that

$$\mathbf{E}_{1p} = A_p^{(1)}(z, t)\mathbf{e}_1(\mathbf{r})\exp(-i(\mathbf{k}_1\mathbf{r})), \tag{2}$$

where $\mathbf{e}_1(\mathbf{r})$ is the distribution of the field of unperturbed incident wave, and $A_p^{(1)}(z, t)$ is the slowly varying amplitude of the pumping wave;

$$\mathbf{E}_{1c} = A_c^{(1)}(z, t)\mathbf{e}_2^*(\mathbf{r})\exp(-i(\mathbf{k}_2\mathbf{r})), \tag{3}$$

where $\mathbf{e}_2(\mathbf{r})$ is the distribution of the field of unperturbed wave incident on the right; $A_c^{(1)}(z, t)$ is the slowly varying amplitude of the reversed wave; and

$$\mathbf{E}_{1f} = A_f^{(1)}(z, t)\mathbf{f}_f^{(1)}(\mathbf{r}, t)\exp(-i(\mathbf{k}_2\mathbf{r})), \tag{4}$$

where $\mathbf{f}_f^{(1)}(\mathbf{r}, t)$ is the distribution of random scattered field and $A_f^{(1)}(z, t)$ is the slowly varying amplitude of fanning. Analogous expressions describe the wave $\mathbf{E}_2$ incident on the right.

The normalization conditions

$$\int_S (\mathbf{e}_1\mathbf{e}_1^*)ds = 1; \quad \int_S (\mathbf{e}_2\mathbf{e}_2^*)ds = 1 \tag{5}$$

are valid, where integration is performed with respect to the arbitrary cross section of crystal z = const,

$$\left\langle \int_S (\mathbf{f}_f^{(1)}\mathbf{f}_f^{(1)*})ds \right\rangle = 1, \tag{6}$$

where $\langle\ \rangle$ indicates averaging over the ensemble of realizations.

In addition,

$$\langle \mathbf{f}_f^{(1)} \rangle = 0. \tag{7}$$

The fields are treated as a result of the effect of

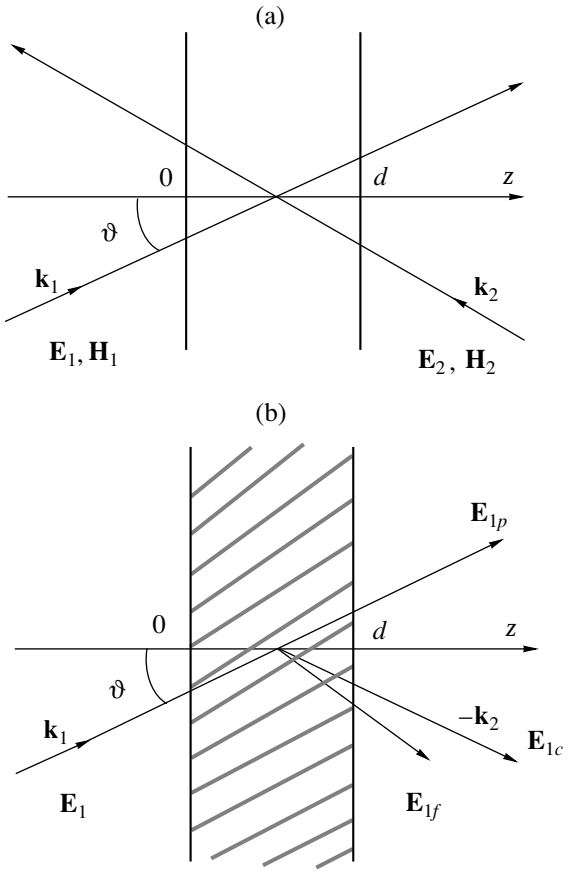

Fig. 1.

equivalent current,

$$\mathbf{j}_{\text{eq}} = \mathbf{E}_1 i\Delta\epsilon\frac{\omega}{4\pi}, \tag{8}$$

where $\Delta\epsilon = \epsilon_m(\mathbf{r}, t)\exp(i(\boldsymbol{\kappa}\mathbf{r})) + \epsilon_m^*(\mathbf{r}, t)\exp(-i(\boldsymbol{\kappa}\mathbf{r}))$, and ϵ_m is the complex amplitude of lattice in crystal. The condition

$$\mathbf{k}_1 + \mathbf{k}_2 + \boldsymbol{\kappa} = 0 \tag{9}$$

is valid.

The formulation of the problem implies the possibility of a fairly complex structure of waves described by the functions $\mathbf{e}_1$, $\mathbf{e}_2$, $\mathbf{f}_f^{(1)}$, and $\mathbf{f}_f^{(2)}$. The problem consists in deriving equations relating the amplitudes $A_p^{(1)}$, $A_p^{(2)}$, $A_c^{(1)}$, $A_c^{(2)}$, $A_f^{(1)}$, and $A_f^{(2)}$. A detailed derivation of the equations will be published separately. We will only note that the Lorentz integral lemma was used in derivation, much as this is done, for example, in treating the problem on excitation of light guide in [5] or in solving the problem on light diffraction by ultrasound [6, 7]. As a result, expressions are derived, which are simplified considerably after averaging using equations (6) and (7). Further, use is made of the constitutive relation for the photorefractive medium, known from [8], which are likewise subjected to averaging over the ensemble of realizations. For definiteness, we will assume that, in the medium being treated, the lattice of refractive index is $\pi/2$ out of phase with respect to the light interference pattern, which, in particular, corresponds to the diffusion mechanism of recording. All of these operations result in the set of equations describing the dynamics of double reversal of fronts in photorefractive crystals,

$$\left(\frac{\partial}{\partial t} + \frac{1}{\tau}\right)(N^* + N_0^*) = QB(A_p^{(1)}A_c^{(1)*} + A_p^{(2)}A_c^{(2)*}),$$

$$\left(\frac{\partial}{\partial t} + \frac{1}{\tau}\right)(N_f^{(1)} + N_{f0}^{(1)}) = QC_1A_p^{(1)}A_f^{(1)*}, \tag{10}$$

$$\left(\frac{\partial}{\partial t} + \frac{1}{\tau}\right)(N_f^{(2)} + N_{f0}^{(2)}) = QC_2A_p^{(2)}A_f^{(2)*},$$

$$\frac{\partial A_p^{(1)}}{\partial z} = -D\{A_c^{(1)}N^* + A_f^{(1)}N_f^{(1)}\},$$

$$\frac{\partial A_c^{(1)}}{\partial z} = DA_p^{(1)}N, \tag{11}$$

$$\frac{\partial A_f^{(1)}}{\partial z} = DA_p^{(1)}N_f^{(1)*},$$

$$-\frac{\partial A_p^{(2)}}{\partial z} = -D\{A_c^{(2)}N^* + A_f^{(2)}N_f^{(2)}\},$$

$$-\frac{\partial A_c^{(2)}}{\partial z} = DA_p^{(2)}N, \tag{12}$$

$$-\frac{\partial A_f^{(2)}}{\partial z} = DA_p^{(2)}N_f^{(2)},$$

where τ is the relaxation time of dielectric permeability; $Q = \Gamma/(2I_0)$ (Γ is the nonlinear coupling constant and I_0 is the total intensity of all incident beams),

$$D = \frac{\omega}{c2\cos\theta}\sqrt{\frac{\mu}{\epsilon}},$$

$$B = \int_S |\mathbf{e}_1|^2|\mathbf{e}_2|^2 ds,$$

$$C_1 = \int_S |\mathbf{e}_1|^2\langle|\mathbf{f}_f^{(1)}|^2\rangle ds,$$

$$C_2 = \int_S |\mathbf{e}_2|^2\langle|\mathbf{f}_f^{(2)}|^2\rangle ds.$$

The quantities N, N^*, $N_f^{(1)}$, and $N_f^{(2)}$ entering the equations characterize the degree of correlation between the fields and lattice,

$$N = i\int_S \epsilon_m^*(\mathbf{e}_1\mathbf{e}_2)ds,$$

$$N_f^{(1)} = -i\left\langle \int_S \epsilon_m(\mathbf{f}_f^{(1)}\mathbf{e}_1^*)ds \right\rangle, \quad (13)$$

$$N_f^{(2)} = -i\left\langle \int_S \epsilon_m(\mathbf{f}_f^{(2)}\mathbf{e}_2^*)ds \right\rangle.$$

The quantities N_0, $N_{f0}^{(1)}$, and $N_{f0}^{(2)}$ correspond to the initial values of the refractive index lattices which are due to crystal defects or impurities responsible for lattices with long relaxation times.

The derived equations are in many ways similar to those given by Zozulya [9]. The distinction is that our equations include the coefficients B, C_1, and C_2 dependents on the field structure. The coefficient B may be calculated, while $\mathbf{e}_1$ and $\mathbf{e}_2$ are preassigned. As to C_1 and C_2, they include the unknown distributions $\mathbf{f}_f^{(1)}$, and $\mathbf{f}_f^{(2)}$. One can estimate their magnitude by making assumptions about the behavior of fanning distribution. In a number of cases, they may be regarded as constant quantities.

The approach described herein to the solution of problems, which is associated with photorefraction, may be also applied in more complex cases, for example, when treating generator schemes such as that of a semilinear generator or a generator employing a resonator with two reversing mirrors (descriptions of these schemes are found, for example, in [10]), as well as other problems.

The initial and boundary conditions have the following form:

$$N(t=0) = N_f^{(1)}(t=0) = N_f^{(2)}(t=0) = 0;$$

$$A_p^{(1)}(z=0,t) = A_{p0}^{(1)}, \quad A_p^{(2)}(z=d,t) = A_{p0}^{(2)};$$

$$A_c^{(1)}(z=0,t) = A_c^{(2)}(z=d,t) = 0; \quad (14)$$

$$A_f^{(1)}(z=0,t) = A_f^{(2)}(z=d,t) = 0.$$

Equations (10) were solved numerically by the modified Euler method, and (11) and (12) were solved by Milne's method; as a result, curves were obtained indicative of the diversity of transient characteristics depending on the values of parameters. Figure 2 gives examples of transient characteristics in which only one parameter was varied, namely, the initial seed for reversed wave lattice N_0. The curves are given in conventional units selected such that the coefficients entering the equations be of the order of unity. The time in the graphs is given in τ units. In addition to the reversed wave (curves A_1 and B_1 in Fig. 2b), the graph further demonstrates the development of fanning (curves C and D, respectively).

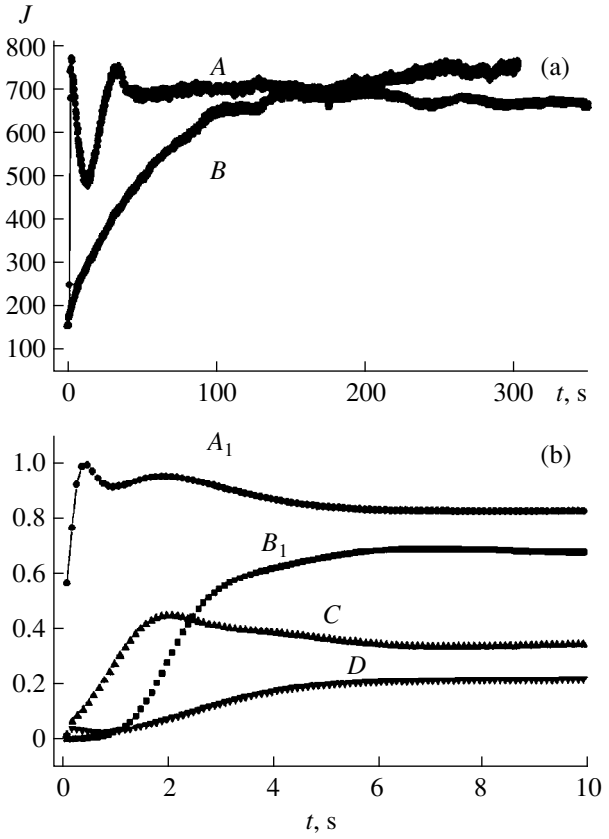

Fig. 2.

Physical experiments were performed by the standard optical scheme of a double reversing mirror, described, for example, by Fischer *et al.* [10]. Two pumping beams from two independent helium–neon lasers L1 and L2 ($\lambda = 0.63$ μm), directed in opposition to each other at an angle $\theta = 4°$, intersected in a $Bi_{12}TiO_{20}$ crystal with the dimensions of $10 \times 4 \times 9$ mm corresponding to the [112], [111], and [110] crystallographic axes with polished ⟨110⟩ faces. One of the beams had a Gaussian shape, and the other one, when necessary, was passed through a diffuser (matte plate), with the diffuse radiation focused by a lens on the crystal face. The beam power did not exceed 3 and 6 mW. A variable meander-shaped electric field with an intensity of 5 kV/cm and a frequency of about 50 Hz was applied to the sample in the [111] direction.

Figure 2 demonstrates the dynamics of relaxation of reversed wave for two different values of seed N_0. In the experiment (Fig. 2a), after preliminary steady-state reversal, both beams were interrupted, and the recorded lattices were relaxing for some time in darkness. At

$t = 0$, both beams were opened again. The relaxation times for curves *A* and *B* were 5 and 11 min, respectively. The A_1 and B_1 dependences in Fig. 2b were calculated from equations (10)–(12) for the values of $N_0 = 0.5$ and 0.01, respectively. One can see that the suggested theoretical model describes qualitatively the singularities of development of reversed wave. For the case of high seeding N_0 (curves *A* and A_1), the reversed wave growth is substantially nonmonotonic. In the case of low seeding (curves *B* and B_1), the oscillatory behavior of the transient process ceases, the time of construction of reversed wave increases, and the steady-state amplitude of reversed wave proves to be somewhat smaller. Therefore, the magnitude of initial seed for reversed wave N_0 affects both the dynamics of construction of reversed wave, as was previously mentioned by Zozulya [9], and the steady-state mode. This behavior of the above-identified curves is attributed to the competition between reversed wave and fanning. If the recorded structure relaxed for a short time (N_0 was high), fanning increases at a slower rate and is suppressed by reversed wave in the initial stage of its development (curve *C* in Fig. 2b). With a low value of N_0, the depletion of fanning occurs at a later time (its development curve has a maximum), and it is stabilized at a higher level (curve *D* in Fig. 2b). This may explain the dependence of steady states of reversed wave on the level of seeding.

As a result of this study, averaged equations have been derived describing the process of relaxation of reversed waves in the case of complex light fields in a double reversing mirror scheme. Qualitative agreement has been obtained between experimentally and theoretically derived time dependences for a certain set of parameters. It is possible to apply this approach to more complex optical schemes which provide the basis for systems of pattern recognition.

REFERENCES

1. D. Psaltis, D. Brady, and K. Wagner, Appl. Opt. **27** (9), 1752 (1988).
2. M. Horowitz, D. Kligler, and B. Fischer, J. Opt. Soc. Am. B **8** (10), 2204 (1991).
3. He Q. Byron, Pochi Yeh, Claire Gu, and R.R. Neurgaonkar, J. Opt. Soc. Am. B **9** (1), 114 (1992).
4. M. P. Petrov, Kh. D. Kolfild, and E. V. Mokrushina, Kvantovaya Élektron. **19** (3) (1992) [Quantum Electron. **19** (3) (1992)].
5. P. A. Vaĭnshteĭn, *Electromagnetic Waves* (Radio i svyaz', Moscow, 1988).
6. I. A. Vodovatov and V. Yu. Petrun'kin, Izv. Vyssh. Uchebn. Zaved. Radiofiz. **XXVI**, 1570 (1983).
7. I. A. Vodovatov, N. S. Pliss, L. N. Popova, and A. I. Puchkova, Izv. Vyssh. Uchebn. Zaved. **37**, 1939 (1994).
8. M. P. Petrov, S. I. Stepanov, and A. V. Khomenko, *Photorefractive Crystals in Coherent Optics* (Nauka, St. Petersburg, 1992).
9. A. A. Zozulya, Kvantovaya Élektron. **19** (8) (1992) [Quantum Electron. **19** (8) (1992)].
10. B. Fischer, S. Sternklar, and S. Weiss, IEEE J. Quantum Electron. **25** (3) (1989).

Translated by H. Bronsteĭn

Technical Physics Letters, Vol. 26, No. 1, 2000, pp. 85–87. Translated from Pis'ma v Zhurnal Tekhnicheskoĭ Fiziki, Vol. 26, No. 2, 2000, pp. 86–91.

Nonlinear Dynamics of a Domain Boundary in the Vicinity of the Curie Point in Ferromagnetics

G. E. Khodenkov

Institute of Electronic Controlling Machines, Moscow, Russia

Received July 29, 1999

Abstract—A rigorous nonlinear solution for a domain boundary with the varying magnitude of the magnetization vector (a Zhirnov domain boundary) has been obtained for ferromagnetics in a magnetic field in the approximation of the Landau second-order phase transitions. The results obtained indicate the efficiency of the nonlocal magnetization reversal mechanism in the range of the Curie temperature. © *2000 MAIK "Nauka/Interperiodica".*

One of the methods used for image recording, its processing, and the accumulation of information with the aid of thermomagnetic devices is based on heating of ferromagnetic material–carrier up to the Curie temperature T_C [1]. To estimate the response speed of such devices, one has to record the dependence of the magnetization reversal time, and, in particular, the velocity of the domain boundary, as a function of an applied magnetic field. Unfortunately, the dynamics of domain boundaries (domain walls) was considered mainly for ferromagnetics outside the Curie range, $T \ll T_C$ (see, e.g., review [2]). In the vicinity of T_C, the magnetization-vector magnitude changes its value, and therefore the well known dynamic results cannot be used in this temperature range.

Below, we describe the study of the nonlinear dynamics of a one-dimensional domain boundary (domain wall) in terms of the standard Landau thermodynamic potential. It turned out that, for magnetic fields below a certain critical strength, there exists an exact nonlinear solution describing the stationary dynamics of a domain boundary. The studies of its stability show that, in more intense fields, the solution becomes unstable, and the general distribution of magnetization tends to become uniform. Within the framework of the Landau potential, the periodic (strip) domain structure sometimes used for recording of information also becomes unstable.

The dynamics of magnetization $M(y, t)$ at temperatures somewhat lower than T_C obeys the Landau–Khalatnikov equation

$$\frac{\partial M}{\partial t} = -\frac{1}{\tau}\frac{\delta \Phi}{\delta M}, \tag{1}$$

in which τ is the time of longitudinal relaxation of magnetization and

$$\Phi = -\int dy\left[\frac{\alpha}{2}(\nabla M)^2 - AM^2 + BM^4 - HM\right] \tag{2}$$

is the thermodynamic potential (M is the magnetization, $\alpha > 0$ is the exchange stiffness, $A = \alpha(T_C - T) > 0$, $a > 0$, and $B > 0$ are the coefficients of the expansion of the potential below the Curie temperature, T_C, and H is the constant external magnetic field). Introducing the dimensional variables

$$t \longrightarrow \left(\frac{\tau}{2A}\right)t, \quad y \longrightarrow \sqrt{\frac{\alpha}{2A}}y,$$
$$M \longrightarrow \sqrt{\frac{A}{2B}}m, \quad H \longrightarrow 2A\sqrt{\frac{A}{2B}}H, \tag{3}$$

we reduce equation (1) to the standard form

$$\dot{m} = m'' + m - m^3 + H. \tag{4}$$

Despite the fact that equations of this type are widely used in various fields of physics (especially in the theory of self-oscillation processes [3]), as far as we know, equation (4) has never been used to describe the nonlinear dynamics of domain boundaries.

In the case $H = 0$, equation (4) has the static solution

$$m(y) = \tanh\left(\frac{y}{\sqrt{2}}\right), \tag{5}$$

which describes the transitions between the domains $m(y \longrightarrow \pm\infty) = \pm 1$ via the changes in the magnitude of the magnetization vector without any rotations (the so-called Zhirnov domain boundary described in 1958 [4]). It is well known that, even for a more general form of the right-hand side of equation (4), such equations, under certain limitations, have stable solitary (separatrix) solutions connecting two saddle point singularities (described in [3] and then in [5]). In the present study, we search for a stationary solution in the form $m(y - Vt)$ (where V is the velocity of a nonlinear wave), which extends equation (5) to the case of a nonzero magnetic field.

1063-7850/00/2601-0085$20.00

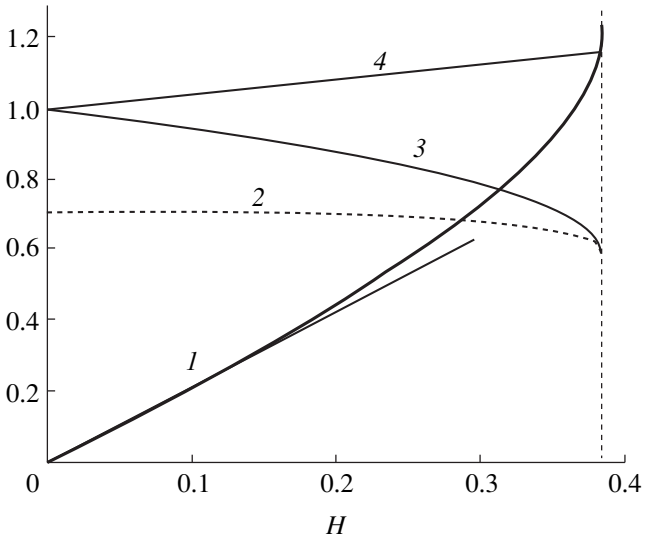

(*1*) Velocity (absolute value) of a domain boundary (8) and its linear approximation (lower line); (*2*) reciprocal grain boundary (9), (*3*) $|m(-\infty)|$ magnetization, and (*4*) $m(\infty)$ magnetization (6).

The positions of singular points of (4) and the magnetization values of the domain boundary at $y \longrightarrow \pm\infty$ are determined by the roots of a cubic equation $m - m^3 + H = 0$. If $H < H_0 \equiv \frac{2}{3\sqrt{3}}$, three real solutions exist; at $H > H_0$, only one real solution exists (for definiteness, $H > 0$). The separatrix solution connecting two saddle-point singularities exists only in the first case, where to two different saddle-point singularities there correspond the minimum and the maximum roots, respectively:

$$m(-\infty) = -\frac{1}{\sqrt{3}}\cos\varphi(H) - \sin\varphi(H)$$
$$\text{and } m(\infty) = \frac{2}{\sqrt{3}}\cos\varphi(H), \quad (6)$$

where $\varphi(H) = \frac{1}{3}\arctan\sqrt{(H_0/H)^2 - 1}$. It can readily be shown that the dynamic solution of (4) generalizing the static solution (5) with due regard for the reduced asymptotic values (6) has the form

$$m(y - Vt) = \frac{m(\infty) - m(-\infty)}{2}\tanh[b(y - Vt)] + \frac{m(\infty) + m(-\infty)}{2}. \quad (7)$$

The parameters entering (7) are the domain-boundary velocity V and the reciprocal thickness of the domain boundary, b:

$$V(H) = \sqrt{6}\sin\left(\varphi(H) - \frac{\pi}{6}\right), \quad (8)$$

$$b(H) = \frac{1}{\sqrt{2}}\cos\left(\varphi(H) - \frac{\pi}{6}\right). \quad (9)$$

Solution (7) is valid only for $H < H_0 \equiv \frac{2}{3\sqrt{3}}$ (see figure). In weak fields, we have $|V| = 3H/\sqrt{2}$; the limiting velocity is $|V(H_0)| = \sqrt{3/2}$; in the vicinity of this velocity, (8) has a characteristic root singularity, $\sim\sqrt{H_0 - H}$, which separates the stationary mode at $H < H_0$ from the nonstationary mode at $H > H_0$.

Comparing (8) with the Walker solution for a domain boundary in a ferromagnetic below the Curie region [6] (which is, in fact, the only exact solution for the nonlinear domain-boundary dynamics), we see several obvious differences. First, in (8), the function $V(H)$ is a monotonically increasing one (showing no extremum in the internal domain similar to that described in [6]). Second, the parameter of the domain-boundary width $1/b$ is also a monotonically increasing function of the field (and not a decreasing one as in [6]). Another important difference relates to the range of the nonstationary mode. In [6], in the nonstationary mode (above the so-called Walker limiting velocity), the travelling motion of the domain boundary is superimposed on the oscillatory motion. The Zhirnov dynamics of a domain boundary is of a quite different nature. Equation (4) at $H > H_0$ has only one singular point, $m_0 H = \frac{2}{\sqrt{3}}\cosh\left[\frac{1}{3}\operatorname{arctanh}\sqrt{1 - (H_0/H)^2}\right]$, which corresponds to the minimum energy of the system, so that the solutions (4) tend to the nonuniform magnetization distribution $m(y, t \longrightarrow \infty) \longrightarrow m_0(H)$. In strong magnetic fields (where $m_0(H) \approx H^{1/3}$), the concluding stage of this process occurs for a characteristic time $\Delta t \sim H^{-2/3}$.

Now, consider one more problem of the stability of static periodic solutions (4)—the theoretical model of the strip structure within functional (2). The periodic static solution (4) at $H = 0$ can be represented as

$$m_0(y) = \sqrt{1 - \kappa}\,\mathrm{sinh}\left[\left(\frac{1 + \kappa}{2}\right)^{1/2} y\right]. \quad (10)$$

Here $0 < \kappa < 1$ is an arbitrary parameter and sinh is the Jacobi elliptical sinus with the modulus $k = \sqrt{(1 - \kappa)/(1 + \kappa)}$. The spatial period of (10) equals $(2^{5/2}/\sqrt{1 + k})K(k)$, where $K(k)$ is the complete first-order elliptical integral. Now, let us analyze the spectrum of problem (4) linearized with respect to (10)

and show that it has negative eigenvalues, i.e., that solution (10) is unstable.

Substituting $m(y, t) = m_0(y) + \delta m(y)\exp(-Et)$ (where E is the eigenvalue and $\delta m(y)$ is the small amplitude) into (4) and performing the change of the variable $y \longrightarrow \sqrt{2}\, z/\sqrt{1+\kappa}$, we arrive at the Lamé equation of the form

$$\Omega \delta m = -\delta m'' + 6k^2 \mathrm{sn}^2(z)\delta m, \qquad (11)$$

in which $\Omega = 2(E+1)/(1+\kappa)$. According to the general theory [7], in addition to the continuous spectrum (11), there are two more allowed zones having finite widths. To the boundaries of these zones, there correspond the periodic solutions (the Lamé functions). It is seen that the lower zone is located in the range of the negative energies

$$\frac{1+k^2}{2} - \sqrt{1-k^2+k^4} \le E \le 0. \qquad (12)$$

To the boundaries of this zone, there correspond the following Lamé functions: $\delta m \sim cn(z)dn(z)$ (the ceiling of the zone $E = 0$) and $\delta m \sim sn^2(z) - B_0$, where $B_0 = 2/(2E_0 + 1 + k^2)$ and $E_0 < 0$ is the left-hand side of inequality (12) (the bottom of the lower zone). This signifies that the periodic solution (10) of initial equation (4) is unstable with respect to perturbations, which are the solutions of equation (11) with energies belonging to zone (12).

The major result of this study is the determination of exact nonlinear dynamic solution (7) for the Zhirnov domain boundary (5) in a magnetic field. The velocity of the local magnetization reversal via the displacement of the domain boundary is limited from above by the magnetic field $H_0 \equiv \dfrac{2}{3\sqrt{3}}$. The maximum domain-boundary velocity attainable according to (8), $\sqrt{3}\,\alpha^{1/2}a^{1/2}(T_C - T)^{1/2}/\tau$, is low, because of its proximity to the Curie point. The time of local magnetization reversal (even for the region with the dimensions of the order of a domain boundary) is rather large, $\sim\tau(T_C - T)$. In practice, one often uses more effective nonlocal magnetization reversal by the fields $H > H_0$. If the field applied is sufficiently intense, the stable state of (4) is $m_0 = H^{1/3}$. According to (4), the time of relaxation to this state from its finite neighborhood is $\sim H^{2/3}$ or, in the dimensional form, $\sim\tau H^{-2/3}B^{1/3}$. A more realistic estimate can hardly been obtained, because the rate of magnetization reversal rate depends on a number of technological factors (laser pulse parameters, conditions of heat transfer and heat removal, etc.), whose consideration is beyond the scope of the present study.

REFERENCES

1. V. V. Randoshkin and A. Ya. Chervonkis, *Applied Magnetooptics* (Énergoatomizdat, Moscow, 1990).
2. A. Malozemov and G. Slonzuski, *Magnetic Domain Walls in Bubble Materials* (Academic, New York, 1979; Mir, Moscow, 1982).
3. V. A. Vasil'ev, Yu. M. Romanovskiĭ, and V. G. Yachno, *Self-Oscillation Processes* (Nauka, Moscow, 1987).
4. L. D. Landau and E. M. Lifshitz, *Electrodynamics of Continuous Media* (Nauka, Moscow, 1982; Pergamon, New York, 1981).
5. V. V. Gudkov, Zh. Vychisl. Mat. Mat. Fiz. **37** (12), 1482 (1997).
6. N. L. Shryer and L. R. Walker, J. Appl. Phys. **45** (12), 5406 (1974).
7. E. T. Whittaker and G. N. Watson, *A Course of Modern Analysis: an Introduction to the General Theory of Analytic Functions with an Account of Principal Transcendental Functions*, 4th ed. (University Press, Cambridge, 1927; GIFML, Moscow, 1963), Part 2.

Translated by L. Man

Technical Physics Letters, Vol. 26, No. 1, 2000, pp. 88–89. Translated from Pis'ma v Zhurnal Tekhnicheskoĭ Fiziki, Vol. 26, No. 2, 2000, pp. 92–94.

Excitation of Quadrupole Spin Echoes

I. V. Zolotarev, A. S. Kim, and P. G. Neĭfel'd

Perm State University, Perm, Russia

Perm Branch of Russian Research Center Applied Chemistry, Perm, Russia

Received September 27, 1999

Abstract—Quadrupole spin echoes excited by a train of pulses with differing radio-frequency carriers, the carrier frequencies being ω_Q and $\omega_Q \pm \Delta\omega_Q$, where ω_Q is the resonance frequency of the excited transition and $\Delta\omega_Q$ is a frequency detuning less than half the linewidth of nuclear quadrupole resonance, are studied for the first time. It is shown that, in this case, the amplitudes of detected echo signals are independent of the detuning and that the positions of these signals on the time axis depends on the time intervals between the excitation pulses, on $\Delta\omega_Q/\omega_Q$, and on the sign of the detuning. *© 2000 MAIK "Nauka/Interperiodica".*

The experimental observation of quadrupole spin echoes in [1] and their theoretical analysis in [2] were made for the case where a sample containing quadrupole nuclei is irradiated with a radio-frequency (RF) excitation signal consisting of periodically recurring pulses whose carrier frequencies are equal to the resonance frequency ω_Q of the excited transition and where echo signals are detected at the same frequency.

In contrast to this, Osokin [3] studied experimentally the behavior of a nuclear spin system subjected to a periodic RF excitation with carrier frequency $\omega_Q \pm \Delta\omega_Q$, where $\Delta\omega_Q$ is a frequency detuning less than half the linewidth of nuclear quadrupole resonance (NQR). In that experiment, echo signals were detected at the excitation frequency.

Here, we consider an RF excitation of a quadrupole nuclear spin system by a pulse train having three different carrier frequencies: ω_Q and $\omega_Q \pm \Delta\omega_Q$. Echo signals are detected at resonance frequency ω_Q.

By way of example, we address the case of a three-pulse train.

Specifically, the carrier frequencies of the first, second, and third pulses are ω_Q, $\omega_Q \pm \Delta\omega_Q$, and $\omega_Q - \Delta\omega_Q$, respectively, the quantity $\Delta\omega_Q$ being fixed for a train. The time intervals between the pulses are τ_1 and τ_2, respectively.

The amplitudes of the echo signals generated in response to the above excitation are

$$\text{a) } E^{(1)}_{m,m-1} = 2(I'_x)_{m,m-1}\left\{c_1(x_i)\omega_{m,m-1}\sin\omega_{m,m-1}\times\left\{t-\left[\left(2-\frac{\Delta\omega_{m,m-1}}{\omega_{m,m-1}}\right)\tau_1-2\tau_2\frac{\Delta\omega_{m,m-1}}{\omega_{m,m-1}}\right]\right\}\right\} \quad (1)$$

$$\text{at } t_1=\left(2-\frac{\Delta\omega_{m,m-1}}{\omega_{m,m-1}}\right)\tau_1-2\tau_2\frac{\Delta\omega_{m,m-1}}{\omega_{m,m-1}},$$

$$\text{b) } E^{(2)}_{m,m-1} = 2(I'_x)_{m,m-1}\left\{c_2(x_i)\omega_{m,m-1}\sin\omega_{m,m-1}\times\left\{t-\left[\left(2-\frac{\Delta\omega_{m,m-1}}{\omega_{m,m-1}}\right)\tau_1+\left(1-\frac{\Delta\omega_{m,m-1}}{\omega_{m,m-1}}\right)\tau_2\right]\right\}\right\} \quad (2)$$

$$\text{at } t_2=\left(2-\frac{\Delta\omega_{m,m-1}}{\omega_{m,m-1}}\right)\tau_1+\left(1-\frac{\Delta\omega_{m,m-1}}{\omega_{m,m-1}}\right)\tau_2,$$

$$\text{c) } E^{(3)}_{m,m-1} = 2(I'_x)_{m,m-1}\times\left\{c_3(x_i)\omega_{m,m-1}\sin\omega_{m,m-1}\left\{t-\left[2\tau_2-\frac{\Delta\omega_{m,m-1}}{\omega_{m,m-1}}\tau_1\right]\right\}\right\} \quad (3)$$

$$\text{at } t_3=2\tau_2-\frac{\Delta\omega_{m,m-1}}{\omega_{m,m-1}}\tau_1,$$

$$\text{d) } E^{(4)}_{m,m-1} = 2(I'_x)_{m,m-1}\left\{c_4(x_i)\omega_{m,m-1}\sin\omega_{m,m-1}\times\left\{t-\left[\left(1-\frac{\Delta\omega_{m,m-1}}{\omega_{m,m-1}}\right)\tau_1+2\tau_2\right]\right\}\right\} \quad (4)$$

$$\text{at } t_4=\left(1-\frac{\Delta\omega_{m,m-1}}{\omega_{m,m-1}}\right)\tau_1+2\tau_2,$$

$$\text{e) } E^{(5)}_{m,m-1} = 2(I'_x)_{m,m-1}\left\{c_5(x_i)\omega_{m,m-1}\sin\omega_{m,m-1}\times\left\{t-\left[\left(2-\frac{\Delta\omega_{m,m-1}}{\omega_{m,m-1}}\right)\tau_1+2\tau_2\right]\right\}\right\} \quad (5)$$

1063-7850/00/2601-0088$20.00 © 2000 MAIK "Nauka/Interperiodica"

at $t_5 = \left(2 - \frac{\Delta\omega_{m,m-1}}{\omega_{m,m-1}}\right)\tau_1 + 2\tau_2$.

In the above expressions, $(I'_x)_{m,m-1}$ is a matrix element of the operator I_x in the representation of the quadrupole Hamiltonian $\mathbf{H}_Q$; $c_i(x_i)$ are trigonometric functions of angular pulse durations; $\omega_{m,m-1}$ is the resonance frequency ω_Q of the excited transition; $\Delta\omega_{m,m-1}$ is the frequency detuning from ω_Q within half the NQR linewidth; τ_1 and τ_2 are the time intervals between the first and the second pulse and between the second and the third pulse, respectively; and m is the magnetic quantum number.

It was found that, for the excitation mode being considered, the echo amplitudes are virtually independent of the detuning and that the echo positions on the time axis depend not only on τ_1 and τ_2, as in the traditional case studied in [1, 2], but also on $\frac{\Delta\omega_{m,m-1}}{\omega_{m,m-1}}$ (inverse of the spectral-line Q factor) and on the sign of the detuning.

For $\Delta\omega_{m,m-1} \longrightarrow 0$, expressions (1)–(5) for the amplitudes and those for the corresponding instants of time reduce to their counterparts from [2].

By using a multifrequency pulsed NQR spectrometer, we conducted a relevant experiment with ^{63}Cu nuclei in $Y_1Ba_2Cu_3O_{7-d}$ ($d > 0$) at a resonance frequency of 31.12 MHz ($T = 297$ K). The NQR linewidth in question is about 200 kHz, so that the detuning must be less than 100 kHz. At large values of τ_1 and τ_2, the positions of the echo signals were found to deviate from those of Hahn signals.

We hope that the above excitation mode will furnish additional information about the structure of chemical compounds that are difficult to analyze by techniques known previously.

REFERENCES

1. E. L. Hahn, Phys. Rev. **80**, 580 (1950).
2. T. P. Das and A. K. Saha, Phys. Rev. **93** (4), 749 (1954).
3. D. Ya. Osokin, Zh. Éksp. Teor. Fiz. **84** (1), 118 (1983) [Sov. Phys. JETP, **57**, 69 (1983)].

Translated by A. Sharshakov